JSCSEN 74(2)223–357(2009)

Journal of the Serbian Chemical Society

VOLUME 74

No 3

BELGRADE 2009

Available on line at

www.shd.org.rs/JSCS

Journal of the Serbian Chemical Society
JSCS@tmf.bg.ac.rs • www.shd.org.rs/JSCS

J. Serb. Chem. Soc. Vol. 74, No. 3 (2009)

CONTENTS

Published by the Serbian Chemical Society
Karnegijeva 4/III, 11000 Belgrade, Serbia
Printed by the Faculty of Technology and Metallurgy
Karnegijeva 4, P.O. Box 35-03, 11120 Belgrade, Serbia

Journal of the Serbian Chemical Society
JSCS@tmf.bg.ac.rs • www.shd.org.rs/JSCS

J. Serb. Chem. Soc. 74 (3) 223–235 (2009)
JSCS–3825

UDC 547.828+544.431.143+543.51
Original scientific paper

ESI-MS spectra of 3-cyano-4-(substituted phenyl)-6-phenyl-2(1*H*)-pyridinones

ALEKSANDAR D. MARINKOVIĆ*#, TATJANA M. VASILJEVIĆ#, MILA D. LAUŠEVIĆ# and BRATISLAV Ž. JOVANOVIĆ#

Faculty of Technology and Metallurgy, University of Belgrade, Karnegijeva 4, P.O. Box 3503, 11120 Belgrade, Serbia

(Received 6 June, revised 24 October 2008)

Abstract: Twelve 3-cyano-4-(substituted phenyl)-6-phenyl-2(1*H*)-pyridinones were investigated by tandem mass spectrometry using positive as well as negative electrospray ionization. The influence of the electron affinity of the substituent and the steric effect on the fragmentation is discussed. Pyridinones with a substituent of low proton affinity show loss of water, HCN or benzene from the pyridinone ring in the first step of MS^2 fragmentations. Oppositely, if a substituent with high proton affinity is present on the phenyl ring in the 4-position of pyridinone, the fragmentation paths are complex, depending mainly on the substituent proton acceptor ability. Elimination of neutral molecules CO, HCN, H_2O, PhH (benzene) or Ph and CN radicals are fragmentation processes common for all compounds in the subsequent steps of the fragmentations.

Keywords: electrospray ionization; substituted pyridinones; tandem mass spectrometry.

INTRODUCTION

The interest in various 3-cyano-4-(substituted phenyl)-6-phenyl-2(1*H*)-pyridinone derivatives stems largely from their unique properties, which enable their use not only in the production of dyes, pigments, fuel and oil additives, but also for the development of medicinal products having a broad spectrum of biological activities.

An excellent review on the synthesis, reactivity and biological activity of 3--cyanopyridine-2(1*H*)-chalcogenones has been published.[1] Substances that improve the blood circulation and cardiotonic activity were also mentioned. Among the other types of biological activities of this class of compounds, it is worth mentioning analgetic and antihypertensive, anti-anaphylactic, diuretic and sodio-

* Corresponding author. E-mail: marinko@tmf.bg.ac.rs
# Serbian Chemical Society member.
doi: 10.2298/JSC0903223M

diuretic, anti-oxidant, antiviral, and antimicrobial compounds.[1,2] Biologically degradable agrochemical products, plant growth regulators, pesticides and herbicides are also produced from derivatives of pyridinones.[3–5] Various tautomeric forms of these molecules determine their chemical behaviour and some additional information in the study of their properties can be seen from their MS^2 spectra.

One of the classic studies of lactim/lactam tautomerism is the determination of the 2-hydroxypyridine (2HP)/2-pyridinone (2PYR) equilibrium. UV/Vis,[6,7] mass spectrometric,[8] photoelectron,[9] low-temperature matrix isolation and IR spectroscopic[10] measurements revealed that 2-hydroxypyridine exists in the gas phase and in inert matrices under equilibrium conditions mainly in the lactim form. Considering the equilibrium in solvents of different polarity, it was found that increasing the solvent polarity shifted the equilibrium towards the pyridinone (lactam) form. Furthermore, the hydrogen bonding ability of the solvent plays an important role, since hydrogen-bond donors tend to stabilize the oxo form (lactam), whereas hydrogen-bond acceptors stabilize the hydroxy form (lactim).

In order to determine the structure–fragmentation relation, the fragmentations of selected pyridinones in an ion source as well as in an ion trap were analyzed. The investigated pyridinones had the following structural formulae:

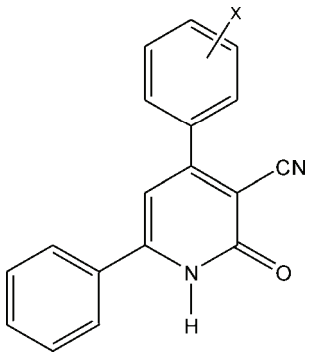

where X is: H (**1**); 4-CH_3 (**2**); 3-CH_3 (**3**); 3-Cl (4); 4-Cl (**5**); 2,4-di-Cl (**6**); 4-CN (**7**); 3-OPh (**8**); 4-OCH_3 (**9**); 3,4-di-OCH_3 (**10**); 3-NO_2 (**11**) and 4-$N(CH_3)_2$ (**12**).

The effect of the phenyl substituent in the 4-position of the pyridinone ring, steric and tautomerism effects on the fragmentation patterns are discussed.

EXPERIMENTAL

Twelve 3-cyano-4-(substituted phenyl)-6-phenyl-2(1*H*)-pyridinones were synthesized following a procedure described in the literature.[11,12] An exception was 3-cyano-4-(4-cyanophenyl)-6-phenyl-2(1*H*)-pyridinone which was synthesized by microwave irradiation of a mixture of 4-cyanobenzalacetophenone, ammonium acetate and ethyl cyanoacetate at 600 W for 6 min.

The new compounds which, to the best of our knowledge, have not been described in the literature, are as follows: 3-cyano-4-(3-phenoxyphenyl)-6-phenyl-2(1*H*)-pyridinone, m. p. 244––246 °C and 3-cyano-4-(4-cyanophenyl)-6-phenyl-2(1*H*)-pyridinone, m.p. 323–325 °C. In addition, the compounds 3-cyano-4-(3-nitrophenyl)-6-phenyl-2(1*H*)-pyridinone, m.p. > 330 °C

and 3-cyano-4-[4-(dimethylamino)phenyl]-6-phenyl-2(1*H*)-pyridinone (m.p. 313–315 °C), although comercially available, have not been considered in the literature. All new-synthesized compounds had satisfactory elemental (C, H, N) composition. Their structures were confirmed by melting point, infrared spectroscopy, ^{1}H- and ^{13}C-NMR and mass spectrometry data.

Mass spectra were obtained using a LCQ Advantage (Thermo, San Jose, CA, USA) quadrupole ion trap mass spectrometer. The electrospray ionisation technique was used in the positive and negative ion mode. The solutions of the pyridinone samples (0.10 mg/ml in CH_3OH) were injected directly into the ESI source by a syringe pump, at a flow rate of 5.0 µl min^{-1} and analysed under the following conditions: capillary temperature 250 °C; sheath gas flow 38 au (N_2); source voltage 4.5 kV; capillary voltage 35 V and –26 V in the positive and negative ionisation mode, respectively. In order to obtain MS^2 spectra, the ions of interest were isolated and fragmented in the collision with helium, with a collision energy in the range 30–50 %. The data obtained were processed using Xcalibur^{TM} 1.2 software.

RESULTS AND DISCUSSION

Mass spectra

The typical peaks that appear in the ESI$^+$-MS spectra of all the investigated pyridinones are protonated molecular ion $[M+H]^+$, the corresponding adduct ion with sodium $[M+Na]^+$ and cluster ions: $[2M+Na]^+$, $[2M–H+2Na]^+$, $[2M–2H+ +3Na]^+$. Two peak groups were also observed, which correspond to multi-charged cluster ions.

The negative ion mass spectra of the investigated pyridinones exhibit far fewer ions than the positive MS. In addition to the deprotonated (quasi-molecular) ion $[M–H]^–$, the only prominent ions present in the negative ion MS are $[2M–2H+ +Na]^–$ and $[3M–3H+2Na]^–$. Compared to the positive ion MS, the total ion current was at least ten fold lower in the negative ion MS, which could easily be explained by the high proton affinity of the studied compounds.

Fragmentation reactions of $[M+H]^+$ ions: MS^2 and pseudo-MS^3 spectra

In order to understand the influence of the different substituents on the phenyl ring of the pyridinone on the stability of the ions in the gas phase, collision-induced dissociation (CID) of the protonated molecular ion was studied. A prominent protonated molecular ion, present in the spectra of all pyridinones, was isolated in the ion trap and subjected to collision with He in order to obtain the MS^2 spectrum. Subsequently, in-source collision-induced dissociation (ISD) of the protonated molecular ion was studied and it was compared to the CID in the ion trap. As the ISD and CID spectra of the quasimolecular ions showed only negligible differences in the intensity of the peaks, it was possible to perform a pseudo-MS^3 CID of the daughter ions generated in the ion source. Mass spectral data for investigated pyridinones in the positive ion mode are presented in Table I. The CID spectrum of the protonated molecular ion of 4-(3-chlorophenyl)-3-cyano-6-phenyl-2(1*H*)-pyridinone is presented in Fig. 1a, as an example of a MS^2 spectrum.

TABLE I. Mass spectral data of the 3-cyano-4-(substituted phenyl)-6-phenyl-2(1*H*)-pyridinones in the positive mode

Compound		$[M+H]^+$ (precursor ions for MS^2)	MS^2 spectrum (precursor ions for MS^3)	Fragment ions and relative abundances (in parentheses) in pseudo MS^3
	X			
1	H	273	255^{a1}[a](100)	228^{a2}(30); 201^{a3}(3)
			195^{c1}(20)	167^{c2}(53); 140^{c3}(10)
2	4-CH_3	287	269^{a1}(100)	242^{a2}(26); 215^{a3}(5)
			260^{b1}(13)	242^{a2}(30); 234^{b4}(3); 215^{a3}(3) 227^{a5}(61);
			242^{a2}(14)	215^{a3}(67)
			209^{c1}(23)	181^{c2}(14); 154^{c3}(15)
3	3-CH_3	287	269^{a1}(77)	254^{a4}(12); 242^{a2}(100); 215^{a3}(12); 191^{a6}(8)
			260^{b1}(26)	242^{a2}(20); 232^{b2}(3)
			244^{d2}(7)	–
			242^{a2}(12)	227^{a5}(25); 215^{a3}(54)
			209^{c1}(5)	181^{c2}(100); 154^{c3}(37)
4	3-Cl	307	289^{a1}(100)	262^{a2}(19); 254^{a4}(31); 227^{a5}(9)
			272^{d1}(29)	255^{d4}(15); 244^{d2}(100)
			254^{a4}(7)	227^{a5}(19)
			229^{c1}(14)	201^{c2}(30); 174^{c3}(18)
5	4-Cl	307	289^{a1}(100)	262^{a2}(16); 254^{a4}(40); 227^{a5}(15)
			272^{d1}(26)	255^{d4}(15); 244^{d2}(100)
			254^{a4}(4)	227^{a5}(88)
			229^{c1}(25)	202^{c5}(6); 201^{c2}(38); 174^{c3}(65)
6	2,4-di-Cl	341	323^{a1}(100)	288^{a4}(100); 261^{a5}(15)
			306^{d1}(59)	289^{d4}(6); 278^{d2}(29); 271^{d6}(9)
			288^{a4}(19)	261^{a5}(12); 253^{a7}(100)
			263^{c1}(60)	236^{c5}(6); 228^{c4}(63); 208^{c3}(16)
7	4-CN	298	280^{a1}(100)	253^{a2}(12)
			253^{a2}(4)	226^{a3}(10)
			220^{c1}(12)	–
8	3-OPh	365	348(100)	320(18)
			337 (18)	–
			320(10)	292(23)
			287 (13)	–
			272^{d1}(25)	255^{d4}(10); 244^{d2}(36)
			262^{c6}(18)	–
			254^{a4}(13)	–
9	4-OCH_3	303	288(100)	260(100); 216(3)
			260(10)	242(3); 232(17); 182(5)
10	3,4-di-OCH_3	333	318(100)	289(13); 271(3); 261(15); 241(2); 211(9)
			289(28)	271(3); 261(15); 211(7)
			272(13)	244(28); 141(4)
11	3-NO_2	318	288(6)	260(100); 232(3)
			272^{d1}(100)	254^{d4b}(11); 244^{d2}(100); 217^{d3}(6); 169^{d5}(4)
			260(9)	242(14); 232(38); 217(9); 156(6)
12	4-$N(CH_3)_2$	316	300(100)	282(36); 273(51); 256(11); 222(46)
			273(5)	258(18); 256(11); 246(9); 195(9)

[a]Superscript of the *m*/*z* values defines the corresponding structure in Schemes 1–3; [b]Compound 11 follows the path d1 – d4 but water loss, instead of hydroxyl radical, was observed

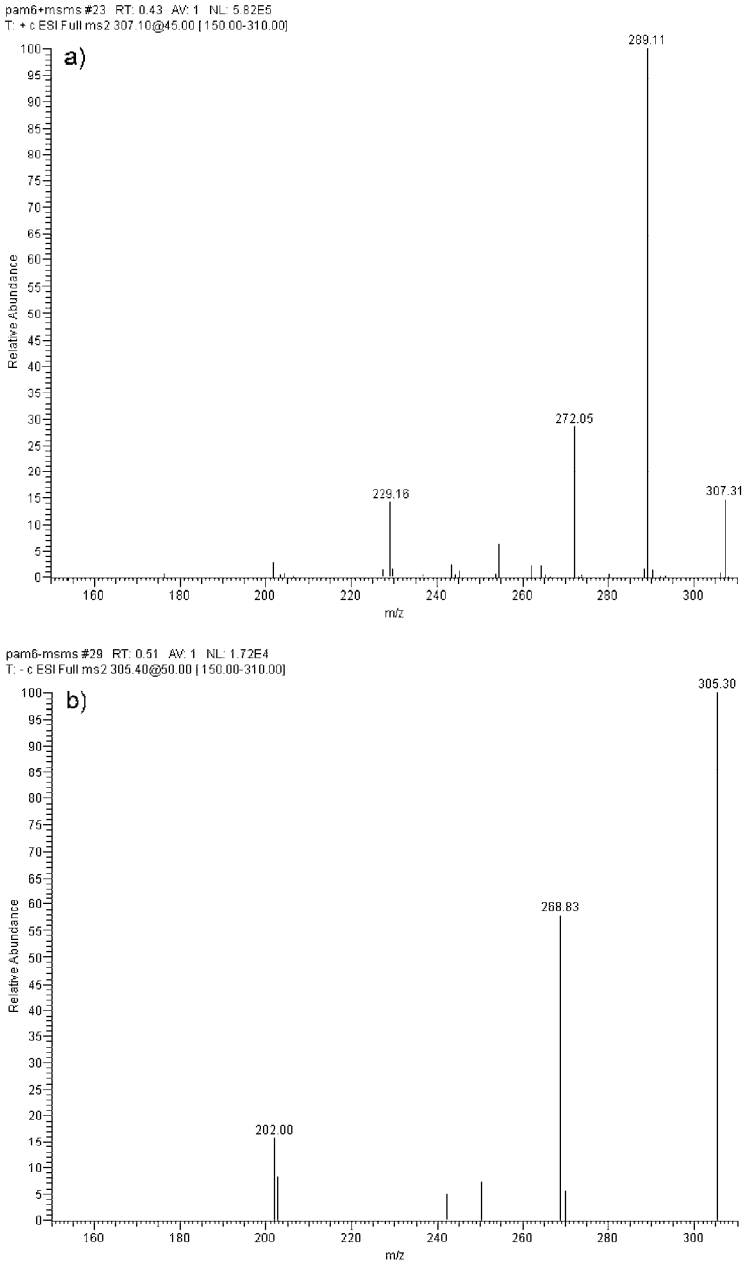

Fig. 1. MS^2 spectra of a) $[M+H]^+$ and b) $[M–H]^–$ obtained from 4-(3-chlorophenyl)- 3-cyano-6-phenyl-2(1*H*)-pyridinone.

The fragmentation pathways of the corresponding protonated molecular ions of the compounds investigated in MS^2 and quasi-MS^3 are presented in Schemes

1–3 and the mass spectral data in Table I. The LCQ Advantage spectrometer does not allow exact mass measurement, therefore the exact composition of the detected ions and lost neutral fragments could not be determined. The proposed structures are based on literature data and chemical logic.

Based on CID and ISD/CID mass spectral data from Table I, two main fragentation paths of the investigated pyridinones could be defined.

The first fragmentation pattern includes loss of a water molecule, HCN or benzene (PhH) as the first step of the MS^2 fragmentation. These loses were observed for compounds **1**–**7** and are presented in Schemes 1 and 2. The pyridinone ring of these compounds is destabilized by protonation on either the nitrogen or oxygen, thus the fragmentation occurs primarily at the pyridinone structure.

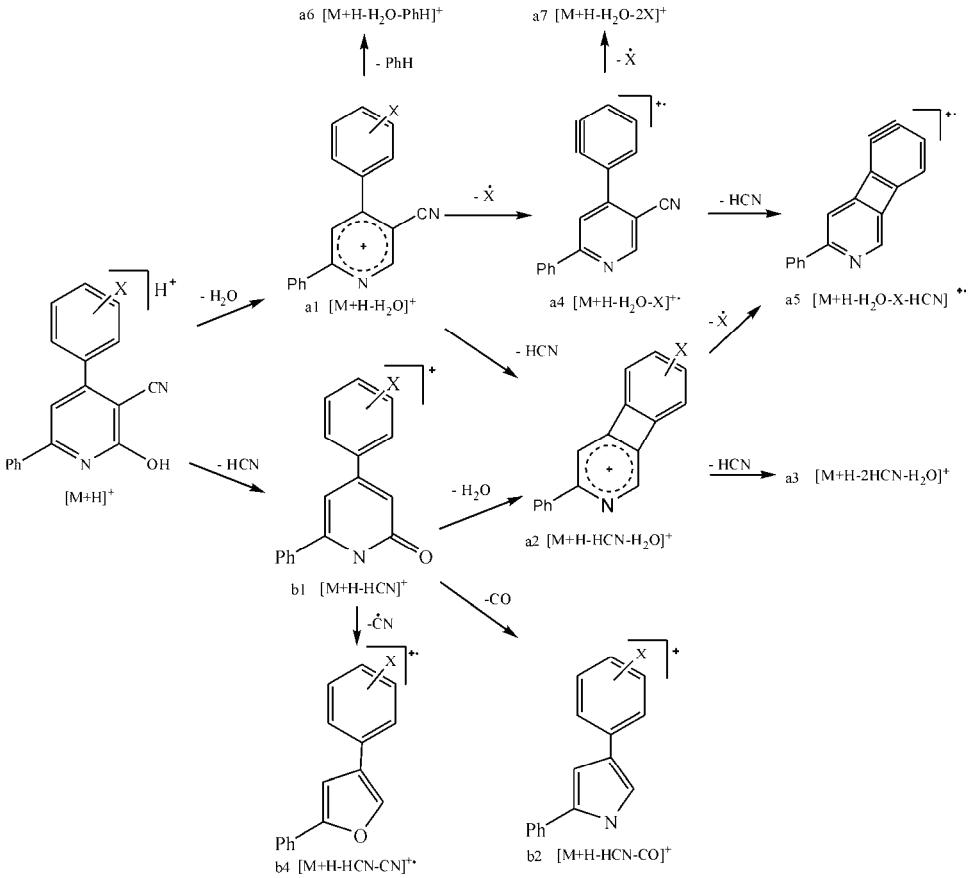

Scheme 1. Proposed fragmentation pathways of $[M+H]^+$ for the loss of H_2O or HCN in the first step.

A completely different fragmentation pattern was observed for compounds **8**–**12** (Table I). The electron-donor substituents are readily protonated, inducing

destabilization of the phenyl ring in the 4-position of pyridinone (compounds **8**–**10** and **12**). In this way, the fragmentation processes occur primarily through the substituted phenyl ring. Loss of a hydroxyl radical (*m*/*z* 348), not water, from $[M+H]^+$ of compound **8** in the MS^2 corroborates the postulate that protonation of the substituent is the main process. It could probably be because of the large phenoxy substituent, which induces a characteristic spatial arrangement of this molecule and electronic character of the C(2)–OH bond, which is more susceptible to homolytic cleavage.

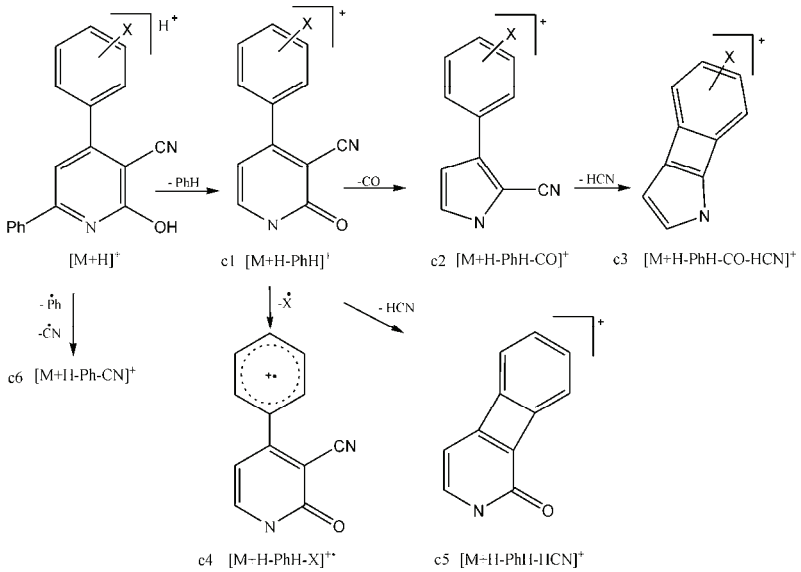

Scheme 2. Proposed fragmentation pathways of $[M+H]^+$ for the loss of a PhH molecule in the first step.

The solvent (methanol) is a hydrogen bond acceptor and donor and significantly influences the appropriate equilibrium of the tautomeric forms of the investigated pyridinones (67 mmol/mol for 2HYP/2PYR).[13] The hydroxy tautomeric form of pyridinone is readily protonated under ESI^+ conditions, water elimination occurs easily, being the main fragmentation path under MS^2 conditions for compounds **1**–**7** (Scheme 2). After water loss, further fragmentations depend on the electronic character of the substituents. For compounds with electron-donor substituents, the fragmentations follow a1-a2-a3 path, while for compounds with electron-acceptor substituents abundant ions a4 and a5 are given (Scheme 1).

The loss of HCN (fragmentation "route b", Scheme 1) followed by either the loss of CO or a CN radical was observed only for compounds **2** and **3**, in which a non-polar and weak electron donor methyl group is the substituent on the phenyl ring. In this case, the pyridinone ring is destabilized and by either loss of CO or a CN radical decomposes, probably to form a five-membered, heterosubstituted

ring (ions b2 and b4, Scheme 1). The disubstituted compound **6** follows the path a1(*m*/*z* 323)-a4 (*m*/*z* 288) by loosing only one chlorine radical in this fragmentation step.

The loss of a PhH molecule is a common fragmentation observed for compounds **1**–**7**, and the fragmentation mainly follows the path through the c1-c2-c3 sequence (Scheme 2). The intensities of the corresponding ions depend on their electronic properties. Pyridinones having a weak electron-donor or one chlorine substituent (compounds **1**–**5**) further fragment by the loss of CO and HCN from the pyridinone ring to the c3 ion. An exception is compound **6**, in which the two chlorine atoms contribute to strong electron acceptor properties. Compound **6** follows either the path to the c3 ion without a trace of the c2 ion or by elimination of Cl or HCN from the c1 ion yielding the c4 and c5 ions. The significant abundance of the c4 ion in the pseudo MS^3 of compound **6** indicates the stabilisation of this ion by the positive resonance effect of the remaining chlorine atom. The structures of the c4 and c5 ions of the disubstituted chlorine compound **6** contain one and two chlorine atoms, respectively. Compound **7**, in which the substituent is the cyano group with strong electron-acceptor properties, fragments to the c1 ion, showing quasimolecular ion stability.

The complete loss of substituent from $[M+H]^+$ follows the fragmentation paths presented in Scheme 3. This type of fragmentation is influenced by a significant destabilisation of the protonated quasimolecular ions by the electron acceptor-character of the substituent. Compounds **4** and **5** (3-Cl and 4-Cl substituents, respectively) gave a base peak d2 in the pseudo MS^3 spectra, showing a significant pyrrole type fragment stability. Considering the position of the chlorine atom in compounds **4** and **5**, small influences on the fragmentation paths could be observed. On the contrary, the fragmentation of the $[M+H]^+$ ions from compound **6** is somewhat different, indicating that the *ortho* position of the chlorine atom causes rotation of the 4-substituted phenyl ring for certain dihedral angle from a plane of the pyridinone ring. From this point of view, it is clear that the geometry of the investigated compounds also influences the fragmentation paths to some extent. For compound **6**, after the loss of one chlorine from $[M+H]^+$, the second one remains attached in structures d1, d2 and d4.

If substituents with a significant proton acceptor affinity are present in the investigated compounds, the complex fragmentation paths depend mainly on the proton acceptor ability. Compound **9**, (with one methoxy group) and compound **10** (with two methoxy groups) show some similarities but also some differences in the fragmentation paths of their $[M+H]^+$. The methoxy group was fragmented by the loss of a methyl radical, leaving a hydroxy group as a possible site for the expulsion of carbon monoxide (*m*/*z* 232) or loss of a water molecule (*m*/*z* 242). On the contrary, in the case of compound **10**, the loss of a methyl radical is followed by the loss of a formyl radical from the second methoxy group, gene-

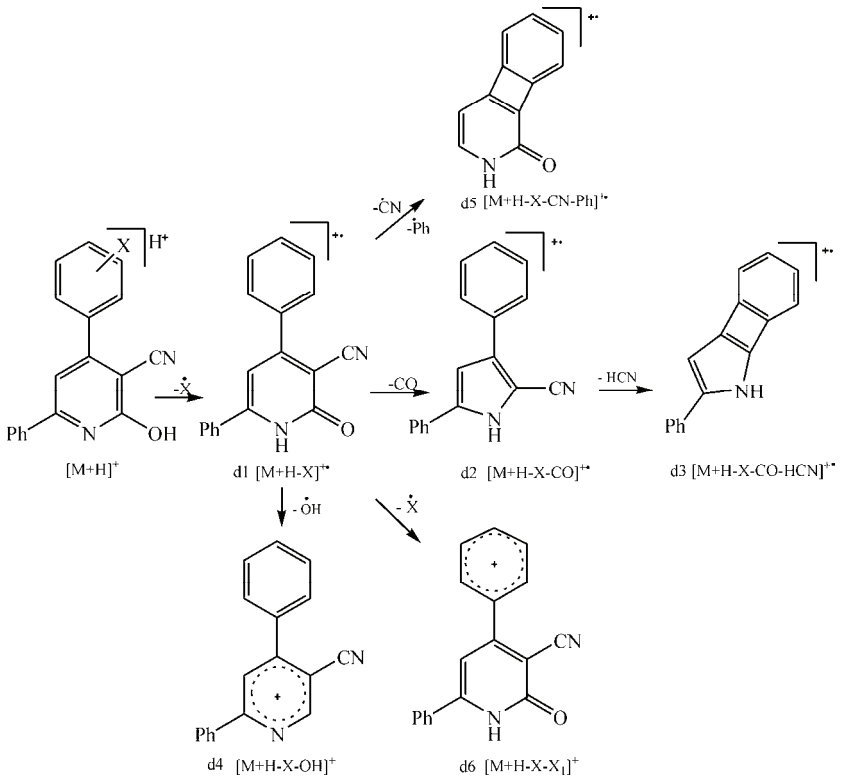

Scheme 3. Proposed fragmentation pathways of $[M+H]^+$ for the loss of the substituent in the first step.

rating the *m*/*z* 289 ion. Subsequent fragmentations involving the loss of CO, PhH and H_2O molecules are the usual fragmentations observed for all compounds. Fragmentation of compound **12** is strongly affected by the high proton acceptor affinity of the dimethylamino group. The protonated amino group easily releases methane, providing a base peak *m*/*z* 300 in the MS^2 spectrum of this compound, which after a loss of HCN produces the *m*/*z* 273 ion. The so-created methylimino group is significantly stable and further fragmentation occurs by elimination of either a PhH molecule or loss of an OH radical, producing *m*/*z* 195 and 256 ions, respectively. The nitro group present in compound **11** does not posses proton acceptor affinity but, after the well-known loss of a NO radical, the formed hydroxyl group is a good proton-acceptor (*m*/*z* 288).

The loss of a CO molecule, a typical fragmentation for 2-pyridinones molecular ion under EI condition,[14,15] is only observed for compound **8** with a low abundance of the *m*/*z* 337 ions in the MS^2 spectrum. However, by expulsions of CO from b1, c1, d1, *m*/*z* 288, 260 and 289 ions were also observed in the quasi-MS^3 spectra. This indicates appropriate influences of the tautomeric forms from

the equilibrium in the sample solution to the fragmentation paths of the investigated compounds under ESI^+ condition.

Fragmentation reactions of [M–H]$^-$

Contrary to the positive ESI-MS, where elimination of H_2O molecules was favoured, the main fragmentation process in the negative ESI–MS was the elimination of CO molecules, observed for almost all the investigated compounds. An example of the MS/MS spectrum of the $[M–H]^-$ of 4-(3-chlorophenyl)-3-cyano--6-phenyl-2(1*H*)-pyridinone is presented in Fig. 1b. The mass spectral data obtained in the negative ionization mode for $[M–H]^-$ of all investigated compounds are presented in Table II.

TABLE II. Mass spectral data of the 3-cyano-4-(substituted phenyl)-6-phenyl-2(1*H*)-pyridinones in the negative ionization mode (superscripts of the *m/z* values define the corresponding structures in Scheme 4)

Compound	X	$[M–H]^-$ (Precursor ions for MS^2)	MS^2 Spectrum
1	H	271(100)	$243e^1$(100)
2	4-CH_3	285(100)	$257e^1$(100)
3	3-CH_3	285(100)	257^{e1}(12)
4	3-Cl	305(100)	269^{e10}(58); 250^{e2}(7); 242^{e6}(5); 202^{e3}(16)
5	4-Cl	305(100)	269^{e10}(7); 250^{e2}(16)
6	2,4-di-Cl	339(100)	303^{e10}(42); 236^{e3}(12)
7	4-CN	296(100)	268^{e1}(17); 241^{e2}(30); 193^{e3}(30)
8	3-OPh	363(100)	286^{e8}(100); 270^{e4}(6); 258^{e9}(12)
9	4-OCH_3	301(100)	286^{e4}(26)
10	3,4-di-OCH_3	331(100)	316^{e4}(100); 315^{e5}(63); 287^{e7}(15)
11	3-NO_2	316(100)	286^{e4}(100); 270^{e4}(78); 258^{e6}(4)
12	4-$N(CH_3)_2$	314(100)	299^{e4}(35); 298^{e5}(8)

The fragmentations of compounds **9**, **10** and **12**, with strong electron-donor substituents, show the loss of a methyl radical. These fragmentations are similar to the corresponding ones in the ESI^+ mode. Phenyl radical loss is the base peak in the spectrum of compound **8**. The substituent in compound **11**, being a strong electron-acceptor, shows the ability to lose a nitrosyl radical in the negative ionization mode. The main fragmentation process for the chloro-substituted compounds is the loss of HCl, probably due to the accommodation of a negative charge on chlorine atom, which extracts the neighbouring proton. Typical fragmentations of the investigated pyridinones in the ESI^- ionisation mode are presented in Scheme 4.

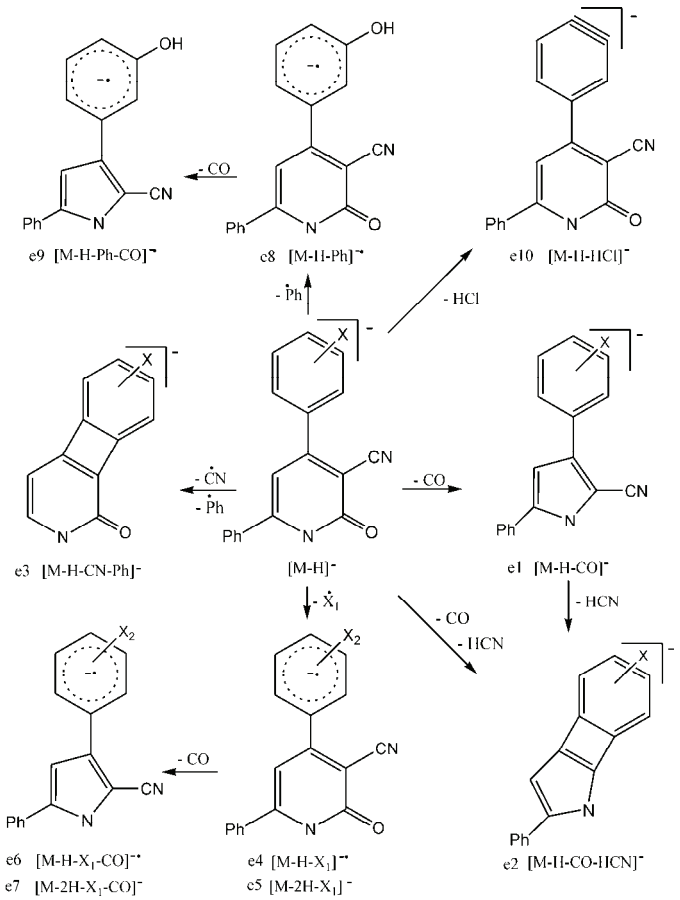

Scheme 4. Proposed fragmentation paths of the $[M–H]^–$ in the MS^2 spectra; e4 and e6 ions: $X_1 = CH_3$ for compounds **9** (*m*/*z* 286; X_2 = OH) and **10** (*m*/*z* 316; X_2 = 3-OH and 4-OCH_3), $X_1 = CH_3$ for compound **12** (*m*/*z* 299; $X_2 = NHCH_3$), X_1 = NO (*m*/*z* 286; X_2 = OH) or NO_2 (*m*/*z* 270; X_2 = H) for compound **11**, X_1 = OPh for compound **8** (*m*/*z* 270; X_2 = H); e5 and e7 ions: $X_1 = CH_4$ for compound **10** (*m*/*z* 315; X_2 = 3-OH and 4-OCH_3), $X_1 = CH_4$ for compound **12** (*m*/*z* 298; $X_2 = NHCH_2$); e10 ion containing one chlorine for the dichloro-substituted compound.

CONCLUSIONS

The typical peaks appearing in the ESI^+ spectra of all pyridinones are the protonated molecular ion $[M+H]^+$, the corresponding molecular ion adducts with sodium $[M+Na]^+$ and cluster ions $[2M+Na]^+$, $[2M–H+2Na]^+$ and $[2M–2H+3Na]^+$. The negative ESI-MS spectra exhibit far fewer ions, which are, apart from $[M–H]^–$, $[2M–2H+Na]^–$ and $[3M–3H+2Na]^–$.

Different factors influence the fragmentation pattern of the investigated pyridinones in the positive ionization mode. The position and proton affinity of the substituents play an important role in the fragmentation processes in the MS^2 and

MS^3 spectra. Pyridinones with a substituent of low proton affinity show loss of water, HCN or benzene from the pyridinone ring in the first step of MS^2 fragmentations. Conversely, if a substituent with a high proton affinity is present at the phenyl ring in the 4-position of pyridinone, the complex fragmentation paths depend mainly on the substituent proton acceptor ability. Elimination of neutral molecules CO, HCN, H_2O and PhH (benzene) or Ph and CN radicals are fragmentation processes common for all compounds in the subsequent steps of the fragmentations.

The ionisation mode significantly influences the fragmentations depending on the tautomeric form of the investigated compounds. In ESI^+, water molecule elimination indicates that protonation of the hydroxyl group of the lactam tautomer occurs. On the contrary, in ESI^-, expulsion of a CO molecule indicates deprotonation of the hydroxyl group.

Acknowledgements. The authors are grateful to the Ministry of Science and Technological Development of the Republic of Serbia for financial support (Project 142063).

ИЗВОД

ESI–MS СПЕКТРИ 3-ЦИЈАНО-4-(СУПСТИТУИСАНИ ФЕНИЛ)-6-ФЕНИЛ-2(1*H*)-ПИРИДИНОНА

АЛЕКСАНДАР Д. МАРИНКОВИЋ, ТАТЈАНА М. ВАСИЉЕВИЋ, МИЛА Д. ЛАУШЕВИЋ и БРАТИСЛАВ Ж. ЈОВАНОВИЋ

Технолошко–металуршки факултет, Универзитет у Београду, п.пр. 3503, Карнегијева 4, 11120 Београд

3-Цијано-4-(супституисани фенил)-6-фенил-2(1*H*)-пиридинони су испитивани тандем масеном спектрометријом коришћењем позитивне и негативне електроспреј јонизације. Испитиван је утицај супституената и стерног ефекта на фрагментације. Пиридинони који имају супституенте малог афинитета према протону показују губитак воде, HCN или бензена из пиридинонског прстена у првом кораку MS^2 фрагментација. Супротно, ако је супституент са високим афинитетом према протону присутан на фенилном прстену у 4-положају пиридинона, сложени фрагментациони путеви углавном зависе од јачине те интеракције. Елиминације неутралних молекула CO, HCN, H_2O, PhH (бензен) или Ph и CN радикала су фрагментациони процеси уобичајени за сва испитивана једињења у наредним фрагментационим ступњевима.

(Примљено 6. јуна, ревидирано 24. октобра 2008)

REFERENCES

1. V. P. Litvinov, S. G. Krivokolysko, V. D. Dyachenko, *Chem. Heterocyc. Compd.* **35** (1999) 509
2. *International Drug Directory*, the Swiss Pharmaceutical Society Edition, Medfarm, Stuttgart, 1994/95, pp. 71, 805, 1062
3. M. C. Seidel, K. L. Viste, R. Y. Yih, US Patent 3503986 (1970)
4. M. C. Seidel, K. L. Viste, R. Y. Yih, US Patent 3576814 (1971)
5. M. C. Seidel, K. L. Viste, R. Y. Yih, US Patent 3761240 (1973)
6. P. Beak, *Acc. Chem. Res.* **10** (1977) 186

7. P. Beak, J. B. Covington, J. M. Zeigler, *J. Org. Chem*. **43** (1978) 177
8. A. Maquestiau, Y. Van Haverbeke, C. De Meyer, A. R. Katritzky, M. J. Cook, A. D. Page, *Can. J. Chem*. **53** (1975) 490
9. M. J. Cook, S. El-Abbady, A. R. Katritzky, C. Guimon, G. J. Pfister-Guillouzo, *J. Chem. Soc., Perkin Trans. 2* (1977) 1652
10. M. J. Novak, L. Lapinski, J. Fulara, A. Les, L. Adamowicz, *J. Phys. Chem.* **96** (1992) 1562
11. S. Kambe, K. Saito, A. Sakurai, T. Hayashi, *Synthesis* **12** (1977) 841
12. D. Mijin, A. Marinković, *Synth. Commun*. **36** (2006) 193
13. C. Reichardt, *Solvents and Solvent Effects in Organic Chemistry*, Wiley, Weinheim, 2003, p. 113
14. J. Barker, *Mass Spectrometry*, Wiley, Chichester, 1999
15. A. D. Marinković, A. A. Perić-Grujić, B. Ž. Jovanović, N. Ilić, M. Nevešćanin, *Rapid Commun. Mass Spectrom*. **20** (2006) 2630.

Journal of the Serbian Chemical Society
JSCS@tmf.bg.ac.rs • www.shd.org.rs/JSCS

J. Serb. Chem. Soc. 74 (3) 237–244 (2009) UDC 547.421+577.175.53+547.448:537.363
JSCS–3826 *Original scientific paper*

Western blot analysis of glucocorticoid receptor phosphoisoforms by one- and two-dimensional electrophoretic assays

NATAŠA POPOVIĆ[1], ANA NIĆIFOROVIĆ[1], MIROSLAV ADŽIĆ[1], MARIJA B. RADOJČIĆ[1]*, CONSTANTINOS DEMONACOS[2] and MARIJA KRSTIĆ-DEMONACOS[3]

[1]*Vinča Institute of Nuclear Sciences, Department of Molecular Biology and Endocrinology, Belgrade, Serbia,* [2]*School of Pharmacy, University of Manchester, Manchester and* [3]*Faculty of Life Sciences, University of Manchester, Manchester, United Kingdom*

(Received 17 October 2007, revised 27 August 2008)

Abstract: The glucocorticoid receptor (GR) protein is a cytosolic ligand-dependent transcription factor with numerous functions regulated by post-translational modifications, including phosphorylation/dephosphorylation. Among the functions most extensively affected by GR phosphorylation are the modulation of its transcriptional activity, alterations in its interaction pattern with cofactors, nuclear translocation and selective gene transactivation. Intensive analysis of the intracellular distribution of GR phosphoisoforms and their interaction with proteins of other cellular signalling networks required the use of [γ^{32}P]ATP as a phosphate donor, and special laboratory protection measures to avoid external irradiation and contamination. In the present study, simple and easy-to-use non-radioactive protein mobility shift assays (NMS assays) were developed using one- and/or two-dimensional gel electrophoresis based on differences in the pI and molecular mass of GR phosphoisoforms. The GR isoforms were immunodetected with specific monoclonal or polyclonal anti-GR antibodies by Western blot in three diverse systems, namely yeast BJ2168 cells expressing wild-type rat GR, rat hepatoma GRH2 cells grown in culture and brain tissue from Wistar rat experimental animals. The results obtained using the NMS assay were similar to previous results obtained with the [γ^{32}P] ATP standard assay.

Keywords: glucocorticoid receptor; phosphoisoforms; electrophoretic assay.

INTRODUCTION

The glucocorticoid receptor (GR) protein is a ligand-dependent transcriptional factor which, in the absence of glucocorticoid hormones (GCs), is located primarily in the cytoplasm of the target cell in the form of a hetero-oligomeric

* Corresponding author. E-mail: marija@vinca.rs
doi: 10.2298/JSC0903237P

complex with heat shock proteins (HSPs).[1,2] After binding to GCs, the GR undergoes conformational changes, dissociates from the HSPs, homodimerizes and translocates into the nucleus where it interacts directly with its specific DNA sequences in the promoter region of the target genes.[1] In addition, the activated GR may interact with other transcription factors, such as the nuclear factor-κB, the activator protein-1 and many others, *via* protein–protein interactions, thus influencing indirectly the activity of these transcription factors on their target genes.[3,4]

Phosphorylation is a very important post-translational modification of GR, regulated by cellular enzymes kinases and phosphatases, influencing and modulating virtually all of the GR functions.[5,6] The *N*-terminal domain of rat GR contains phosphorylation sites at the amino acids serine 224/232 and serine 246, activated by cyclin-dependent kinases (CDKs) and c-Jun-*N*-terminal kinase (JNK), respectively.[7,8] GR phosphorylation by these kinases affects its transcriptional activity, protein stability and nucleo-cytoplasmic shuttling, thus modulating GR-mediated gene expression.[5,9,10] For an understanding of the physiological functions of GR, it is of crucial importance to have simple and accurate method(s) for analysis of the phosphoisoforms of GR. Such methods would enable studies of intracellular distribution of GR phosphoisoforms and their interaction with proteins of other cellular signalling networks. Most of the recently used methods employed radioactively labelled phosphate donor [γ-^{32}P]ATP to follow GR phosphorylation *in vivo* or *in vitro*.[7–10] Although powerful, these techniques required special laboratory protection protocols due to possible external irradiation and contamination by the high levels of [γ-^{32}P]ATP radioactivity.[7,10]

In the present study, simple and easy-to-use non-radioactive protein mobility shift assays (NMS assays) were developed for the analysis of GR phosphoisoforms based on the differential mobility of GR phosphoisoforms separated by the one- or two-dimensional gel electrophoresis. The hyperphosphorylated GR isoform was detected by highly specific monoclonal anti-GR antibodies or epitope specific polyclonal antibodies by Western blot immunodetection assay. The NMS assays were first established *in vivo* with yeast *Saccharomyces cerevisiae* BJ2168 strain expressing wild-type rat GR and thereafter successfully applied to test *in vivo* phosphorylation of GR in rat hepatoma GRH2 cells grown in culture or brain tissue from Wistar rat experimental animals. The obtained results suggest that NMS assays can be used across very different biological systems from yeast cell to *in vivo* animal models with high sensitivity and reproducibility and provide an alternative way to study this subject and avoid using [γ-^{32}P]ATP.[7,10]

EXPERIMENTAL

Baker's yeast Saccharomyces cerevisiae *strains and plasmids*

The triple protease deficient yeast strain BJ2168 (a, pep 4-3, prc 1-417, prb 5-1122, ura 3-52, trp 1, leu 2)[11] served as the parent for derivative strains containing various 2μ-origin--based expression and reporter vectors. Transformations were performed by the lithium ace-

tate procedure.[12] The yeast expression plasmid pG-N795[13,14] contained rat GR cDNA driven by the yeast glyceraldehyde-3-phosphate dehydrogenase promoter, residing on a 2μ vector (10–40 copies per cell) bearing the TRP1 selectable marker. The 2μ vector carries the URA3 selectable marker, a bacterial origin of replication and the bacterial ampicillin resistance gene.[14] Yeast cultures were propagated at 30 °C in minimal yeast medium supplemented with a standard mixture of amino acids and 2 % glucose.[15]

Mammalian cells culture

The mammalian cell line GRH2, a derivative of transfected hepatoma HTC cells, expressing a high level GR was used in the study.[16] Cells were grown in 90 % Dulbecco's modified Eagle's medium H-16, supplemented with 10 % heat-inactivated FCS, 100 IU/mL penicillin and streptomycin and 2 mM L-glutamine (all obtained from Sigma-Aldrich, Taufkirchen, Germany) in 95 % humidity atmosphere of 95 % air and 5 % CO_2 at 37 °C.

Hormone treatment and preparation of yeast and GRH2 cell extracts

Yeast and GRH2 cells were treated *in vivo* with 10 μM deoxycorticosterone (DOC, 3300 ng/mL medium) or 10 μM dexamethasone (Dex, 3900 ng/mL medium), respectively. The yeast cell extract was prepared (1:2 mass/volume) at 4 °C by glass bead lysis in 45 mM Hepes pH 7.4, containing 10 % glycerol, 1 mM Na_2EDTA, 400 mM NaCl, 1 mM DTT and 0.5 % Nonidet P40 followed by centrifugation at 13,000 rpm in a Beckman JA centrifuge. When indicated, the supernatant was treated for 30 min at 25 °C with 20 IU/mL of calf intestine phosphatase (Boehringer Mannheim). The GRH2 cell extract was prepared in the same manner as the yeast extract except that the glass beads were omitted.

Preparation of cell extracts from brain cortex of experimental animals

Wistar males (2 months old, body mass 250 g) were exposed to acute stress (immobilization),[17] sacrificed by decapitation and the prefrontal brain cortex (PFC) was weighed and homogenized (1:2 mass/volume) at 4 °C in 20 mM Tris HCl buffer pH 7.2, containing 10 % glycerol, 1 mM Na_2EDTA, 1 mM Na_2EGTA, 50 mM NaCl, 2 mM DTT and protease inhibitors.[17] The homogenate was centrifuged at 38000 rpm for 60 min at 4 °C and the resulting supernatant was used as cell cytosol.

The protein concentration in the yeast and mammalian cell extracts or brain cell cytosol was determined by the method of Lowry.[18]

Separation and analysis of samples by one-dimensional gel electrophoresis (1-DE) or two-dimensional gel electrophoresis (2-DE)

For analysis by 1-DE, samples (60 μg of protein) were mixed (1:1) in denaturing buffer according to Laemmli[19] and separated by molar mass (M_m) in 7.5 % slab polyacrylamide gels for 45 min at 100 V under denaturing conditions. Standard mixture of M_m marker proteins (Sigma SDS6H2), containing: equine myosine (220000 g/mol), *Escherichia coli* β-galactosidase (116000 g/mol), rabbit muscle phosphorylase B (97400 g/mol), bovine albumin (66000 g/mol) and egg white ovalbumin (45000 g/mol), was used for 1-D gel calibration.

In 2-DE, samples (100 μg of protein) were first mixed with isofocusing buffer (9 M urea, 2 % Triton X-100, 5 % β-mercaptoethanol, 2 % of ampholines (4 volumes of ampholine pH 5–7 plus 1 volume of ampholine pH 3–10) and 0.1 % Bromphenol Blue), and separated according to isoelectric point (pI) in prefocused 4 % disk polyacrylamide gels. The gels were prefocused for 20 min at 200 V, then 20 min at 300 V and 20 min at 400 V before sample isofocusing was run for 10 min at 500 V and then 3.5 h at 750 V. For pI calibration, the following pI markers were run in parallel gel disks: soybean trypsin inhibitor (TI, pI = 4.6),

bovine carbonyl anhydrase (CA, pI = 5.9) and equine myoglobin (Myo, pI = 7.0). The sample disks were taken out of the glass tubes, incubated for 60 min in denaturing buffer according to Laemmli[19] and layered on top of 7.5 % slab polyacrylamide denaturing gels (the same those used in 1-DE). The electrophoretic separation according to molar mass (M_m) was performed for 90 min at 120 V.

Western blot immunodetection of GR protein

Proteins separated by 1-DE or 2-DE were electrophoretically transferred to PVDF membranes and blocked for 1 h at room temperature in phosphate buffered saline (PBS) containing 5 % non-fat dry milk. Immunopositive bands were detected either with GR-specific BUGR2 (gift from Professor Keith R. Yamamoto) monoclonal antibody or with M-20 (sc-1004, Santa Cruz Biotechnology) polyclonal antibody, both prepared in PBST (PBS, 0.1 % Tween 20, 2.5 % milk). After extensive washing (3–5 times for 10 min in PBST), the immunopositive bands were visualized by secondary goat-anti mouse or goat-anti rabbit antibody linked to alkaline phosphatase (ALP)[20] or horseradish peroxidase chemiluminescences (ECL) detection system.[17]

RESULTS AND DISCUSSION

An electrophoretic mobility shift assay, also called “gel shift assay”, is a common technique usually used to study protein–DNA or protein–RNA interactions by 1-D electrophoresis (1-DE). In the present report, it is shown that 1-DE and 2-DE methods can also be successfully applied for monitoring the phosphorylation or dephosphorylation of a single protein, *i.e.*, glucocorticoid receptor (GR) isolated from yeast *Saccharomyces cerevisiae* cells or mammalian cells. As may be observed in Fig. 1A (lanes 1, 3 and 5), the native unliganded GR expressed in yeast (*S. cerevisiae* strain BJ2168) resolved by 1-DE was detected by Western blot using specific anti-GR monoclonal antibodies (BUGR) as a single protein band corresponding to the position of the phosphorylase B marker at 97400 g/mol. Upon addition of the yeast GR specific hormone analogue deoxycorticosterone (10 μM, *i.e.*, 3300 ng DOC/mL medium, K_d 4 nM),[15,21] a “smeared” GR pattern appeared with a GR band corresponding to M_m of about 99000 g/mol (99kGR) (Fig. 1A, lanes 2, 4 and 6). The shift in the M_m of GR was observed in the interval of 50–100 μg of total proteins assayed per lane (Fig. 1A, ALP detection) up to 200 μg of total proteins assayed (Fig. 1B, ECL detection). Earlier studies[3,10] in *S. cerevisiae* BJ2168 mutant strains carrying the GR serine 232 site targeted by CDK for phosphorylation mutated to alanine showed that the ligand-dependent shift in the M_m of GR corresponds to its hyper-phosphorylated form.[3,10] In order to check if the 99kGR was actually a hyper-phosphorylated form of the GR, a control experiment in which BJ2168 extract was treated *in vitro* with 20 IU/mL of calf intestine phosphatase was performed (Fig. 1B). As may be observed, the ligand-dependent 99kGR was not present after the phosphatase treatment (Fig. 1B, lane 4). This fact complements and extends previous findings[10] and provides a strong indication that 99kGR band was indeed the hyper-phosphorylated isoform of GR.

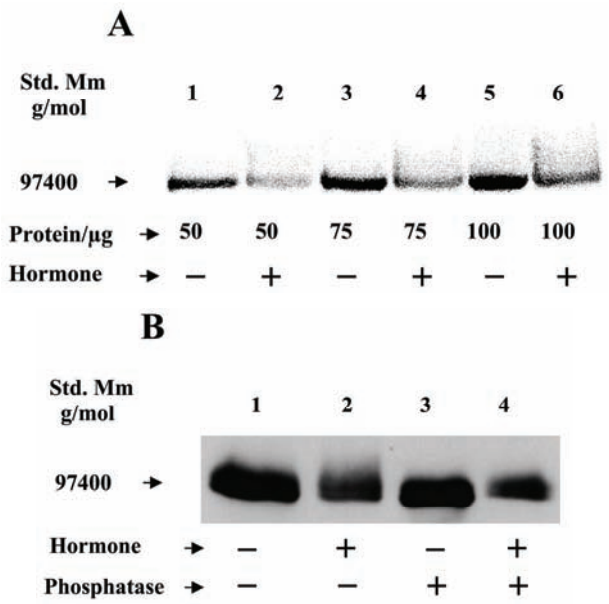

Fig. 1. Western blot analysis of yeast BJ2168 ectopically expressing GR separated by 1-DE. A) Titration of protein concentration 50, 75 or 100 µg and mobility shift: controls (lanes 1, 3, and 5), and yeast GR after hormone treatment (lanes 2, 4 and 6). B) Mobility shift sensitivity to phosphatase treatment: controls (lanes 1 and 3), yeast GR after hormone treatment (lanes 2 and 4) and after calf intestine phosphatase (lanes 3 and 4). The position of molar mass standard (Std. M_m) phosphorylase B (97400 g/mol) is indicated by an arrow.

When untreated or DOC treated BJ2168 extracts were resolved by 2-DE (1--isoelectrofocusing and 2-separation according to molar mass) and screened by BUGR, both pI and M_m shifts were observed (Fig. 2, left and right panels, respectively). The ligand-bound, hyper-phosphorylated and activated form of GR[22] was shifted towards both higher M_m and more acidic pI. The same 2-DE analysis was performed with GRH2 cell extracts after *in vivo* treatment with 10 µM Dex (3900 ng Dex /mL medium, K_d 4nM,[23] Fig. 3). A similar, although less pronounced, shift in the M_m and pI of GR was observed, indicating that GR phosphoisoforms may be also analysed by the 2-DE of rat hepatoma GRH2 cells in culture.

Finally, GR phosphorylation was assayed by the 1-DE shift-assay in extracts isolated from Wistar rat brain tissue. The prefrontal brain cortex extracts which contain high levels of GR protein[24] were prepared from control animals in which the natural hormone corticosterone (CORT) was at a low diurnal level, *i.e.*, 130 ng/mL plasma (Fig. 4, lane 1). The cytosol was also prepared from stressed animal brain corresponding to 630 ng of CORT/mL plasma (Fig. 4, lane 2). The 1-DE analysis followed by Western blot detection of GR by specific M-20 polyclonal antibodies clearly showed the appearance of both 97.4kGR and 99kGR hormone-dependent hyperphosphorylated isoform under high CORT conditions.

These results provide evidence that the employed method may be successfully applied to separate these phosphoisoforms *in vivo* in whole animal studies. Moreover, in recent publication in which serine 232 epitope specific anti-GR antibodies were used, the hyperphosphorylated isoform with reduced mobility (99kGR) was shown to be a CDK phosphorylated form of GR in Wistar rat brain.[17]

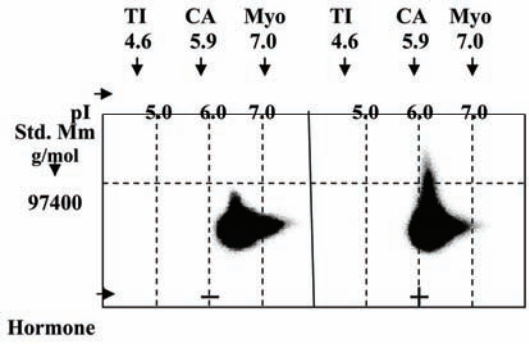

Fig. 2. Western blot analysis of yeast BJ2168 ectopically expressing GR separated by 2-DE. Left panel: the control sample; right panel: the sample treated with hormone. The positions of the pI standards: soybean trypsin inhibitor (TI, pI = 4.6), bovine carbonic anhydrase (CA, pI = 5.9) and equine myoglobin (Myo, pI = 7.0), and the position of the molar mass standard (Std. M_m) phosphorylase B (97400 g/mol) are indicated by dashed lines.

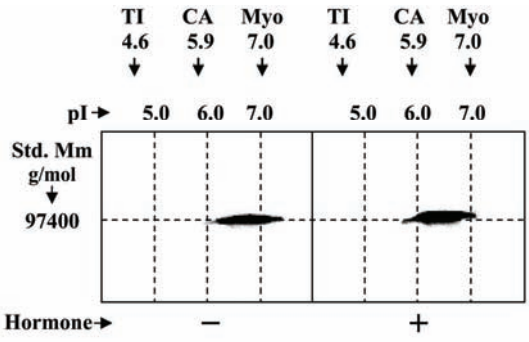

Fig. 3. Western blot analysis of the GR from rat liver GRH2 cells separated by 2-DE. Left panel: the control sample; right panel: the sample treated with hormone (10 μM Dex). The position of the pI standards: soybean trypsin inhibitor (TI, pI = 4.6), bovine carbonic anhydrase (CA, pI = 5.9) and equine myoglobin (Myo, pI = 7.0), and the position of the molar mass standard (Std. M_m) phosphorylase B (97400 g/mol) are indicated by dashed lines.

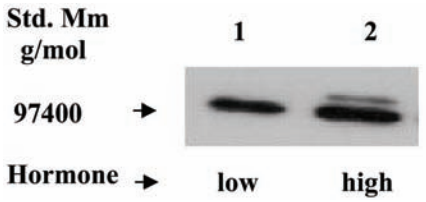

Fig. 4. Western blot analysis by specific M-20 antibodies of the GR from the prefrontal cortex of Wistar rat brain separated by 1-DE: control sample with low hormone level (130 ng/mL CORT) (Lane 1) and a stressed animal with a high hormone level (630 ng/mL CORT), (Lane 2). The position of the molar mass standard (Std. M_m) phosphorylase B (97400 g/mol) is indicated by an arrow.

CONCLUSIONS

The non-radioactive electrophoretic protein mobility shift assays (NMS assays) used in the present study are equivalent to a standard radioactivity based assay using [γ-^{32}P]ATP as a phosphate donor. Instead of the radioactivity detection

method, the NMS assay is based on Western blot immunodetection of GR phosphoisoform separated in one- and/or two dimensional gels according to differences in pI and molar mass. The GR forms are easily detected in all the studied biological systems and GR undergoes hormone dependent phosphorylation in yeast as well as in mammals, suggesting the importance and conservation of this process. In addition, these GR isoforms can be detected and quantified with high sensitivity and reproducibility, thus enabling the avoidance of the use of the [γ-^{32}P]ATP assay; and the method does not require special laboratory protection measures. The NMS assay may be used to analyse GR from the diverse biological systems: yeast cells, mammalian cells (rat hepatoma GRH2 culture) and brain tissue from experimental animals.

Acknowledgement. The work was supported by the Grants No. 03E24 and No. 143042B from the Ministry of Science and Technological Development of the Republic of Serbia.

ИЗВОД

«WESTERN BLOT» АНАЛИЗА ФОСФОИЗОФОРМИ ГЛУКОКОРТИКОИДНОГ РЕЦЕПТОРА ПОМОЋУ ЈЕДНОДИМЕНЗИОНАЛНЕ И ДВОДИМЕНЗИОНАЛНЕ ЕЛЕКТРОФОРЕЗЕ

НАТАША ПОПОВИЋ[1], АНА НИЋИФОРОВИЋ[1], МИРОСЛАВ АЦИЋ[1], МАРИЈА Б. РАДОЈЧИЋ[1], CONSTANTINOS DEMONACOS[2] И МАРИЈА КРСТИЋ-DEMONACOS[3]

[1]Институт за нуклеарне науке "Винча", Лабораторија за молекулану биологију и ендокринологију, Београд, [2]School of Pharmacy, University of Manchester, Manchester и [3]Faculty of Life Sciences, University of Manchester, Manchester, United Kingdom

Глукокортикоидни рецептор (ГР) је цитосолни лиганд-зависни транскрипциони фактор чије бројне функције су регулисане пост-транслационим модификацијама: фосфорилацијом и дефосфорилацијом. Међу функцијама ГР које су најосетљивије на фосфорилацију су: модулација његове транскрипционе активности, промене у начину интеракције са кофакторима, транслокација ГР у једро и селективна трансактивација гена. У литератури су до сада описане бројне анализе унутарћелијске дистрибуције ГР и његове интеракције са протеинима других сигналних путева, које су засноване на [γ-^{32}P]ATP као донору фосфатне групе. За овакве анализе потребне су специјалне лабораторијске мере заштите од зрачења и радиоактивне контаминације. У приказаној студији развили смо једноставан и лак нерадиоактивни тест («NMS») за анализу ГР фосфоизоформи који се заснива на промени у њиховој покретљивости у једнодимензионалној или дводимензионалној електрофорези, као последици разлика у pI и молекулској маси. Фосфоизоформе ГР су анализиране у три различита биолошка система: у квасцу BJ2186 са дивљим типом («wild-type») ГР, у ћелијама хепатома пацова GRH2 гајеним у култури и у можданом ткиву експерименталних Wistar пацова. Анализа фосфоизоформи ГР је рађена имунолошком методом помоћу високо-специфичних моноклонских или поликлонских антитела коришћених у «Western blot» тесту. Резултати добијени «NMS» тестом били су слични нашим претходним резултатима у којима је коришћен стандардни [γ-^{32}P]ATP тест.

(Примљено 17. октобра 2007, ревидирано 27. августа 2008)

REFERENCES

1. A. Y. So, C. Chaivorapol, E. C. Bolton, H. Li, K. R. Yamamoto, *PLoS Genet.* **3** (2007) e94
2. D. Ricketson, U. Hostick, L. Fang, K. R. Yamamoto, B. D. Darimont, *J. Mol. Biol.* **368** (2007) 729
3. H. F. Luecke, K. R. Yamamoto, *Genes Dev.* **19** (2005) 1116
4. I. Rogatsky, J. C. Wang, M. K. Derynck, D.F. Nonaka, D.B. Khodabakhsh, C.M. Haqq, B.D. Darimont, M.J. Garabedian, K. R. Yamamoto, *Proc. Natl. Acad. Sci. USA* **100** (2003) 13845
5. M. J. Garabedian, I. Rogatsky, A Hittelman, R. Knoblauch, J. M. Trowbridge, M. D. Krstić, *Molecular Biology of Steroid and Nuclear Hormone Receptors*, Birkhauser, Boston, 1998, p. 237
6. Z. Wang, W. Chen, E. Kono, T. Dang, M. J. Garabedian, *Mol. Endocrinol.* **21** (2007) 625
7. M. D. Krstić, I. Rogatsky, K. R. Yamamoto, M. J. Garabedian, *Mol. Cell. Biol.* **17** (1997) 3947
8. M. Krstić-Demonacos, C. Demonacos, In *Recent Research Developments in Molecular and Cellular Biology*, S. G. Pandalai, Ed., Research Signpost, Trivandrum, India, 2001, p. 57
9. T. Kino, T. Ichijo, N. D. Amin, S. Kesavapany, Y. Wang, N. Kim, S. Rao, A. Player, Y. L. Zheng, M. J. Garabedian, E. Kawasaki, H. C. Pant, G. P. Chrousos, *Mol Endocrinol.* **21** (2007) 1552
10. N. Pocuca, S. Ruzdijić, C. Demonacos, D. T. Kanazir, M. Krstić-Demonacos, *J. Steroid Biochem. Mol. Biol.* **66** (1998) 303
11. E. W. Jones, *Genetics* **85** (1977) 23
12. H. Ito, Y. Fukuda, K. Murata, A. Kimura, *J. Bacteriol.* **153** (1983) 163
13. M. Schena, K. R. Yamamoto, *Science* **241** (1988) 965
14. M. Schena, L. P. Freedman, K. R. Yamamoto, *Genes Dev.* **3** (1989) 1590
15. J. M. Garabedian, K. R. Yamamoto, *Mol. Biol. Cell* **3** (1992) 1245
16. J. N. Vanderbilt, R. Miesfeld, B. A. Maler, K. R. Yamamoto, *Mol. Endocrinol.* **1** (1987) 68
17. M. Adžić, J. Djordjević, A. Nićiforović, M. B. Radojčić, M. Krstić-Demonacos, *3rd CSSI Congress on Stress*, Budapest, Hungary, 2007, Book of Abstracts, Section 7B-20-P, p. 423
18. O. H. Lowry, N. J. Rosebrough, A. L. Farr, R. J. Randall, *J. Biol. Chem.* **193** (1951) 265
19. U. K. Laemmli, *Nature* **227** (1970) 680
20. B. Gametchu, R. W. Harrison, *Endocrinology* **114** (1984) 274
21. D. Failla, G. M. Tomkins, D. V. Santi, *Proc. Natl. Acad. Sci. USA* **72** (1975) 3849
22. M. Kalimi, P. Colman, P. Feigelson, *J. Biol. Chem.* **250** (1975) 1080
23. M. Beato, P. Feigelson, *J. Biol. Chem.* **247** (1972) 7890
24. K. Fuxe, A.-C. Wikstrom, S. Okret, L. F. Agnati, A. Harfstrand, Z. Y. Yu, L. Granholm, M. Zoli, W Vale, J.-A. Gustafsson, *Endocrinology* **117** (1985) 1083.

Journal of the Serbian Chemical Society
JSCS@tmf.bg.ac.rs • www.shd.org.rs/JSCS
J. Serb. Chem. Soc. 74 (3) 245–257 (2009) UDC 616.981.55+615.9+547.281.1+547.963.1
JSCS–3827 *Original scientific paper*

The monoclonal antibody 26 raised against tetanus toxoid also recognizes tetanus toxin and β_2-glycoprotein I – its binding properties *in vitro* and potential applications

ALEKSANDRA B. INIĆ-KANADA*, MARIJANA M. STOJANOVIĆ, IRENA P. ŽIVKOVIĆ, VLADIMIR Ž. PETRUŠIĆ and LJILJANA A. DIMITRIJEVIĆ

Institute of Virology, Vaccines and Sera – Torlak, Vojvode Stepe 458, 11152 Belgrade, Serbia

(Received 17 July, revised 7 November 2008)

Abstract: A murine monoclonal IgG_1 antibody, marked as MAb26, specific for tetanus toxoid has been immunochemically characterized. By performing enzyme-linked immunosorbent assays (ELISAs) and western blot analyses, it was demonstrated that MAb26 reacted with tetanus toxoid, tetanus toxin and β_2-glycoprotein I (β_2GPI). According to the results, MAb26 recognized the sequential epitope on the tetanus heavy chain. The affinity constant, calculated from Scatchard plots of MAb26 binding to tetanus toxoid, was 1.145×10^8 M^{-1} and the measurement of the relative affinity of MAb26 by ELISA using thiocyanate elution showed a significantly higher affinity of MAb26 to the toxoid (p = = 0.0012) in comparison to the toxin. Additionally, the reactivity of MAb26 toward the toxoid forms increased when the tetanus toxin was detoxified using 8 mM and higher formaldehyde concentrations. The similarity of the tetanus toxoid to several sera proteins, either at the level of its conformation (IL-1α) or at the level of peptide sequences (β_2GPI, laminin) favors its role in autoimmunity by the mechanism of molecular mimicry. As the induction of an autoimmune disease is dependent on the breakdown of tolerance, which could be the result of an overt hyperstimulation, the control of the presence and concentration of self-reactive epitopes in vaccine preparations is a prerequisite. In this study, it was shown that MAb26 can: 1) discriminate between the tetanus toxin and different toxoid forms, which makes it a good candidate for antibody control during vaccine preparation; 2) due to its cross-reactivity with β_2GPI, it could provide information on the presence of a potentially dangerous sequential epitope expressed at the protein surface.

Keywords: tetanus toxoid; tetanus toxin; monoclonal antibodies; formaldehyde.

INTRODUCTION

Tetanus toxin (TTn) is an enormously potent neurotoxin[1] secreted by the anaerobic soil bacterium, *Clostridium tetani* and is comprised of two polypeptide

* Corresponding author. E-mail: aleksandra612@gmail.com
doi: 10.2298/JSC0903245I

chains, termed heavy (H, 100 kD) and light (L, 50 kD) chains, linked by a disulphide bond. These two chains are functionally distinct; the H chain is responsible for binding and cell entry, while the L chain is catalytically active and functions as a zinc-dependent endopeptidase. TTn traffics to the central nervous system by retrograde axonal transport followed by trans-synaptic spread into inhibitory interneurons,[2,3] where it specifically cleaves the synaptic vesicle protein synaptobrevin. Synaptobrevin cleavage by TTn blocks the release of inhibitory neurotransmitters leading to spastic paralysis. In concentration of approximately 1 ng/kg,[4] TTn induces death in non-vaccinated humans.

As TTn induces death before an adaptive immunity could be generated, active immunization[5] with tetanus vaccine (TTdV) is crucial for the prevention of death caused by tetanus. At present, protection is routinely induced through immunization with a TTn derivate, tetanus toxoid (TTd), obtained by chemical modification with formaldehyde,[6] which was first described more than 80 years ago. TTn inactivated by formaldehyde is devoid of toxicity but is still highly immunogenic with a stabilized native conformation.

The similarity between TTn and several sera proteins (β_2GPI, laminin) at the level of short peptide sequences favors its role in autoimmunity by the mechanism of molecular mimicry.[7,8] This fact implies that the application of TTd requires prior detailed characterization and precise quantification. The cross-reactivity of TTn, especially with β_2GPI drew our attention as it has been shown that β_2GPI is a major antigen in the antiphospholipid syndrome (APS).[9]

With the intent of examining further the specificity of anti-tetanus antibodies, an anti-tetanus monoclonal antibody (MAb), marked as MAb26, which recognizes the epitope located on both forms of tetanus: natural toxin and its chemical derivative, toxoid, was immunochemically characterized. In addition, MAb26 cross-reacted with β_2GPI and could be regarded as a convenient tool for an investigation related to the potential generation of some "surprising" and potentially hazardous anti-β_2GPI autoantibodies, possibly through the molecular mimicry mechanism. There is a general consensus that autoimmune diseases depend on genetic and environmental factors. As studies on experimental APS models proved that there is molecular mimicry between β_2GPI-related synthetic peptides and structures within bacteria and viruses, TTd, might be a cause for experimental APS.[10] Since the pathogenic potential of MAb26 *in vivo* has already been demonstrated,[11] this study was conducted with the aim of further analyzing the immunochemical characteristics of MAb26, with the emphasis on the analysis of the reactivity of MAb26 toward different tetanus antigenic determinants. The obtained results also indicate that formaldehyde modification potentiates the conformational expression of β_2GPI cross-reactivity.

EXPERIMENTAL

Antigens

TTn was purified from fermentation cultures of *Clostridium tetani* and inactivated at a fixed concentration of 180 Lf/ml by adding formaldehyde to final concentrations of 0, 2, 4, 8, 16, 32, 64 and 128 mM. The mixture was adjusted to pH 7.4 and incubated at 35 °C for 4 weeks. The resulting "detoxified samples" were then dialyzed and filtered to remove the excess of inactivation reagents. After a final pH adjustment and filtration, the samples were aliquoted and used in the experiments. In the following text, when the formaldehyde concentration is not specifically indicated, the abbreviation TTd refers to the tetanus toxoid obtained using 128 mM formaldehyde.

β_2GPI was purified from normal human plasma using sequential precipitation with $(NH_4)_2SO_4$, 65 % saturation, from the supernatant obtained following perchloric acid addition to human plasma (final concentration 1.75 %) and chromatographic steps (Mono S column; ÄKTA Purifier, Pharmacia Amersham, Uppsala, Sweden). Both Ags were checked for purity by SDS-PAGE (Phast System, Pharmacia Amersham, Uppsala, Sweden) and identified by immunoblot, using either commercially available mouse anti-human β_2GPI IgG1 (IgG1; clone 5F7, ICN Biomedicals, Aurora, USA) or anti-TTd standard antibodies.

Production of MAbs specific for TTd

MAbs to TTd were produced by the hybridoma technology.[12] MAb26 was IgG_1 which was demonstrated by ELISA, using commercially available biotin-labeled MAbs specific for mouse IgG subclasses (ICN Biomedicals, Aurora, USA) for detection. MAb26 producing hybridoma was cultured in integra bottles (Integra CL 350, Integra Biosciences, Switzerland) and the MAb was affinity purified from the supernatant on a Protein A-Sepharose 6B (Pharmacia Amersham, Uppsala, Sweden) column according to the instructions of the manufacturer. The purity of MAb preparations were determined by sodium dodecylsulphate polyacrylamide gel electrophoresis (SDS-PAGE). The isolated MAb26 was used for $F(ab')_2$ and Fab' production according to a procedure previously described.[13] The resulting proteolytic digestion samples were dialyzed against 100 mM Tris-HCl buffer, pH 8.1, and intact Fc fragments and non-digested antibody were removed by Protein A-Sepharose chromatography. The $F(ab')_2$ preparation showed a single band at 100 kD and a doublet of bands at 25 kD in non-reducing and reducing SDS-PAGE, respectively. The Fab' preparation showed a single band at 50 kD and 25 kD in non-reducing and reducing SDS-PAGE, respectively. The obtained antigen-binding fragments, as well as intact MAbs were biotin labeled (–B) according to a previously described procedure.[14]

Reactivity of MAb26 with TTn and TTd

ELISA plates (MaxiSorp, Nunc) were covered (50 µl/well) with TTn or TTd (1µg ml^{-1} PBS) by overnight adsorption at 4 °C. A 1 % BSA/PBS solution was used for blocking non-specific binding for 2 h at room temperature). The saturation, as well as each subsequent ELISA step, was followed by washing with 0.05 % Tween 20/PBS (4×200 µl/well). MAb26 (0.50–10 µg/ml) was added to the plate and incubated for 1 h at room temperature. Biotin--labeled antibodies specific for mouse IgG (ICN) (50 µl/well) were incubated for 1 h at room temperature. The system extrAvidin-peroxidase/OPD was used for "visualization" of Ag–Ab interaction. The absorbance was read at 492/692 nm.

The measurement of the relative MAb26 affinity by ELISA using thiocyanate elution

The affinities of MAb26 to TTd and TTn were estimated by use of aqueous solutions containing different potassium thiocyanate (KSCN) concentrations.[15] Analysis of the in-

fluence of thiocyanate ion (SCN^-) on the specific MAb26 binding was performed with ELISA-based procedures. The protocol was similar to those performed for the reactivity determination of MAb26 with TTd and TTn. The single difference was an additional 1-hour incubation with aqueous KSCN solutions after the binding of MAb26 to the adsorbed Ags. Aqueous solutions containing increasing KSCN concentrations (0–6 M) were employed for MAb26 desorption. The SCN^- concentration ($[SCN^-]$) that induced a 50 % reduction of initial absorbance ($[SCN^-]_{50\ \%}$) was calculated for each sample upon linearization of the corresponding Ag–Ab dissociation profile (Binding (%) = $f([SCN^-])$). A preliminary experiment showed that KSCN in the concentrations used did not induce desorption of coated TTd or TTn. To evaluate the significance of the observed differences in MAb26 affinity toward TTd and TTn, dissociation profiles (Binding (%) = $f([SCN^-])$ were compared by a paired Student's *t*-test.

Reactivity of MAb26 with TTn adsorbed onto gangliosides

ELISA plates (PolySorp, Nunc) were covered (50 µl/well) with the appropriate ganglioside: GT_{1b} or GD_{1b} (10 µg/ml in methanol) by overnight evaporation at room temperature. A 1 % BSA/PBS solution was used for saturation for 2 h at room temperature. The saturation, as well as each subsequent ELISA step, was followed by washing with PBS (4×200 µl/well). TTn/1 % BSA (20 µg /ml) or 1 % BSA were added to the plate and incubated for 1 h at 37 °C. MAb26 (10 µg/ml) or TTd-specific mouse anti-serum (polyclonal anti-TTd Abs, 1:400) were added to the plate and incubated for 1 h at 37 °C. After washing, the biotin-labeled antibodies specific for mouse IgG (ICN) was added to the plate (50 µl/well). System extrAvidin-peroxidase/OPD was used for "visualization" of the Ag–Ab interaction. The absorbance was read at 492/692 nm.

SDS-PAGE and Western blot

TTn, TTd and β_2GPI were resolved by SDS-PAGE on 1-mm-thick 9 % separating gels, with 4 % stacking gels (Mini Protean II System, Bio-Rad, USA). The proteins were electrophoretically transferred to PVDF membranes (Millipore Corporation, Bedford, MA, USA) for 1 h at 4 °C and 1–1.5 mA/cm^2 (Multiphor II System, LKB, Sweden) in buffer containing 25 mM Tris (Pharmacia), 193 mM glycine (Pharmacia), and 15 % methanol (Fluka). To prevent non-specific antibody binding, the membranes were incubated with blocking buffer, 3 % BSA (Sigma) in PBS for 2 h. MAb26 was diluted in blocking buffer and the incubations were performed for 1 h at room temperature. The membranes were incubated with anti-mouse IgG-B (Sigma) diluted 1:5000, followed by streptavidin–phosphatase (Sigma) diluted 1:1000. The membranes were washed three times with 0.05 % Tween 20 (Sigma)/PBS and twice with PBS after the incubations. The antibody binding was visualized by exposure to 5-bromo-4-chloro-3-indolyl phosphate/nitro blue tetrazolium (BCIP/NBT) (Bio-Rad).

SDS-PAGE under reducing conditions was performed similarly to that described above with the following differences: 1) the proteins were resolved by electrophoresis on a gradient 4.0–15 % polyacrylamide gel (Pharmacia) and 2) the samples contained 5 % 2-mercaptoethanol.

Reactivity of MAb26 with β_2*GPI*

ELISA plates (MaxiSorp, Nunc) were covered (50 µl/well) with β_2GPI (10 µg/ml β_2GPI/PBS) by overnight adsorption at 4 °C. A 1 % BSA/PBS solution was used for saturation for 2 h at room temperature. The saturation, as well as each subsequent ELISA step, was followed by washing with 0.05 % Tween 20/PBS (4×200 µl/well). MAb26 (0.50–10 µg/ml) was added to the plate and incubated for 1 h at room temperature. The biotin-labeled antibodies specific for mouse IgG (ICN) (50 µl/well) were incubated for 1 h at room tem-

perature. The system extrAvidin-peroxidase/OPD was used for "visualization" of the Ag–Ab interaction. The absorbance was read at 492/692 nm.

Competitive inhibition ELISA: binding of MAb26 for β_2GPI in the presence of differently detoxified forms of TTn

The β_2GPI was bound to the MaxiSorp (Nunc) microtiter plates by overnight adsorption at 4 °C, at a concentration of 10 μg/ml. Detoxified samples (20 μg/ml), made by adding formaldehyde to final concentrations of 0, 2, 4, 8, 16, 32, 64 and 128 mM, were mixed with $F(ab')_2$ MAb26, 10 μg/ml, then pre-incubated for 1 h at 25 °C in a water bath and further incubated with β_2GPI coated on the microplate walls. ExtrAvidin-peroxidase/OPD was used as the detection system. The percentage binding (*BI*) was calculated after determination of the free MAb26 from the standard curve $A_{492/692} = f((F(ab')_2MAb26))$.

Double immunodiffusion

Double immunodiffusion[16] was performed for subclass determination and for the detection of the precipitating properties of MAb26.

RESULTS AND DISCUSSION

Preliminary tests, performed with supernatants of hybridoma 26, indicated that MAb26 reacts with TTd, TTn and β_2GPI. The hybridoma 26, secreting MAb26 of the IgG1 subclass (pI 7.4), was further subcloned, propagated in Integra bottles and characterized. Although this characterization included the conventional approach to study MAbs, the focus was on the investigation of the unusual binding features of MAb26, the localization of its partial epitope and potential applications.

Binding properties of MAb26

The reactivity of the isolated MAb26 toward TTd and TTn was tested using direct ELISA and this MAb displayed strong reactivity toward tetanus antigenic determinants. The reactivity pattern undoubtedly demonstrated anti-TTd binding specificity with a K_a value of 1.145×10^8 M^{-1}, determined for isolated TTd (150 kD) in competitive ELISA (Fig. 1a). The reactivity toward TTd was higher in comparison to the reactivity toward TTn, which was confirmed by analysis of the influence of KSCN on MAb26 binding to TTd and TTn (Fig. 1b). Significant differences between the elution profiles of MAb26 from TTn and TTd following incubation with KSCN in various concentration were revealed by paired Student's *t*-test ($p = 0.0012$), indicating a large difference in the affinity of MAb26 toward these antigens. The calculated $[SCN^-]_{50\ \%}$ values confirmed the higher affinity of MAb26 toward TTd compared to TTn. Parallel binding curves of MAb26 and its $F(ab')_2$ and Fab' fragments for TTd or TTn revealed the same binding pattern, which excluded the necessity of bivalent binding of MAb26 (Fig. 2), which is in accordance with the high affinity of MAb26 toward these Ags.

The MAb26 was also reacted with β_2GPI. It was not possible to calculate the affinity of MAb26 toward β_2GPI by the standard Scatchard method. The first reason could be its low affinity toward β_2GPI and the second, probably more im-

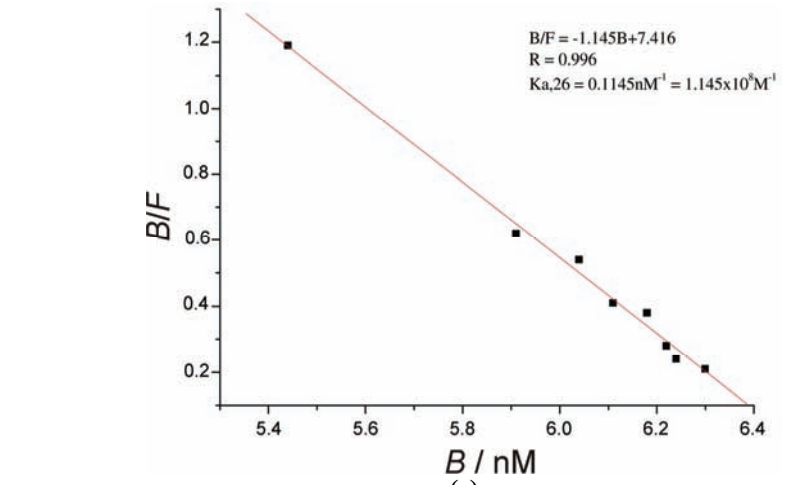

(a)

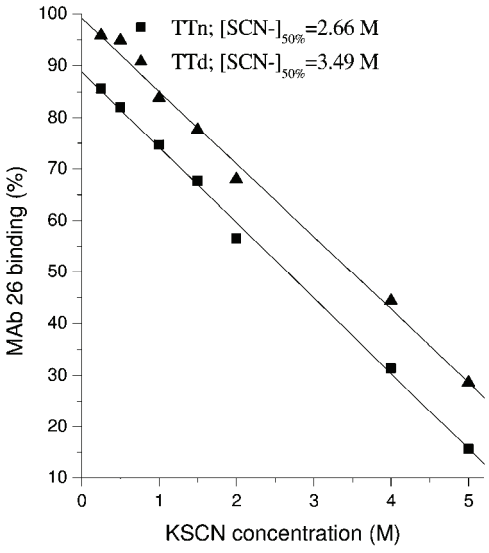

(b)

Fig. 1. a) Scatchard plot ($B/F = f(B)$) of the binding of MAb26 to TTd measured by ELISA at 25 °C, B – concentration of MAb26 bound to TTd, F – concentration of free MAb26, and b) measurement of the relative affinity of MAb26 toward TTn and TTd by ELISA using thiocyanate elution. The corresponding $[SCN^-]_{50\,\%}$ values are indicated within the graph.

portant, is the requirement of its bivalent binding.[17] The necessity to use a high concentration of β_2GPI (10 μg/ml) for the detection of MAb26 binding implies a low affinity of MAb26 toward β_2GPI (Fig. 3a). Bivalent binding of MAb26 to β_2GPI could explain the non-linear dependence of MAb26 binding to β_2GPI following its incubation with solutions containing different concentration of KSCN and the relatively high value of $[SCN^-]_{50\,\%}$ (Fig. 3b). Finally, as was shown in a previous study,[11] the absence of Fab' binding to β_2GPI adsorbed in a concentration which allows the detection of MAb26, but the presence of binding

of intact MAb26 and its F(ab')$_2$ to β_2GPI, confirmed the requirement of bivalent binding of MAb26 to β_2GPI.

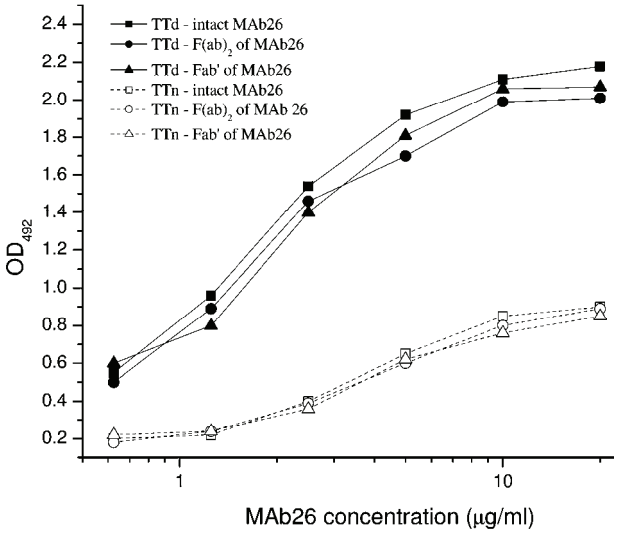

Fig. 2. Binding curves of MAb26 and its F(ab')$_2$ and Fab' fragments to TTd and TTn.

Partial characterization of the MAb26 binding epitope

Western blot revealed that MAb26 recognized the band of 150 kD in TTd/ /TTn and cross-reacted with β_2GPI (Fig. 4a). These results suggest that the epitope recognized by MAb26 was most probably sequential and not dependent on the native structure of TTd/TTn or β_2GPI. Further Western blot experiments performed after SDS-PAGE obtained under reducing conditions revealed that MAb26 binding epitope most probably lies on the tetanus heavy chain (Fig. 4b).

The reactivity of MAb26 toward different detoxified samples, made by adding formaldehyde to final concentrations of 0, 2, 4, 8, 16, 32, 64 and 128 mM, was tested by ELISA. It could be seen (Fig. 5) that the reactivity of MAb26 increased when the Ags were used in which the TTn had been detoxified using 8 mM and higher formaldehyde concentrations. A similar MAb26 binding pattern was revealed by Western blot (Fig. 6b) performed after SDS-PAGE obtained under reducing conditions with detoxified samples (Fig. 6a).

The results of MAb26 binding to TTn adsorbed directly onto a microtiter plate or a microtiter plate pre-coated with gangliosides supported the hypothesis that the epitope recognized by MAb26 is located on the H chain of the TTn/TTd molecule. The gangliosides (GD_{1b} and GT_{1d}) represent natural receptors for TTn and the ganglioside binding site is located on the C-terminal domain of the H chain of TTn. It was shown (Fig. 7) that adsorption of TTn to gangliosides almost completely inhibited its recognition by MAb26, most probably due to steric hindrance.[18]

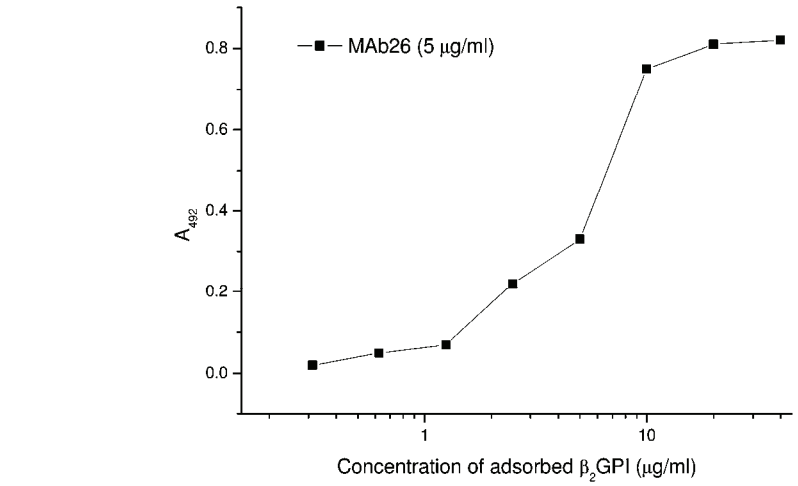

(a)

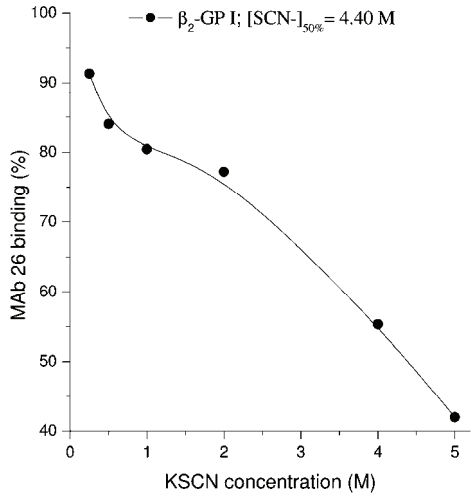

(b)

Fig. 3. a) Binding curve of MAb26 to increased β_2GPI concentrations adsorbed onto a MaxiSorp microtiter plate and b) measurement of the relative affinity of MAb26 toward β_2GPI by ELISA using thiocyanate elution. The corresponding $[SCN^-]_{50\,\%}$ values are indicated within the graph.

The observed differences in reactivity of MAb26 toward the different toxoid forms might be the result of the different extent of chemical modification and this fact could eventually be used for discrimination between TTn and the toxoid forms or to confirm the efficient transformation of TTn to toxoid forms.

Cross-reactivity of MAb26 with β_2*GPI*

By using "detoxified TTd samples" as inhibitors of MAb26–β_2GPI binding, an attempt was made to evaluate whether the formaldehyde concentration used in the detoxification process could have any impact on the structure of the β_2GPI-like epitope on the TTd molecule. It is evident that the β_2GPI-like epitope was pre-

sent in the TTn molecule and was potentiated through conformational changes induced by formaldehyde treatment. A 50 % inhibition of binding $F(ab')_2$ MAb26 to β_2GPI was obtained in the presence of as little as 4 mM formaldehyde in the TTn detoxification process (Fig. 8). This result could favor the possibility that the native conformation is stabilized by the formaldehyde-induced cross-links.

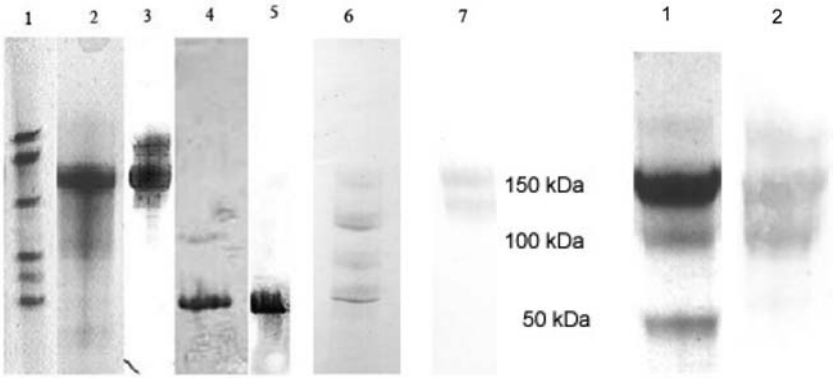

Fig. 4. a) SDS-PAGE of TTd (lane 2), β_2GPI (lane 4) and TTn (lane 6) on a 9 % polyacrylamide gel and Western blot analysis of MAb26 TTd (lane 3), β_2GPI (lane 5) and TTn (lane 7). The molecular weight marker kit (lane 1) consisted of myosin (212 kD), α-macroglobulin (170 kD), β-galactosidase (116 kD), transferrin (76 kD) and glutamic dehydrogenase (53 kD), (b) SDS-PAGE of TTd under reducing conditions and Western blot analysis.

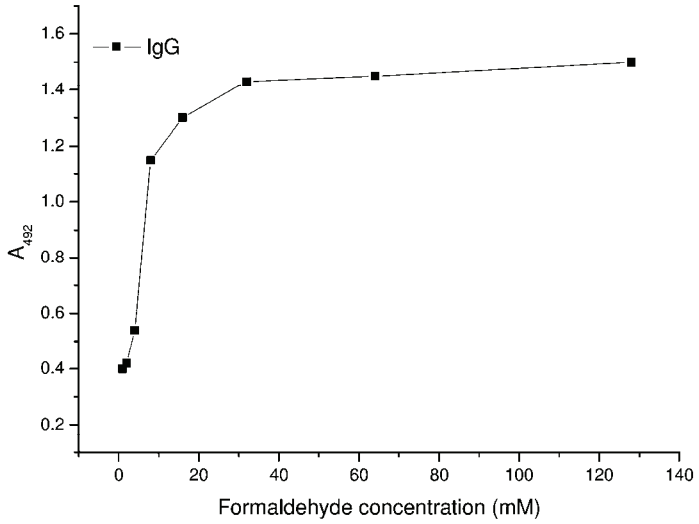

Fig. 5. Binding of MAb26 to different detoxified samples (made by adding formaldehyde to final concentrations of 0, 2, 4, 8, 16, 32, 64 and 128 mM) immobilized directly onto a UV-irradiated MaxiSorp plate. All the samples were assayed in triplicate and the mean ±*SD* are presented.

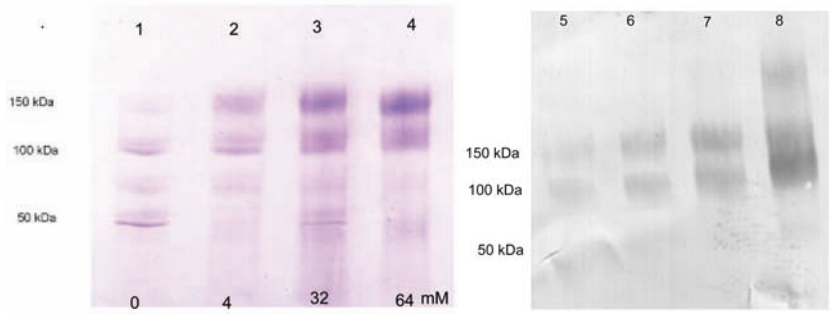

(a) (b)

Fig. 6. SDS-PAGE of detoxified samples (with 0, 4, 8, 32 and 64 mM formaldehyde) under reducing conditions on a gradient 4–15 % PAG (a) and Western blot analysis of former samples 1–4 with MAb26 as 5–8, respectively (b).

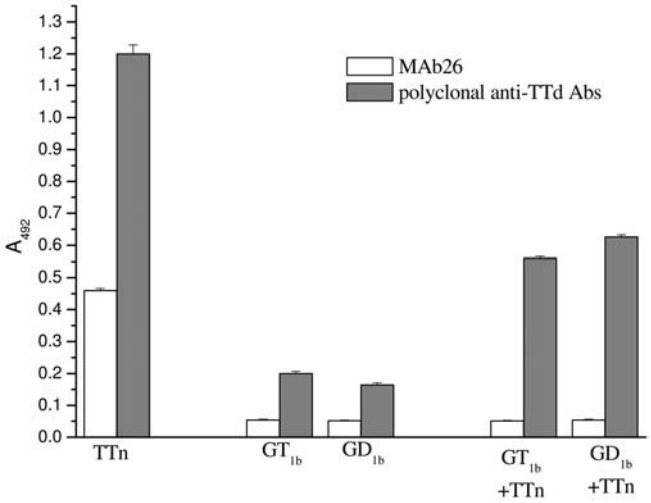

Fig. 7. Binding of MAb26 to TTn, gangliosides and TTn + gangliosides. Polyclonal anti-TTd anti-serum was used as the positive control.

MAb26 is cross-reactive with β_2GPI and might be employed as a convenient tool for investigations related to the potential generation of anti-β_2GPI autoantibodies, possibly by the molecular mimicry mechanism. The theory of molecular mimicry, one of the mechanisms thought to be responsible for the association of autoimmunity with infections, involves the display of epitopes resembling the host determinants by the infectious agent. The epitope of a pathogen may induce an immune response that breaks down self-tolerance by cross-reactivity, thus inducing an auto-immune response leading to disease. The involvement of molecular mimicry and immunization with TTd in the induction of APS was demonstrated in experimental animal models.[19–21] In a previous study,[11] experimental APS in BALB/c mice (which are not lupus-prone, *i.e.* the mice were not geneti-

cally predisposed to autoimmune diseases) was induced after they had been passively infused with MAb26.

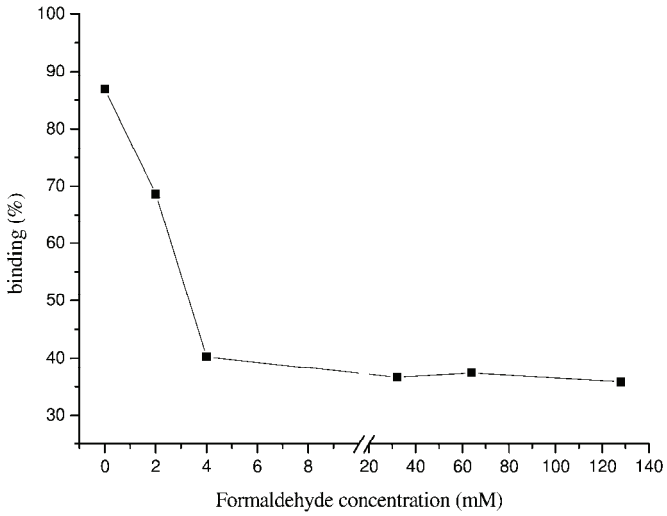

Fig. 8. Inhibition of MAb26 binding to β_2GPI in the presence of differently detoxified forms of TTn.

As the induction of autoimmune disease is dependent on the breakdown of tolerance, which could be the result of overt hyperstimulation, control of the presence and concentration of self-similar epitopes in vaccine preparations is a prerequisite. This favors MAb26 as a valuable tool in the preparation process of a tetanus toxoid vaccine.

Precipitating properties of MAb26

In addition to the characterization of MAb26, it was shown that this MAb precipitated TTd and TTn in solution and also exhibited good precipitating properties in gels, as demonstrated by double immunodiffusion (Figs. 9a and 9b).

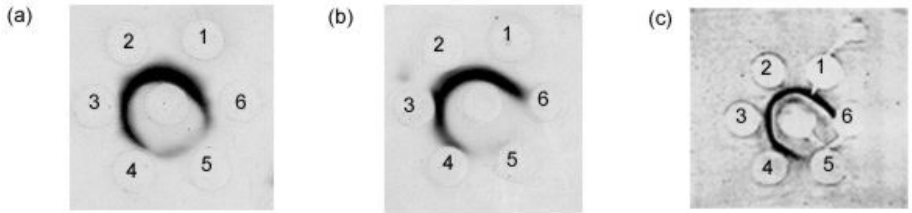

Fig. 9. Double immunodiffusion of MAb26 against TTd, TTn and β_2GPI performed in a 1.0 % agarose gel. TTd (a), TTn (b) and β_2GPI (c) were placed in the central wells at a concentration of 1.0 mg/ml. The concentrations of MAb26 that were placed in the peripheral wells were 2-fold dilutions starting with 0.50 (well 1), 0.25 (well 2), 0.125 (well 3), 0.0625 (well 4), 0.03125 (well 5) and ending with 0.015 mg/ml (well 6).

Although MAb26 could not precipitate β_2GPI in solution which is in accordance with data from the literature for anti-β_2GPI Abs, MAb26 exhibited good precipitating properties in gels (Fig. 9c).

CONCLUSIONS

According to the presented results, it can be concluded that the characterized MAb26 could be employed as a control antibody during vaccine preparation. Its different affinities toward tetanus toxin and toxoid might be used for following-up the detoxification process, which is indispensable for vaccine production. On the other hand, the cross reactivity with β_2GPI could expand the information of the presence of a potentially dangerous sequential epitope expressed at the protein surface after detoxification.

Acknowledgements. This investigation was supported by grant 142020 from the Ministry of Science of the Republic of Serbia.

ИЗВОД

МОНОКЛОНСКО АНТИТЕЛО 26 НАПРАВЉЕНО НА ТЕТАНУС ТОКСОИДУ РЕАГУЈЕ И СА ТЕТАНУС ТОКСИНОМ И β_2-ГЛИКОПРОТЕИНОМ I – КАРАКТЕРИСТИКЕ ВЕЗИВАЊА *IN VITRO* И МОГУЋА ПРИМЕНА

АЛЕКСАНДРА Б. ИНИЋ-КАНАДА, МАРИЈАНА М. СТОЈАНОВИЋ, ИРЕНА П. ЖИВКОВИЋ, ВЛАДИМИР Ж. ПЕТРУШИЋ и ЉИЉАНА ДИМИТРИЈЕВИЋ

Институт за вирусологију, вакцине и серуме "Торлак", Војводе Степе 458, 11152 Београд

Овај рад описује имунохемијску карактеризацију мишјег IgG1 моноклонског антитела означеног као MAт26. Ензимским имуносорбентним тестом (ELISA) и Western blot анализом је показано да MAт26 реагује са тетанус токсоидом, тетанус токсином и β_2-гликопротеином I (β_2GPI). Према нашим резултатима, MAт26 препознаје секвенциони епитоп на тешком ланцу молекула тетануса. Константа афинитета MAт26 за тетанус токсоид, израчуната на основу Скачардовог дијаграма, је $1{,}145\times10^8$ M^{-1}. На основу елуције тиоцијанатом, коришћене за одређивање релативног афинитета MAт26 за тетанус токсин и тетанус токсоид, поступком базираним на ELISA-и, показан је знатно већи (p = 0,0012) афинитет MAт26 ка токсоидној форми. Такође, реактивност MAт26 ка токсоидној форми расла је са порастом концентрације формалдехида, почевши од 8 mM, коришћеног у процесу детоксификације. Сличност тетанус токсоида са различитим серумским протеинима на нивоу конформације и/или пептидних секвенција (β_2GPI, ламинин) указује на његову потенцијалну улогу у индукцији аутоимуности механизмом молекулске мимикрије. Будући да настанак аутоимунске болести подразумева нарушавање толеранције, на пример, прекомерном стимулацијом имунског система, контрола присуства и концентрације себи сличних епитопа се намеће као неопходна. У овом раду је показано да: 1) MAт26 може да прави разлику између тетанус токсина и различитих токсоидних форми што га чини потенцијално добрим антителом које би се користило у контроли током производње вакцина; 2) захваљујући унакрсној реактивности са β_2GPI, MAт26 може да пружи информације о присуству потенцијално опасних епитопа на површини протеина.

(Примљено 17. јула, ревидирано 7. новембра 2008)

REFERENCES

1. C. Fotinou, P. Emsley, I. Black, H. Ando, H. Ishida, M. Kiso, K. A. Sinha, N. F. Fairweather, N. W. Isaacs, *J. Biol. Chem.* **276** (2001) 32274
2. K. Sinha, M. Box, G. Lalli, G. Schiavo, H. Schneider, M. Groves, G. Siligardi, N. Fairweather, *Mol. Microbiol.* **37** (2000) 1041
3. L. Simpson, *Annu. Rev. Pharmacol. Toxicol*. **26** (1986) 427
4. H. Brüggemann, S. Bäumer, W. F. Fricke, A. Wiezer, H. Liesegang, I. Decker, *Proc. Natl. Acad. Sci. USA* **100** (2003) 1316
5. M. A. Manghi, M. F. Pasetti, M. L. Brero, *J. Immunol. Methods* **168** (1994) 17
6. B. Bizzini, A. Turpin, M. Raynaud, *Ann. Inst. Pasteur* **116** (1969) 688
7. M. Blank, M. Eisenstein, R. A. Ascherson, R. Cervera, Y. Schoenfeld, in *Infection and Autoimmunity*, Y. Schoenfeld, N. Rose, Eds., Elsevier, Amsterdam, 2004, p. 473
8. European Bioinformatics Institute – European Molecular Biology Laboratory, Cambridgeshire, UK, http://www.ebi.ac.uk/t-coffee/ (2 June, 2008)
9. M. Blank, I. Krause, M. Fridkin, N. Keller, J. Kopolović, I. Goldberg, A. Tobar, Y. Shoenfeld, *J. Clin. Invest.* **109** (2002) 797
10. Y. Shoenfeld, M. Blank, R. Cervera, J. Font, E. Raschi, P. Meroni, *Ann. Rheum. Dis.* **65** (2006) 2
11. A. Inić-Kanada, M. Stojanović, I. Živković, D. Kosec, M. Mićić, V. Petrušić, S. Živančević-Simonović, Lj. Dimitrijević, *Am. J. Reprod. Immunol.* **61** (2009) 39
12. S. Šeatović, A. Inić-Kanada, M. Stojanović, I. Živković, R. M. Jankov, L. Dimitrijević, *J. Immunoassay Immunochem.* **25** (2004) 31
13. A. Johnstone, R. Thorpe, *Immunochemistry in Practice*, Blackwell Scientific Publications, Oxford, 1987, p. 48
14. V. T. Updyuke, L. G. Nicolson, *J. Immunol.* **73** (1984) 83
15. R. A. MacDonald, C. S. Hosking, C. L. Jones. *J. Immunol. Methods* **106** (1988) 191
16. O. Ouchterlony, *Prog. Allergy* **5** (1958) 1
17. Y. Sheng, A. Kandiah, S. Krilis, *J. Immunol.* **15** (1998) 2038
18. P. Emsley, C. Fotinou, I. Black, N. F. Fairweather, I. G. Charles, C. Watts, E. Hewitt, N. W. Isaacs, *J. Biol. Chem.* **24 (**2000) 8889
19. A. Piona, L. La Rosa, A. Tincani, D. Faden, G. Magro, S. Grasso, F. Nicoletti, G. Balestrieri, P. L. Meroni, *Scand. J. Immunol.* **41** (1995) 427
20. M. Blank, J. Cohen, V. Toder, Y. Shoenfeld, *Proc. Natl. Acad. Sci. USA* **15** (1991) 3069
21. D. W. Branch, D. J. Dudley, M. D. Mitchell, K. A. Creighton, T. M. Abbott, E. H. Hammond, R. A. Daynes, *Am. J. Obstet. Gynecol.* **63** (1990) 210.

Journal of the Serbian Chemical Society
JSCS@tmf.bg.ac.rs • www.shd.org.rs/JSCS

J. Serb. Chem. Soc. 74 (3) 259–267 (2009)
JSCS–3828

UDC 547.594.4+547–326+
+546.742'562'472':543.51
Original scientific paper

Unsaturated β-ketoesters and their Ni(II), Cu(II) and Zn(II) complexes

MUHAMMED BASHEER UMMATHUR[1]*, KRISHNANNAIR KRISHNANKUTTY[2] and SINDHU BALAGOPAL[2]

[1]*Department of Chemistry, Unity Women's College, Manjeri, Kerala-676122 and* [2]*Department of Chemistry, University of Calicut, Kerala-673635, India*

(Received 15 May, revised 14 July 2008)

Abstract: A new series of β-ketoesters in which the keto group is attached to the olefinic linkage were synthesized by the reaction of methyl acetoacetate and aromatic aldehydes under specified conditions. The existence of these compounds predominantly in the intramolecularly hydrogen bonded enol form was well demonstrated from their IR, ^{1}H-NMR and mass spectral data. Details on the formation of their [ML_2] complexes with Ni(II), Cu(II) and Zn(II) and the nature of the bonding are discussed on the basis of analytical and spectral data.

Keywords: unsaturated β-ketoesters; metal complexes; IR; ^{1}H-NMR; mass spectra.

INTRODUCTION

Numerous reports exist on the synthesis, characterization and applications of metal complexes of β-ketoesters in which the keto group is attached to alkyl/aryl functions.[1] However, no systematic investigation has appeared on β-ketoesters in which the keto group is linked to an olefinic linkage. In recent years such "unsaturated" β-dicarbonyl compounds and their metal complexes have gained considerable importance[2–12] mainly because of the observation that the active constituents of several medicinal plants contain such compounds. A typical example is curcuminoids, the active chemical constituents of turmeric (*Curcuma longa*, Linn., Zingiberaceae family), a traditional Indian medicinal plant.[5,6] These natural curcuminoids were reported to possess anticancer,[7] antitumor,[8] anti-oxidant,[8,9] anti-inflammatory,[10] antiviral and immunomodulatory activities.[11] Synthetic curcuminoids are reported to be more potent anticarcinogenic and antimutagenic[12] agents. Therefore, investigations on such unsaturated carbonyl systems and their metal complexes have tremendous importance. In continuation of our studies on unsaturated polycarbonyl compounds and their metal com-

* Corresponding author. E-mail: mbummathur@rediffmail.com
doi: 10.2298/JSC0903259U

plexes,[2,3,13,14] the synthesis and characterization of a new series of "unsaturated" β-ketoesters and their typical metal complexes are reported herein.

EXPERIMENTAL

Methods and instruments

Carbon, hydrogen and nitrogen percentages were determined by microanalyses (Heraeus Elemental analyzer) and the metal contents of the complexes by AAS (Perkin Elmer 2380). The electronic spectra of the compounds in methanol (10^{-4} mol/L) were recorded on a 1601 Shimadzu UV–Vis spectrophotometer, IR spectra (KBr discs) on an 8101 Shimadzu FTIR spectrophotometer, ^{1}H-NMR spectra ($CDCl_3$ or DMSO-d_6) on a Varian 300 NMR spectrometer and mass spectra on a Jeol/SX-102 mass spectrometer (FAB using Argon and *m*-nitrobenzyl alcohol as the matrix). The molar conductance of the complexes was determined in DMF (≈10^{-3} mol/L) at 28±1 °C. Magnetic susceptibilities were determined at room temperature on a Gouy-type magnetic balance.

Synthesis of the unsaturated β*-ketoesters HL[1]–HL[6]*

The aldehydes used for the preparation of unsaturated β-ketoesters were: benzaldehyde, naphthalene-1-carbaldehyde, 4-hydroxybenzaldehyde, vanillin, 4-(dimethylamino)benzaldehyde and 2-hydroxynaphthalene-1-carbaldehyde. A typical procedure for the synthesis is given below.

Methyl acetoacetate (1.16 g, 0.010 mol) and boric oxide (0.35 g, 0.0050 mol) were mixed and made into a paste with dry ethyl acetate and stirred for ≈ 1 h at room temperature. To this, a solution of aromatic aldehyde (0.010 mol) and tri(*sec*-butyl) borate (4.6 g, 0.020 mol), dissolved in dry ethyl acetate (≈ 15 mL), was added and stirred for ≈ 5 h with the slow addition of *n*-butylamine (0.50 mL in 5.0 mL dry ethyl acetate) and the reaction mixture was kept overnight. HCl (0.40 M, 7.5 mL) was added and the mixture again stirred for ≈ l h. Subsequently, the mixture was extracted repeatedly with ethyl acetate and the combined extracts were evaporated to dryness on a water bath. The obtained pasty mass was stirred with methanol (15 mL) for ≈ 2 h and was then kept in an ice bath under constant stirring for ≈ 3 h. The precipitated compound was filtered and recrystallized from hot benzene thus producing the chromatographically (TLC, silica gel as adsorbent) pure compound.

Synthesis of Cu(II), Ni(II) and Zn(II) complexes

To a refluxing solution of the unsaturated β-ketoester in ethanol (0.0020 mol, 20 mL), an ethanolic solution of metal(II) acetate (0.0010 mol, 15 mL) was added dropwise under stirring. The pH of the solution was adjusted to around 6 using sodium acetate and the refluxing was continued for ≈ 3 h. The solution was then concentrated to half its volume and cooled to room temperature. The precipitated complex was filtered, washed with water, then with methanol, and finally recrystallized from hot ethanol.

RESULTS AND DISCUSSION

A well-established synthetic route to "unsaturated" β-dicarbonyl compounds is based on the synthesis of curcuminoids[5] using the reaction of aromatic aldehydes and acetylacetone in presence of boric oxide, tri(*sec*-butyl) borate and *n*-butylamine. The use of boric oxide and tri(*sec*-butyl) borate is to prevent the Knoevenagel-type condensation and facilitate the Claisen-type condensation by the formation of a boron complex of the diketone. This reaction usually yields a mixture of both the mono and bis-condensation products. In the present study,

when methyl acetoacetate was employed, only the monocondensation product was formed.

The compounds were stable, showed sharp melting points and were soluble in common organic solvents. The formulas and elemental analytical data of the unsaturated β-ketoesters synthesized from various aromatic aldehydes are given in Tables I and II. The analytical data (Table III) together with their non-electrolytic nature in DMF (the specific conductance of a 10^{-3} mol/L solution was < 10 Ω^{-1} cm^{-1}) suggest $[ML_2]$ stoichiometry of the complexes. The Ni(II) and Zn(II) chelates were diamagnetic, while the Cu(II) complexes showed a normal paramagnetic moment. The observed electronic, IR, ^{1}H-NMR and mass spectra were fully consistent with the presentation of unsaturated β-ketoesters (Scheme 1) and of the complexes (Scheme 2).

TABLE I. Abbreviations of the prepared β-ketoesters and Ar constituent

Compound	Ar-
HL^1	Phenyl
HL^2	1-Naphthyl
HL^3	4-Hydroxyphenyl
HL^4	3-Hydroxy-4-methoxyphenyl
HL^5	4-(Dimethylamino)phenyl
HL^6	2-Hydroxy-1-naphthyl

IR spectra

Methyl acetoacetate exists predominantly in the keto form with a very small percentage of the enol form[15] and exhibits the most characteristic bands in the region 1600–1800 cm^{-1}, due to the ester carbonyl at ≈ 1750 cm^{-1}, the acetyl carbonyl at ≈ 1720 cm^{-1} and the β-hydroxy-α,β-unsaturated ester carbonyl of the enol form at ≈1650 cm^{-1}. The spectra of all the unsaturated β-ketoesters showed three strong bands at ≈ 1740 cm^{-1}, ≈ 1670 cm^{-1} and ≈ 1640 cm^{-1}, assignable to the stretching of the ester carbonyl, the β-hydroxy-α,β-unsaturated ester carbonyl of the enol form and the cinnamoyl carbonyl function[16] (Table IV). The spectra of all the compounds showed a prominent band at ≈ 970 cm^{-1} typical of the *trans*--CH=CH– group.[17] The broad band in the region 2800–3500 cm^{-1} suggests the existence of the compounds predominantly in the intramolecularly hydrogen bonded enolic form.[17]

The spectra of all the complexes showed an intense and slightly broadened band at ≈ 1630 cm^{-1} in the 1600–1800 cm^{-1} region (Table V). In the metal chelates of methyl acetoacetate both the acetyl and ester carbonyls show an appreciable decrease in frequencies upon complexation.[15] Therefore, by considering its position and shape it can be presumed that this band originates from a metal bonded dicarbonyl function. The broad band in the region 2800–3500 cm^{-1} was absent in the spectra of the metal complexes, indicating the replacement of the eno-

TABLE II. Analytical, ^{1}H-NMR and mass spectral data of the prepared unsaturated β-ketoesters

Compound	M.p. °C	Yield %	Elemental Analysis Found (Calculated), %			^{1}H-NMR (δ/ppm)					Mass spectral data *m/z*
			C	H	N	Enolic OH	Ester OCH_3	Methine	CH_2	Aryl substituent	
HL^1	54	72	70.49	5.89	–	12.168	3.128	6.768	3.684	–	204, 189, 173, 145,
$C_{12}H_{12}O_3$			(70.59)	(5.88)							131, 127, 103, 101
HL^2	68	70	75.64	5.46	–	12.354	3.098	6.876	3.634	–	254, 239, 223, 195,
$C_{16}H_{14}O_3$			(75.59)	(5.51)							181, 153, 127, 101
HL^3	86	74	65.50	5.44	–	12.358	3.142	6.548	3.634	10.046 (OH)	221, 205, 189, 161,
$C_{12}H_{12}O_4$			(65.45)	(5.45)							147, 127, 119, 101
HL^4	64	70	62.48	5.64	–	13.123	3.292	6.895	3.684	10.154 (OH)	247, 232, 216, 188, 174,
$C_{13}H_{14}O_5$			(62.40)	(5.60)						3.918 (OCH_3)	146, 127, 120, 101
HL^5	57	68	68.12	6.80	5.65	13.258	3.162	6.542	3.568	2.938 ($N(CH_3)_2$)	251, 235, 219, 191, 177,
$C_{14}H_{17}NO_3$			(68.01)	(6.88)	(5.67)						149, 127, 123, 101
HL^6	60	72	71.18	5.14	–	13.160	3.122	6.938	3.546	10.798 (OH)	270, 255, 239, 211, 197,
$C_{16}H_{14}O_4$			(71.11)	(5.19)							169, 143, 127, 101

TABLE III. Physical and analytical data of the isolated Cu(II), Ni(II) and Zn(II) complexes (L – deprotonated ligand (abbreviated as in Table I))

Complex	M.p. °C	Yield %	Elemental Analysis Found (Calculated), %			
			C	H	N	M
$[NiL^1_2]$ $C_{24}H_{22}NiO_6$	210	72	62.09 (61.97)	4.72 (4.73)	–	12.64 (12.63)
$[NiL^2_2]$ $C_{32}H_{26}NiO_6$	202	68	67.98 (68.00)	4.62 (4.60)	–	10.44 (10.40)
$[NiL^3_2]$ $C_{24}H_{22}NiO_8$	236	70	58.04 (57.98)	4.42 (4.43)	–	11.78 (11.82)
$[NiL^4_2]$ $C_{26}H_{26}NiO_{10}$	226	70	55.98 (56.04)	4.69 (4.67)	–	10.56 (10.55)
$[NiL^5_2]$ $C_{28}H_{32}N_2NiO_6$	198	76	61.13 (61.01)	5.82 (5.81)	5.11 (5.08)	10.62 (10.66)
$[NiL^6_2]$ $C_{32}H_{26}NiO_8$	260	68	64.33 (64.35)	4.40 (4.36)	–	9.86 (9.84)
$[CuL^1_2]$ $C_{24}H_{22}CuO_6$	196	74	61.38 (61.34)	4.64 (4.69)	–	13.49 (13.53)
$[CuL^2_2]$ $C_{32}H_{26}CuO_6$	214	70	67.38 (67.42)	4.59 (4.57)	–	11.01 (11.16)
$[CuL^3_2]$ $C_{24}H_{22}CuO_8$	208	72	57.48 (57.42)	4.36 (4.39)	–	12.74 (12.67)
$[CuL^4_2]$ $C_{26}H_{26}CuO_{10}$	176	68	55.52 (55.56)	4.59 (4.63)	–	11.33 (11.32)
$[CuL^5_2]$ $C_{28}H_{32}CuN_2O_6$	192	70	60.42 (60.48)	5.69 (5.76)	4.99 (5.04)	11.42 (11.44)
$[CuL^6_2]$ $C_{32}H_{26}CuO_8$	256	74	63.88 (63.84)	4.30 (4.32)	–	10.60 (10.56)
$[ZnL^1_2]$ $C_{24}H_{22}O_6Zn$	192	70	61.11 (61.10)	4.70 (4.67)	–	13.84 (13.87)
$[ZnL^2_2]$ $C_{32}H_{26}O_6Zn$	188	68	67.24 (67.21)	4.58 (4.55)	–	11.38 (11.44)
$[ZnL^3_2]$ $C_{24}H_{22}O_8Zn$	208	68	57.25 (57.21)	4.34 (4.37)	–	13.02 (12.99)
$[ZnL^4_2]$ $C_{26}H_{26}O_{10}Zn$	186	74	55.43 (55.38)	4.60 (4.62)	–	11.52 (11.60)
$[ZnL^5_2]$ $C_{28}H_{32}N_2O_6Zn$	206	72	60.24 (60.28)	5.68 (5.74)	5.01 (5.02)	11.74 (11.73)
$[ZnL^6_2]$ $C_{32}H_{26}O_8Zn$	252	70	63.68 (63.64)	4.34 (4.31)	–	10.80 (10.84)

lic proton by a metal cation during complexation. The involvement of the carbonyl groups in coordination, as shown in Scheme 2, is further supported by the appearance of two medium intensity bands at ≈ 420 cm^{-1} and ≈ 470 cm^{-1} assignable to ν_{M-O}.[16]

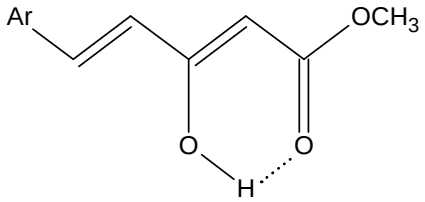

Scheme 1. Presentation of the prepared unsaturated β-ketoesters (abbreviations are given in Table I).

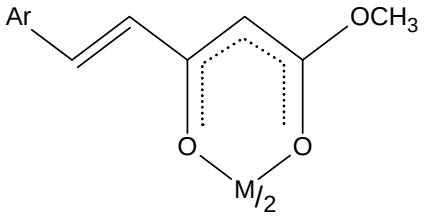

Scheme 2. Simplified presentation of the structure of the metal complexes with unsaturated β-ketoesters. Abbreviations as in Table I.

TABLE IV. Characteristic IR stretching bands (cm^{-1}) of the unsaturated β-ketoesters ($HL^{1–6}$ as in Table I)

HL^1	HL^2	HL^3	HL^4	HL^5	HL^6	Probable assignments
1742	1738	1740	1730	1736	1720	(C=O) Ester
1660	1658	1689	1668	1666	1665	(C=O) Olefinic
1624	1620	1643	1635	1630	1635	(C=O) Cinnamoyl
1591	1590	1597	1580	1582	1577	(C=C) Phenyl/alkenyl
1562	1542	1573	1545	1546	1568	
1546	1536	1546	1528	1528	1520	
1528	1518	1512	1525	1520	1496	
967	969	970	986	970	966	CH=CH *trans*
–	–	3056	3070	–	3066	Phenolic OH

TABLE V. Characteristic IR stretching frequencies (cm^{-1}) and mass spectral data of the prepared Cu(II) complexes

Complex/ Empirical formula	IR bands (cm^{-1})				Mass spectral data (*m*/*z*)
	(C=O) Ester	(C=O) Cinnamoyl	(C=C) Aryl/alkenyl	M–O	
$[CuL^1{}_2]$	1625 *s*	1595 *s*	1556 *s*	428 *m*	469, 451, 440, 438, 409, 407, 368,
$C_{24}H_{22}CuO_6$			1580 *s*	470 *m*	366, 337, 335, 317, 315, 265, 263,
			1542 *m*		204, 201, 189, 173, 127
$[CuL^2{}_2]$	1626 *s*	1593 *s*	1562 *s*	416 *m*	571, 569, 540, 538, 509, 507, 418,
$C_{32}H_{26}CuO_6$			1580 *s*	474 *m*	416, 387, 385, 317, 315, 265, 263,
			1544 *m*		254, 239, 203, 201, 195, 181
$[CuL^3{}_2]$	1630 *s*	1590 *s*	1560 *s*	420 *m*	503, 501, 472, 470, 441, 439, 384,
$C_{24}H_{22}CuO_8$			1584 *s*	470 *m*	382, 353, 351, 317, 315, 265, 263,
			1550 *m*		221, 205, 203, 201, 147, 119
$[CuL^4{}_2]$	1630 *s*	1585 *s*	1567 *s*	416 *m*	563, 561, 532, 530, 501, 499, 414,
$C_{26}H_{26}CuO_{10}$			1577 *s*	487 *m*	412, 383, 381, 317, 315, 265, 263,
			1546 *m*		251, 219, 203, 201, 191, 127, 101
$[CuL^5{}_2]$	1622 *s*	1599 *s*	1561 *s*	416 *m*	557, 555, 526, 524, 495, 493, 411,
$C_{28}H_{32}CuN_2O_6$			1581 *s*	485 *m*	409, 380, 378, 317, 315, 265, 263,
			1545 *m*		247, 232, 203, 201, 174, 120, 101
$[CuL^6{}_2]$	1635 *s*	1590 *s*	1560 *s*	425 *m*	603, 601, 572, 570, 541, 539, 434,
$C_{32}H_{26}CuO_8$			1570 *s*	476 *m*	432, 403, 401, 317, 315, 270, 265,
			1546 *m*		263, 255, 239, 203, 201, 127, 101

^{1}H-NMR spectra

The ^{1}H-NMR spectra of the unsaturated β-ketoesters displayed a one proton singlet at $\delta \approx 13$ ppm due to the intramolecularly hydrogen bonded enolic proton.[18] The olefinic and methylene proton signals appeared at $\delta \approx 6$–7 ppm and $\delta \approx 3$–4 ppm. The aryl proton signals were observed in the δ range 7–7.8 ppm as a complex multiplet. The position and integrated intensities of all the signals (Table II) agree well with the proposed structure of the compounds (Scheme 1).

In the ^{1}H-NMR spectra of the diamagnetic Ni(II) and Zn(II) complexes, the low field enol proton signal of the ligands was absent indicating its replacement by the metal ion during complexation. The OCH_3 proton signal remained almost unaffected. The methylene proton signal was shifted appreciably to low field compared to the shift of the olefinic protons. This may be due to the aromatic character that might have been imparted to the C_3O_2M ring system of the chelates by the highly conjugated groups attached to the dicarbonyl moiety. The integrated intensities of the various signals conform to $[ML_2]$ stoichiometry of the complexes. The aryl substituents were not involved in bonding with the metal ion, which is clearly indicated[2] in the spectra of their Ni(II) and Zn(II) complexes in which the signals remain unaltered.

Mass spectra

Mass spectra of all the unsaturated β-ketoesters showed an intense molecular ion peak, $P^+/(P + 1)^+$, thereby confirming the formulation of the compounds.[19] Peaks due to $(Ar–CH=CH–CO)^+$, $(P – OCH_3)^+$, $(P – COOCH_3)^+$, $(P – ArC_2H_2)^+$, *etc*. are characteristic for all the spectra (Table II). The FAB mass spectra of the Cu(II) complexes showed molecular ion peaks corresponding to $[CuL_2]$ stoichiometry of the complexes. Peaks corresponding to $[CuL]^+$, L^+ and fragments of L^+ were also present in the spectra (Table V). The spectra of all the chelates have a number of fragments containing copper in the 3:1 natural abundance of ^{63}Cu and ^{65}Cu isotopes.

Electronic spectra

The UV spectra of the unsaturated β-ketoesters showed two broad bands with maxima at ≈ 390 nm and ≈ 260 nm due to the various $n\rightarrow\pi^*$ and $\pi\rightarrow\pi^*$ transitions. In the complexes, these absorption maxima were shifted appreciably to lower wave numbers. The Cu(II) complexes showed a broad visible band, λ_{max} at ≈ 15,000 cm^{-1}. This, together with the calculated μ_{eff} values (≈ 1.74 μ_B) suggests square-planar geometry.[20] A broad band centered at ≈ 11000 cm^{-1} observed in spectra recorded in pyridine indicated the formation of octahedral pyridine adducts. The diamagnetism and the broad medium-intensity band at ≈ 17,600 cm^{-1} in the spectra of the Ni(II) chelates suggest their square-planar geometry. In conformity, the spectra of the chelates in pyridine solution (10^{-3}

mol/L) showed three bands corresponding to a configurational change to octahedral due to the association of pyridine. The three well-separated absorption bands at λ_{max} around 8,145, 13,345 and 24,450 cm^{-1} correspond to the transitions: $^3A_{2g} \rightarrow {}^3T_{2g}$; $^3A_{2g} \rightarrow {}^3T_{1g}(F)$ and $^3A_{2g} \rightarrow {}^3T_{1g}(P)$, respectively.

CONCLUSIONS

Six new unsaturated β-ketoesters in which the keto group was attached to an olefinic linkage were synthesized by the reaction of methyl acetoacetate and aromatic aldehydes. Analytical, IR, ^{1}H-NMR and mass spectral data revealed a 1:1 product in which the methyl group of the ester had undergone a Claisen condensation with the aromatic aldehyde. The existence of these unsaturated β-ketoesters in the intramolecularly hydrogen bonded enol form was well demonstrated from their analytical and spectral data. Analytical, physical and spectral data of the [ML_2] complexes of Ni(II), Cu(II) and Zn(II) showed monobasic bidentate coordination in which the intramolecularly hydrogen-bonded enolic proton had been replaced by a metal cation.

ИЗВОД

НЕЗАСИЋЕНИ β-КЕТОЕСТРИ И ЊИХОВИ Ni(II), Cu(II) И Zn(II) КОМПЛЕКСИ

MUHAMMED BASHEER UMMATHUR[1], KRISHNANNAIR KRISHNANKUTTY[2] и SINDHU BALAGOPAL[2]

[1]Department of Chemistry, Unity Women's College, Manjeri, Kerala-676122, India и
[2]Department of Chemistry, University of Calicut, Kerala-673635, India

Реакцијом метил-ацетоацетата и ароматичних алдехида под наведеним условима добијена је нова серија β-кетоестара у којима је кето група припојена олефинској вези. Из њихових IR, ^{1}H-NMR и масених спектралних података показано је постојање ових једињења претежно у енолном облику са интрамолекулском водоничном везом. Детаљи о грађењу њихових [ML_2] комплекса са Ni(II), Cu(II) и Zn(II) и природи веза су дискутовани на основу аналитичких и спектралних података.

(Примљено15. маја, ревидирано 15. јула 2008)

REFERENCES

1. a) R. C. Maurya, S. Rajput, *J. Mol. Struct.* **35** (2004) 687; b) R. Mosteiro, A. Fernandez, M. L. Torrez, D. V. Garcia, A. Saurez, J. J. Fernandez, J. M. Vila, *New J. Chem.* **26** (2002) 1425
2. a) V. D. John, K. Krishnankutty, *Appl. Organomet. Chem.* **20** (2006) 477; b) V. D. John, K. Krishnankutty, *Transition Met. Chem.* **30** (2005) 229; c) K. Krishnankutty, V. D. John, *Synth. React. Inorg. Met.-Org. Chem.* **33** (2003) 343; d) V. D. John, G. Kuttan, K. Krishnankutty, *J. Exp. Clin. Cancer Res.* **21** (2002) 219
3. a) K. Krishnankutty, P. Venugopalan, *Synth. React. Inorg. Met-Org. Chem.* **28** (1998) 1313; b) K. Krishnankutty, P. Venugopalan, *J. Indian Chem. Soc.* **75** (1998) 2
4. S. M. Khopde, K. I. Priyadarsini, P. Venketesan, M. N. A. Rao, *Biophys. Chem.* **80** (1999) 85
5. H. J. J. Pabon, *Rec. Trav. Chim. Pays-Bas* **83** (1964) 237
6. V. S. Govindarajan, *CRC Crit. Rev. Food Sci. Nutr.* **12** (1980) 199

7. a) R. Kuttan, P. C. Sudheeran, C. D. Joseph, *Tumori* **73** (1987) 29; b) R. Kuttan, P. Bhanumathy, K. Nirmala, M. C. George, *Cancer Lett.* **29** (1985) 197; c) K. K. Soudamini, R. Kuttan, *J. Ethnopharmacol.* **27** (1989) 227; d) M. Nagabushan, S. V. Bhide, *J. Am. Cell. Nutr.* **11** (1992) 192
8. R. J. Anto, K. N. D. Babu, K. N. Rajasekharan, R. Kuttan, *Cancer Lett*. **94** (1995) 74
9. K. Elizabeth, M. N. A. Rao, *Int. J. Pharm.* **58** (1990) 237
10. R. C. Srimal, B. N. Dhawan, *J. Pharm. Pharmacol.* **25** (1973) 447
11. S. Antony, R. Kuttan, G. Kuttan, *Immun. Invest.* **28** (1999) 291
12. R. J. Anto, J. Jeorge, K. N. D. Babu, K. N. Rajasekharan, R. Kuttan, *Mutat. Res.* **37** (1996) 127
13. a) K. Krishnankutty, P. Sayudevi, M. B. Ummathur, *J. Serb. Chem. Soc.* **73** (2008) 423; b) K. Krishnankutty, P. Sayudevi, M. B. Ummathur, *J. Indian Chem. Soc.* **84** (2007) 518; c) K. Krishnankutty, P. Sayudevi, M. B. Ummathur, *J. Indian Chem. Soc.* **84** (2007) 337
14. a) M. B. Ummathur, K. Krishnankutty, *Pol. J. Chem.* **82** (2008) 963; b) M. B. Ummathur, K. Krishnankutty, *Chin. J. Chem.* **26** (2008) 453; c) K. Krishnankutty, M. B. Ummathur, *J. Indian Chem. Soc.* **83** (2006) 639; d) K. Krishnankutty, M. B. Ummathur, *J. Indian Chem. Soc.* **83** (2006) 663; e) K. Krishnankutty, M. B. Ummathur, *J. Indian Chem. Soc.* **83** (2006) 883
15. N. Thankarajan, P. Sreeman, *J. Indian Chem. Soc.* **58** (1981) 650
16. K. Nakamoto, *Infrared Spectra and Raman Spectra of Inorganic and Coordination Compounds*, Wiley, New York, 1997
17. L. J. Bellamy, *The Infrared Spectra of Complex Molecules*, Chapman and Hall, London, 1980
18. a) R. L. Lintvedt, H. F. Holtzdaw Jr., *J. Am. Chem. Soc.* **88** (1966) 2713; b) P. J. Roughley, D. A. Whiting, *J. Chem. Soc. Perkin Trans. 1* (1973) 2379
19. C. G. MacDonald, J. S. Shannon, *Aust. J. Chem.* **19** (1966) 1545
20. K. C. Joshi, V. N. Pathak, *Coord. Chem. Rev.* **22** (1977) 37.

Journal of the Serbian Chemical Society
JSCS@tmf.bg.ac.rs • www.shd.org.rs/JSCS

J. Serb. Chem. Soc. 74 (3) 269–277 (2009)
JSCS–3829

UDC 541.121:546.472'723+
+547.82'314.2:547.461.2/.3
Original scientific paper

Acid–base equilibria of the Zn(II) and Fe(III) complexes with condensation products of 2-acetylpyridine and the dihydrazide of oxalic and malonic acid

BRANKA DRAŽIĆ[1], GORDANA POPOVIĆ[1]*, RATOMIR JELIĆ[2], DUŠAN SLADIĆ[3#], DRAGANA MITIĆ[3#], KATARINA ANĐELKOVIĆ[3#] and ŽIVOSLAV TEŠIĆ[3#]

[1]*Faculty of Pharmacy, University of Belgrade, Vojvode Stepe 450, P.O. Box 146, 11000 Belgrade,* [2]*Faculty of Science, University of Kragujevac, Radoja Domanovića 12, 34000 Kragujevac and* [3]*Faculty of Chemistry, University of Belgrade, Studentski trg 12–16, P.O. Box 158,11000 Belgrade, Serbia*

(Received 22 May, revised 4 November 2008)

Abstract: Acid–base equilibria of Zn(II) and Fe(III) complexes with *N'*,*N'*[2]-bis-[(1*E*)-1-(2-pyridyl)ethylidene]ethanedihydrazide (ligand **L1**) and *N'*,*N'*[2]-bis[(1*E*)--1-(2-pyridyl)ethylidene]propanedihydrazide (ligand **L2**), *i.e.*, [Fe(**L1**)$Cl_2(H_2O)$], $[Fe(\mathbf{L2})Cl(H_2O)]^{2+}$, $[Zn(\mathbf{L1})(H_2O)_3]^{+}$ and $[Zn(\mathbf{L2})(H_2O)_2]^{2+}$, which expressed cytotoxic activity, were investigated in aqueous media. The equilibrium constants were determined potentiometrically at 25 °C at a constant ionic strength of 0.10 mol/dm^3 (Na_2SO_4). The results showed that at pH < 8 both the Fe(III) complexes studied here have three, while $[Zn(\mathbf{L1})(H_2O)_3]^{+}$ and $[Zn(\mathbf{L2})(H_2O)_2]^{2+}$ have one and two titratable protons, respectively. Based on the obtained values for the equilibrium constants, protonation schemes of the examined complexes are proposed.

Keywords: metal complexes; d-metals; hydrazone; acid–base equilibria; potentiometry.

INTRODUCTION

Our studies have been directed for several years toward the synthesis, characterization and examination of the biological activity of *d*-metal complexes containing condensation products of 2-acetylpyridine and different hydrazides and hydrazines as ligands.[1–5] Within the scope of these studies, Zn(II) and Fe(III) complexes with condensation derivatives of 2-acetylpyridine and the dihydrazide of either oxalic or malonic acid were synthesized.[5] Among all the examined series of complexes, it was shown that the Zn(II) and Fe(III) complexes expressed the highest cytotoxic activity on HeLa and B16 cell cultures *in vitro*.[6]

* Corresponding author. E-mail: gpopovic@pharmacy.bg.ac.rs
# Serbian Chemical Society member.
doi: 10.2298/JSC0903269D

Acid dissociation constants are particularly important in pharmaceutical research, especially for the discovery and evaluation of new compounds that could be pharmacologically active, *i.e.*, that represent potential drugs. Knowledge on the distribution of the equilibrium forms of a new compound as a function of pH can be of value in the estimation of a the absorption, distribution, metabolism and excretion of a drug, because different equilibrium forms will evolve on its contact with body fluids, disregarding the route of its application. This prompted us to study acid–base equilibria of Zn(II) and Fe(III) complexes with *N′*,*N′*^{2}-bis-[(1*E*)-1-(2-pyridyl)ethylidene]ethanedihydrazide and *N′*,*N′*^{2}-bis-[(1*E*)-1-(2-pyridyl)ethylidene]propanedihydrazide in aqueous media. The chemical structures of the investigated complexes are shown in Fig. 1.

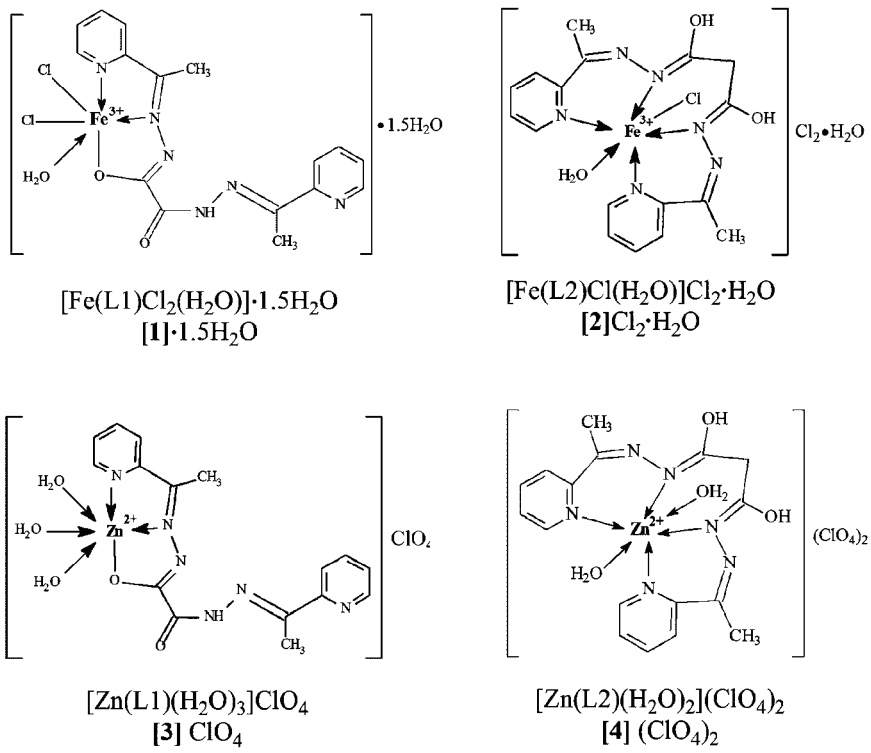

Fig. 1. Chemical structure of the examined Zn(II) and Fe(III) complexes.

EXPERIMENTAL

Apparatus and reagents

UV–Vis spectra were recorded using a GBC UV–visible Cintra 6 spectrophotometer.

For potentiometric titrations, a TTT60 titrator, with an automatic 2.5 cm^3 ABU12 burette with an accuracy of 0.001 cm^3 (Radiometer, Copenhagen, Denmark), was used. The titration mixtures were stirred with a mechanical M22 stirrer (Radiometer) at a constant temperature of

25±0.1 °C. pH-Metric measurements were performed using a PHM240 pH-meter and a combined GK240B electrode (Radiometer). The measured pH values were transformed into p*c*H values (pcH = – log[H_3O^+]) applying the relation:[7]

$$pcH = pH - A \quad (1)$$

The correction factor, A = 0.55±0.01, was determined based on the data of the potentiometric titration of HCl solution (0.007672–0.009424 mol/dm^3) with standard NaOH solution, at 25 °C and constant ionic strength of 0.10 mol/dm^3 Na_2SO_4.

The syntheses and characterization of the Zn(II) and Fe(III) complexes with *N'*,*N'*^{2}-bis-[(1*E*)-1-(2-pyridyl)ethylidene]ethanedihydrazide (ligand **L1**) and *N'*,*N'*^{2}-bis-[(1*E*)-1-(2-pyridyl)ethylidene]propanedihydrazide (ligand **L2**) were described previously.[5] The complexes, prepared by direct and template synthesis and characterized by elemental analysis, ^{1}H-NMR and ^{13}C-NMR spectroscopy, and X-ray analysis,[5] were kept in a cold, dry and dark place. During the experiments described herein, only freshly prepared solutions of the above complexes in deionized water were used. All other reagents were of analytical grade purity (Merck, Darmstadt, Germany). Hydrochloric acid and sodium hydroxide solutions were potentiometrically standardized.

Reversibility of acid–base processes

Three 5.0×10^{-5} mol/dm^3 solutions of each of the examined metal complex were prepared in 0.10 mol/dm^3 Na_2SO_4: solution A, pH 3.3–3.5 (precisely measured), adjusted by adding H_2SO_4; solution B, pH 7.0–8.0, adjusted with NaOH, and solution C, prepared by acidifying solution B with H_2SO_4 to the pH values of solution A.

The spectra of the above solutions were recorded within the wavelength range from 200––500 nm, using a 0.10 mol/dm^3 Na_2SO_4 solution as the blank.

Determination of the equilibrium constants

Equilibrium constants of the examined complexes were determined potentiometrically in aqueous solutions at 25 °C and constant ionic strength of 0.10 mol/dm^3 Na_2SO_4. Solutions of the complexes (25 cm^3; c = 7.3×10^{-4} mol/dm^3) were titrated with 0.020 cm^3 aliquots of a standard carbonate-free NaOH solution (c = 0.0992–0.1052 mol/dm^3). The titrations were performed immediately after the solutions were prepared and after 1, 3, 5 and 7 h.

The equilibrium constants of the complexes were evaluated using the data obtained in three independent titrations. The experimental data were analyzed using the HYPERQUAD computer program.[8]

RESULTS AND DISCUSSION

The acid–base equilibria of the metal complexes **1**–**4** were examined in aqueous medium within the pH range 3.0 to 8.0. The reversibility of these processes was confirmed spectrophotometrically for each complex on the basis of the absorption spectra of their solutions in acidic media (pH 3.52, 3.44, 3.34 and 3.52 for the complexes **1**, **2**, **3** and **4**, respectively), then at pH 7.0–8.0 (pH 7.03, 7.00, 7.71 and 7.10 for the complexes **1**, **2**, **3** and **4**, respectively) and the spectra of the solutions obtained by acidifying the neutral solutions to the desired pH value within acidic pH range. Reversible changes of the spectra during the change of acidity of all four examined complexes were registered, *i.e.*, an overlapping of the spectrum of a complex prepared in an acidic medium with its spectrum after

the change of the pH of its solution from neutral to acidic apparently results from the acid–base equilibrium. The absorption spectra of complex **2** are shown in Fig. 2 as a representative example.

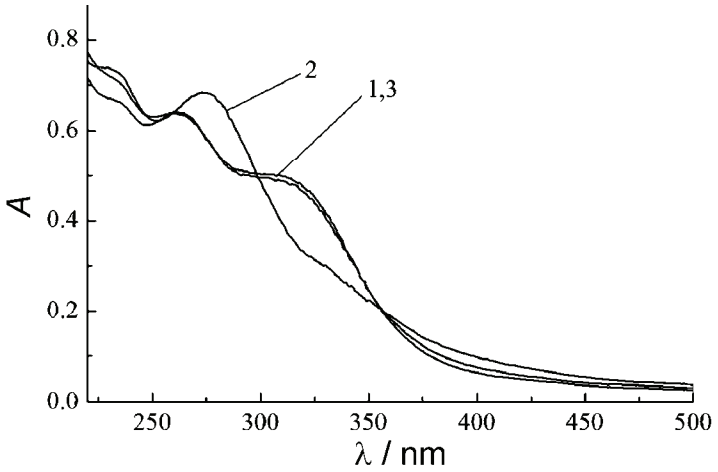

Fig. 2. Absorption spectra of complex **2** in solutions of different pH. 1) pH 3.44; 2) pH 7.00; 3) pH 3.44 (solutions were prepared by acidifying the solution of pH 7.00). c (complex) = 5.0×10^{-5} mol/dm^3.

In Fig. 2, curve 1 represent the spectrum of the solution prepared by dissolving complex **2** in 0.10 mol/dm^3 Na_2SO_4, the pH of the resulting solution being 3.44. Changing the pH of this solution to 7.00 (curve 2) led to a change in the absorption spectrum and a peak at 274 nm appeared. Curve 3 represents the spectrum of complex **2** after changing the pH from 7.00 back to the starting value of 3.44. As seen, curves 1 and 3 overlap each other.

The number of titratable protons in aqueous solutions of the examined complexes was determined on the basis of the moles of NaOH consumed per mole of the complex during potentiometric titration.[9]

From the corresponding titration curves presented in Fig. 3, it can be concluded that within the pH range from 3.0–8.0, the examined complexes contain a single (complex **3**), two (complex **4**) or three (complexes **1** and **2**) acidic groups. The equilibrium constants ($\log \beta_{pqr} = c(M_pL_qH_r)/c(M)^pc(L)^qc(H)^r$) were calculated based on the data of the potentiometric titrations, assisted by the HYPERQUAD computer program (Table I).

The results of the pH-metric titrations up to pH 8.0 were used for the calculation of the constants. Acid–base processes of the complexes in alkaline media were not examined because of their decreased solubility and precipitation.

The protolytic equilibria of the examined complexes, presented in Figs. 4–7, are proposed. The three constants obtained for complex **2** (Fig. 5) point to the substitution of the chloro ligand with a water molecule, as well as to the titration

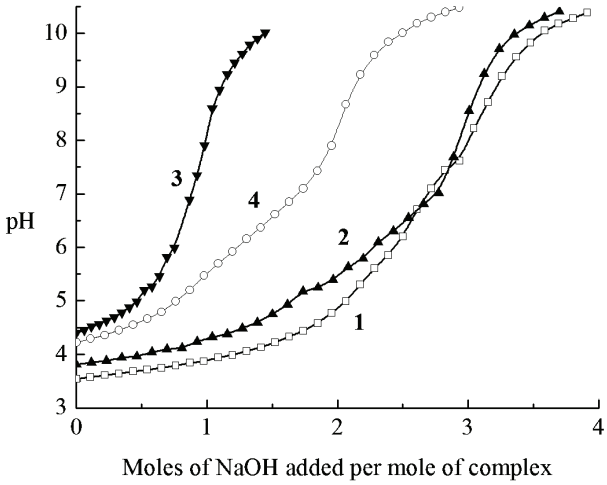

Fig. 3. Potentiometric titration curves of solutions of the Fe(III) and Zn(II) complexes with a standard NaOH solution. The numbers designate the numbers of the complexes.

TABLE I. Stability constants (log β_{pqr}) and the dissociation constants (pK) of the Fe(III) and Zn(II) complexes at t = 25 °C and I = 0.10 mol/dm^3 Na_2SO_4. Values in parentheses refer to the estimated standard deviations

log β_{pqr}	Complex			
	1	**2**	**3**	**4**
log β_{111}	–2.54(12)	–3.01(4)	–4.44(1)	–3.88(2)
log β_{112}	–5.56(8)	–6.87(2)	–	–9.76(4)
log β_{113}	–11.09(9)	–12.72(3)	–	–
pK_1	2.54	3.01	4.44	3.88
pK_2	3.02	3.86	–	5.88
pK_3	5.53	5.85	–	–

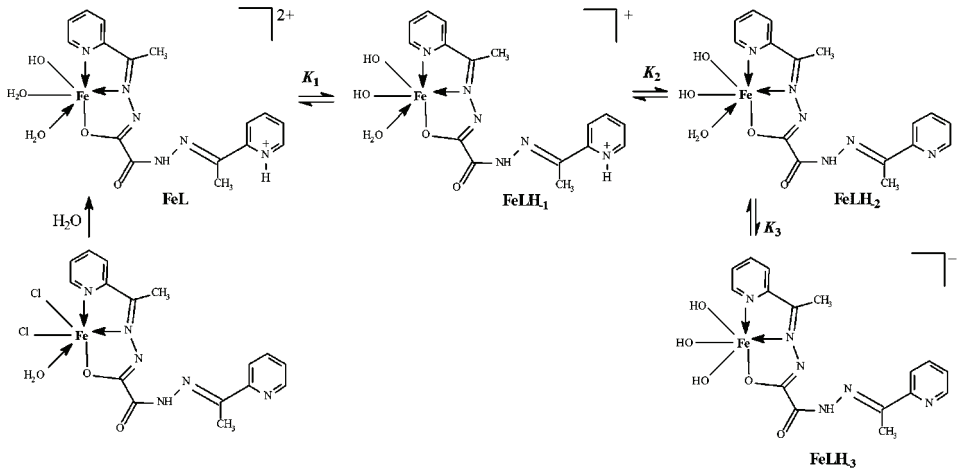

Fig. 4. Protonation scheme of complex **1**.

of protons from both coordinated water molecules and the third proton from ligand **L2** (–N(OH)–N=). The constant pK_1 = 3.01 corresponds to one coordinated water molecule and the other two constants pK_2 = 3.86 and pK_3 = 5.85 could be ascribed to the hydroxylimino group of ligand **L2** and the second coordinated water molecule, respectively. This conclusion was drawn based of a comparison of the constants for complex **2** with those of the Zn(II) complex containing the same ligand (complex **4**) (Fig. 7). Namely, taking into consideration the higher charge of Fe(III) in relation to Zn(II), lower p*K* values of the analogous groups in complex **2** would be expected. The constants pK_1 = 3.88 and pK_2 = 5.88 for complex **4** would belong to one coordinated water molecule and the hydroxylimino group of ligand **L2**, respectively. The three constants of the Fe(III) complex **1** (Fig. 4) demonstrate the substitution of two chloro ligands with water molecules, as well as the involvement of all three water molecules in the acid–base equilibria (ligand **L1** contains no acidic groups). However, since ligand **L1** also contains one pyridine nitrogen atom that represents a non-coordinated basic center, it could be hypothesized that it also participates in these equilibria. Based on the pyridine p*K* of 5.2, it could be supposed that a proton from one coordinated water molecule is transferred to the pyridine nitrogen atom and that the obtained three acidity constants belong to coordinated water molecules (pK_1 = 2.54 and pK_3 = 5.53) and the protonated pyridine nitrogen atom (pK_2 = 3.02). The increased acidity of the protonated pyridine of ligand **L1** in the complex in relation to pyridine itself was to be expected due to a decreased electron density at nitrogen atom resulting from electron-attractive effect of the *ortho* substituent, as well as from the influence of Fe(III) through the system of conjugated bonds. Since only one constant

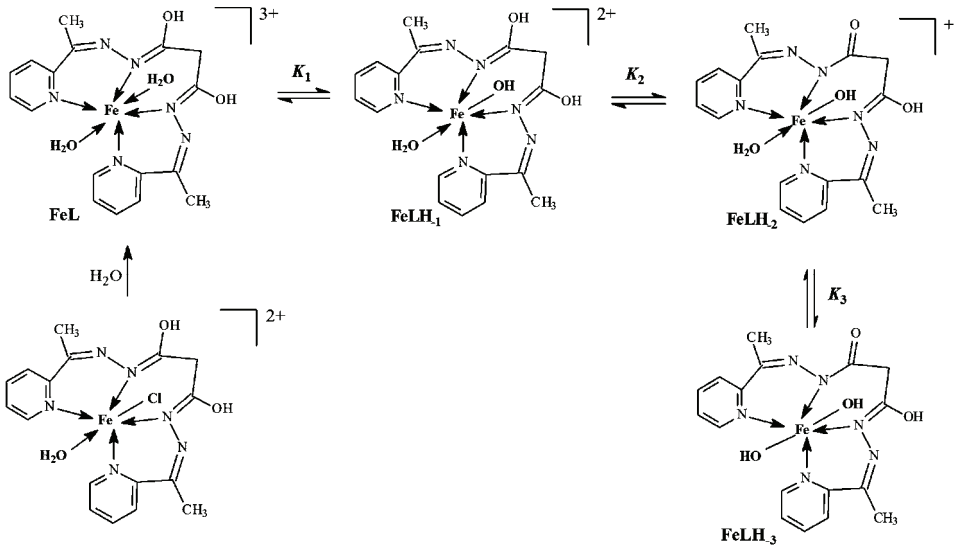

Fig. 5. Protonation scheme of complex **2**.

was determined for complex **3** (pK_1 = 4.44) (Fig. 6), it was assumed that proton transfer from one molecule of coordinated water to the pyridine nitrogen atom in ligand **L1** occurs and due to the lower electron-attractive effect of Zn(II) as compared to that of Fe(III), the obtained value was higher in relation to the analogous Fe(III) complex (complex **1**) (Fig. 4).

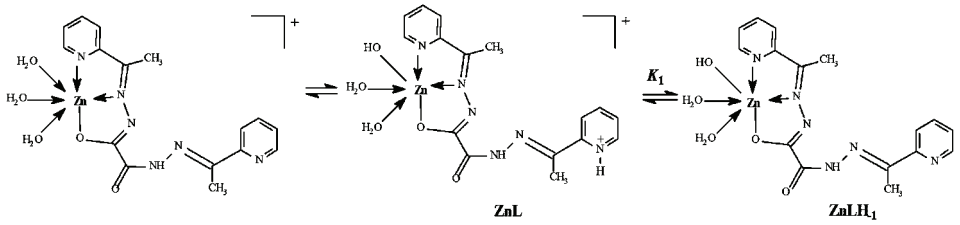

Fig. 6. Protonation scheme of complex **3**.

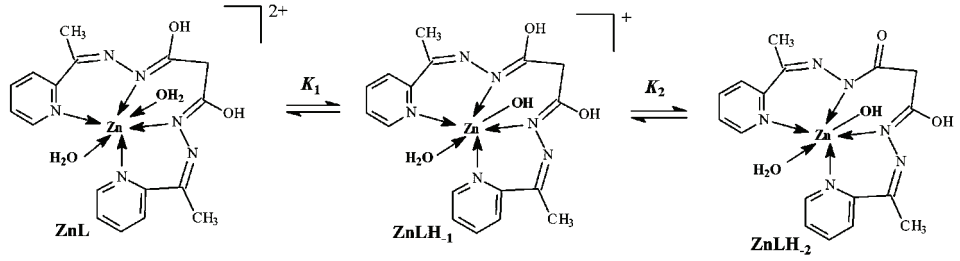

Fig. 7. Protonation scheme of complex **4**.

Based on the determined constants, it was possible to calculate equilibrium concentrations of each particle present in solution at a defined pH value. Representative distribution of the equilibrium species of the complex **1** as a function of pH is depicted in Fig. 8.

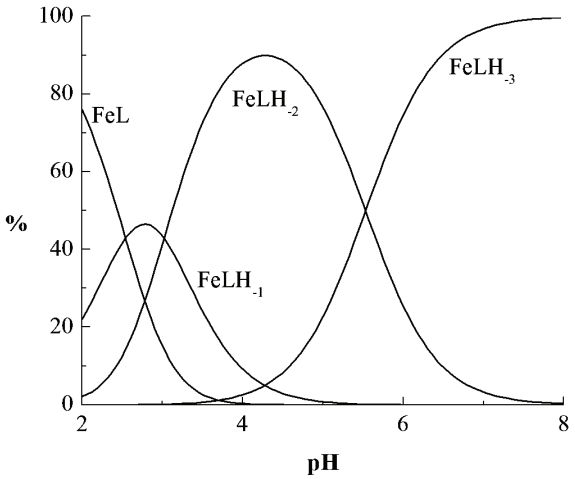

Fig. 8. Distribution of the equilibrium species of complex **1** as a function of pH.

From Fig. 8, it can be seen that at pH < 4.00, three forms of complex **1** are in equilibrium: the dication $[FeL]^{2+}$, the monocation $[FeLH_{-1}]^{+}$ and the neutral form $[FeLH_{-2}]^{0}$. Within the pH range 4.00 to 7.00, the neutral form and monoanion $[FeLH_{-3}]^{-}$ were dominant, while at pH > 7, the solution contained only the monoanion.

The uncharged forms of complexes **2**–**4** were predominant at pH 7.40 (the physiological pH of human body fluids), while complex **1** had a single negative charge. This result is significant for studies on the transport of the examined complexes through cell membranes, which are usually permeable for uncharged moieties, *i.e.*, liposoluble species.

Acknowledgement. This work was supported by the Ministry for Science and Technological Development of Serbia, Contract No. 142062.

И З В О Д

КИСЕЛИНСКО–БАЗНЕ РАВНОТЕЖЕ КОМПЛЕКСА Fe(III) И Zn(II) СА КОНДЕНЗАЦИОНИМ ДЕРИВАТИМА 2-АЦЕТИЛПИРИДИНА И ХИДРАЗИДА ОКСАЛНЕ, ОДНОСНО МАЛОНСКЕ КИСЕЛИНЕ

БРАНКА ДРАЖИЋ[1], ГОРДАНА ПОПОВИЋ[1], РАТОМИР ЈЕЛИЋ[2], ДУШАН СЛАДИЋ[3], ДРАГАНА МИТИЋ[3], КАТАРИНА АНЂЕЛКОВИЋ[3] и ЖИВОСЛАВ ТЕШИЋ[3]

[1]*Фармацеутски факултет, Универзитет у Београду, ул.пр. 146, Војводе Степе 450, 11000 Београд,* [2]*Природно–математички факултет, Универзитет у Крагујевцу, Радоја Домановића 12, 34000 Крагујевац и* [3]*Хемијски факултет, Универзитет у Београду, ул.пр 158, Студентски трг 12–16, 11000 Београд*

У овом раду су проучаване киселинско-базне равнотеже у воденим растворима комплекса Zn(II) i Fe(III) са *N*',*N*'^{2}-бис[(1*E*)-1-(2-пиридил)етилиден]етандихидразидом (лиганд **L1**) и *N*',*N*'^{2}-бис[(1*E*)-1-(2-пиридил)етилиден]пропандихидразидом (лиганд **L2**), тј. $[Fe(\mathbf{L1})Cl_2(H_2O)]$, $[Fe(\mathbf{L2})Cl(H_2O)]^{2+}$, $[Zn(\mathbf{L1})(H_2O)_3]^{+}$, $[Zn(\mathbf{L2})(H_2O)_2]^{2+}$, који показују цитотоксичну активност. Равнотежне константе су одређиване потенциометријски, на температури 25 °C и при константној јонској јачини 0,10 mol/dm^3 Na_2SO_4. Утврђено је да у интервалу pH < 8 испитивани Fe(III) комплекси имају три, $[Zn(\mathbf{L1})(H_2O)_3]^{+}$ један, а $[Zn(\mathbf{L2})(H_2O)_2]^{2+}$ два протона који могу да се титришу. На основу добијених вредности за константе, претпостављене су и одговарајуће протонационе схеме.

(Примљено 22. маја, ревидирано 4. новембра 2008)

REFERENCES

1. K. Andjelković, J. Howing , R. Tellgren, D. Jeremić, I. Ivanović-Burmazović, D. Sladić, *J. Coord. Chem.* **56** (2003) 611
2. K. Andjelković, G. Jakovljević, M. Zlatović, Ž. Tešić, D. Sladić, J. Howing, R. Tellgren, *J. Serb. Chem. Soc.* **69** (2004) 651
3. A. Bacchi, G. Pelizzi, D. Jeremić, D. Sladić, M. Gruden-Pavlović, K. Andjelković, *Transition Met. Chem.* **28** (2003) 935
4. N. Filipović, A. Bacchi, G. Pelizzi, R. Marković, D. Mitić, K. Anđelković, *J. Coord. Chem.* **58** (2005)1541

5. K. Anđelković, D. Sladić, A. Bacchi, G. Pelizzi, N. Filipović, M. Rajković, *Transition Met. Chem.* **30** (2005) 243
6. M. Lazić, S. Radulović, T. Todorović, D. Sladić, Ž. Tešić, K. Andjelković, *Mater. Sci. Forum* **518** (2006) 513
7. H. M. N. H. Irving, M. G. Miles, L. D. Pettit, *Anal. Chim. Acta* **38** (1967) 475
8. P. Gans, A. Sabatini, A. Vacca, *J. Chem. Soc., Dalton Trans.* (1985) 1195
9. R. Prakash, G. Ramachandraiah, *J. Chem. Soc., Dalton Trans. 1* (2000) 85.

Journal of the Serbian Chemical Society
JSCS@tmf.bg.ac.rs • www.shd.org.rs/JSCS

J. Serb. Chem. Soc. 74 (3) 279–289 (2009)
JSCS–3830

UDC 546.57+544.654.2:548.19
Original scientific paper

Effect of non-stationary current regimes on the morphology of silver electrodeposits

ALEKSANDAR T. DIMITROV[1]*, PERICA PAUNOVIĆ[1], ORCE POPOVSKI[2], DRAGAN SLAVKOV[1], ŽELJKO KAMBEROVIĆ[3] and SVETOMIR HADŽI JORDANOV[1]

[1]*Faculty of Technology and Metallurgy, University "St. Cyril and Methodius", Skopje,* [2]*Military Academy "Mihajlo Apostolski", Skopje, FYR Macedonia and* [3]*Faculty of Technology and Metallurgy, University in Belgrade, Serbia*

(Received 19 September, revised 30 October 2008)

Abstract: This work is concerned with the use of reverse current regimes in order to form small-grained and compact silver deposits during the electrorefining process. Several parameters were varied, *i.e.*, *i*) anodic overpotential, *ii*) cathodic *vs.* anodic time ratio and *iii*) duration of the anodic pulse. After optimization of these parameters, phosphate ions were added and the electrolyte was stirred. The effects of a rise of the anodic overpotential on the grain sizes of the silver deposit and compactness were studied. Prolongation of the anodic time had a similar influence but with a decrease in current efficiency. An increase of the cathodic *vs.* anodic time ratio caused an enlargement of the grains and a decrease in the compactness of the deposit. Optimal morphological characteristics were obtained when PO_4^{3-} were added and the electrolyte was stirred.

Keywords: silver; reverse current; electrorefining; nitrate solution; electrodeposition.

INTRODUCTION

Morphology, which depends on kinetic parameters of the electrodeposition process, overpotential and current density, is considered to be one of the most important features of electrodeposited metals. Traditionally, silver produced by electrorefining from nitrate electrolytes is of dispersed shape (mostly dendritic and spongy).[1] Compact and technically applicable metals are produced by a further smelting/casting procedure.[2]

In order to explain why silver deposits are preferentially dendritic, both electrochemical and crystallographic aspects were considered. Granular deposits of high porosity at lower overpotentials and dendrites at higher ones are the result of the high value of the silver exchange current density (low j/j_0 ratio).[3] On the

* Corresponding author. E-mail: aco@tmf.ukim.edu.mk
doi: 10.2298/JSC0903279D

other hand, non-compact silver layers are formed due to hindered nucleation. Markov *et al.*[4] showed the existence of a wide nucleation exclusion zone near each nucleus growing on a foreign substrate, and Milchev[5] the same in the case of silver. The generation and growth of nuclei is followed by the formation and growth of the nucleation exclusion zones. As a result, the nucleus surface density is low and hence rough and uneven deposits are formed during further growth.

Normally, direct formation of compact silver deposits is preferable. This leads to a simpler and cheaper electrorefining process as well as a higher level of purification. In previous papers,[5–7] it was shown that the addition of small quantities of phosphate ions, PO_4^{3-}, and stirring of the nitrate electrolyte, created conditions favorable for compact and small-grained silver deposits. This is probably leads to a maximum of the steady-state electrolysis conditions.

Another approach to improve the morphology of silver deposits is the application of reverse current regimes, which results in the dissolution of dendrites and a smoothing of the deposit during the anode pulse at the working electrode,[6] and a decrease of the size of the nucleation exclusion zone;[7] hence, compacter silver deposits are to be expected.

The main goal of this work was to examine how the reverse current regimes affect the morphology of silver deposits. This involved the selection of the appropriate cathodic and anodic overpotential, cathodic *vs.* anodic time ratio and the duration of the anodic pulse. Simultaneously, the effect of stirring and the addition of phosphate ions were also studied.

EXPERIMENTAL

In order to determine the reference state, silver was deposited by direct current electrolysis at –80 mV, as explained elsewhere.[8] The investigation continued with reverse current electrolysis, with variation of several parameters, *i.e.*, *i*) the anodic overpotential η_a was varied between 40–160 mV, *ii*) the cathodic *vs.* anodic pulse duration $\tau_c:\tau_a$, was 8:1, 4:1 and 2:1 and *iii*) the duration of the anodic pulse τ_a (2 and 4 s). All variations were investigated both with and without stirring of the electrolyte and/or addition of PO_4^{3-}.

Electrodeposition was performed in an electrochemical cell consisting of Ag wires (0.5 mm) for both the working and reference electrode and an Ag plate with a much higher surface area as the counter electrode. The electrolyte contained 0.50 M $AgNO_3$ and 1.17 M $NaNO_3$, with a further 0.060 M H_3PO_4 added when required. All chemicals were of p.a. quality, and redistilled and deionized water was used. Both stationary and stirred electrolytes (magnetic stirrer, 400 rpm) were tested. The electrochemical cell was connected with an AMEL electrochemical line (Potentiostat/Galvanostat 2053 and programmable generator 568) and a gas-purification line. All experiments were performed at room temperature.

The obtained silver deposits were examined and documented by a scanning electron microscope (SEM), Hitachi 2000 Delta instrument.

RESULTS AND DISCUSSION

Reverse vs. *steady-state electrodeposition*

In the preliminary stage, the experiments were aimed at demonstrating the differences between the silver deposits produced by d.c. and those by obtained by reverse current electrodeposition at the same cathodic overpotential. The anodic overpotential in the case of the reverse electrodeposition was randomly chosen and further optimized. Determination of the optimal anodic overpotential will be discussed in the following section. A comparison of the morphology is given in Fig. 1. It is obvious that, in both cases, the crystals possessed an FCC-type lattice. The grains were a combination of cube–octahedron, *i.e.*, cubic crystals with modified corners (see Fig. 2). During the steady-state electrodeposition, some other morphological forms developed as well, *e.g.*, twinned grains (A in Fig. 1) and spiral-like crystals (B in Fig. 1). At the edge of the electrode, dendritic growth started (C in Fig. 1). The morphology of the deposit was heterogeneous and non-compact even at the optimal overpotential for d.c. electrodeposition. The opposite, *i.e.*, homogeneity in size and shape, was produced when current reversal was applied (Fig. 1c). The crystal grains were cubic with modified corners and smaller than in the previous case.

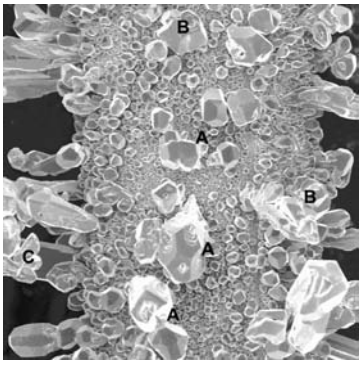

(a)

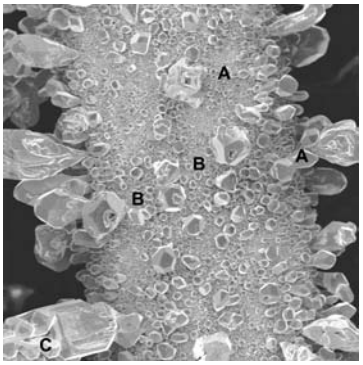

(b)

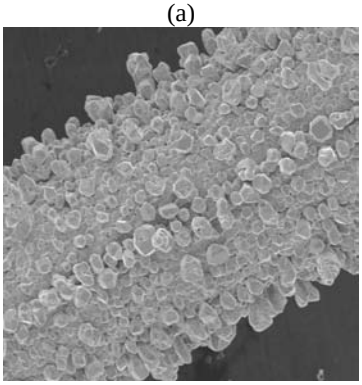

(c)

Fig. 1. Silver electrodeposits produced in 0.50 M HNO_3 + 1.17 M $NaNO_3$: a) steady-state electrodeposition at η_c = –70 mV, $\tau_{deposition}$ = = 10 min, b) the same as in a at η_c = –80 mV, c) reverse electrodeposition η_c = –80 mV, η_a = 80 mV, τ_c:τ_a = 2:1, τ_a = 2 ms, $\tau_{deposition}$ = = 10 min; magnification: ×100.

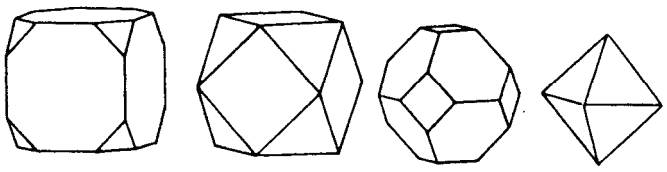

Fig. 2. Transitional shapes from cubic to octahedral: a) initial stage of the modification of the cubic corners, b) and c) different variants of cubic-octahedra, d) octahedral.

During steady-state electrodeposition, the number of nuclei increases, reaching saturation after a certain time (10–100 ms), after which there is no further nuclei formation and only crystal growth occurs. The number of nuclei in the stationary state depends only on the applied overpotential/current density. In the case of the reverse electrodeposition regime, due to the short time of the cathodic pulse, there is no saturation of nuclei formation. After any cathodic pulse, the number of nuclei increases and this contributes to the formation of smaller grains than in the case of steady-state deposition. It should also be mentioned that dissolution of the surface layer occurs during the anodic pulse. This layer contains larger grains and other morphological forms, especially dendrites. As a result of dissolution, a layer with uniform size and shape of grains is formed. The cycle of alternating deposition/dissolution contributes to formation of homogeneous, small-grained and compact deposits.

Variation of η_a *and* τ_c:τ_a

The first step in the optimization of the parameters of reverse current electrodeposition was an investigation of the influence of the anodic overpotential η_a and the ratio of duration of cathodic *vs*. anodic pulse τ_c:τ_a.

In a previous study,[8] a value of cathodic overpotential of –80 mV was found to be the most suitable, providing the best balance between nucleation and the crystal growth process. Thus, this value was adopted as the value for the cathodic overpotential of the reverse electrodeposition. During the cathodic pulse, deposition of silver occurs as in the case of steady-state electrodeposition but, due to the short duration (shorter than 10 ms), saturation of the nucleation process is not achieved, *i.e.*, the same quantity of metal is dispersed over a larger number of nuclei and, consequently, a small-grained deposit is produced.

On the other hand, during the anodic pulse, several processes occur, such as: *i*) dissolution of all crystals, preferentially at places where the exchange current density j_0 is the highest and *ii*) the splitting off of the crystals weakly bound onto the substrate, especially of larger crystals and dendrites.

The sites of the removed crystals or dendrites are suitable for nucleation in the next cathodic pulse because the nucleation exclusive zones have decreased or completely disappeared. Moreover, they could be also suitable for the growth of neighboring crystals.

The anodic overpotential, η_a, was varied over a wider range of overpotentials, *i.e.*, 40–160 mV. The duration of the anodic pulse τ_a of the reverse cycle is usually shorter than that of the cathodic one τ_c, and in this case it was 2 ms. The ratio of cathodic *vs.* anodic pulse period $\tau_c:\tau_a$ was varied as 8:1, 4:1 and 2:1, meaning that τ_c was 16, 8 and 4 ms, respectively.

The change in the morphology of the silver deposits as a function of the variation of the anodic overpotential, η_a, and $\tau_c:\tau_a$ is shown in Fig. 3. At lower

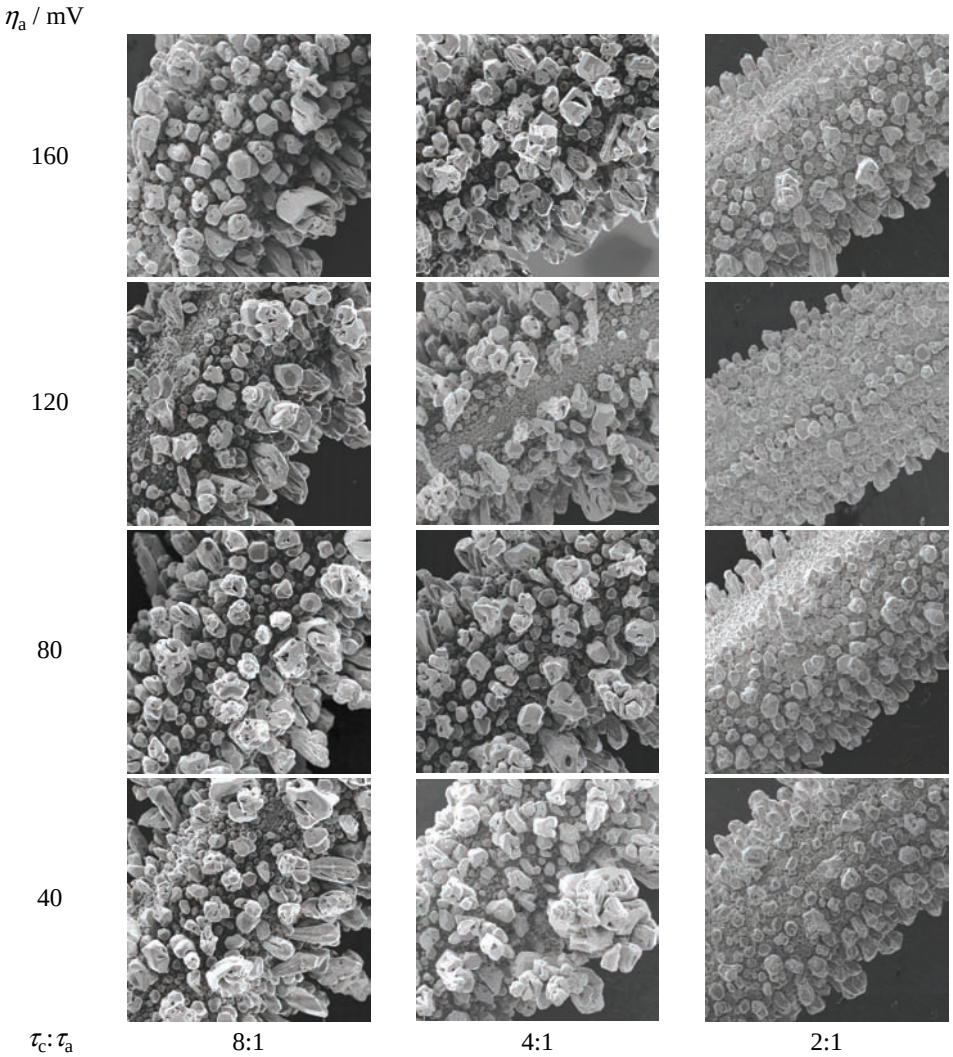

Fig. 3. Morphological changes of silver electrodeposits as a function of the anodic overpotential, η_a, and cathodic *vs.* anodic time ratio, $\tau_c:\tau_a$; τ_a = 2 ms, $\tau_{deposition}$ = 10 min; magnification: ×100.

anodic overpotential (40 and 60 mV), there was no splitting off or release of the crystals, only a slow dissolution. At higher anodic overpotentials, the tips of the crystals dissolved faster than the side parts. According to their size and shape, it seems that they grew uniformly in all directions. Nevertheless, there was not mutual linking of the crystals. An increase of the anodic overpotential also caused a more intensive dissolution of the larger crystals as well as their splitting and entire release, especially of dendrites. Hence, at an anodic overpotential of 120 mV, the deposits consisted of smaller grains and were more compact than the corresponding ones obtained at lower overpotentials. On further increasing of the anodic overpotential to 160 mV, the grain size and compactness continued to improve. However, considering the lower current efficiency at 160 mV, an anodic overpotential of 120 mV could be regarded as the optimal one.

At the beginning of a cathodic pulse, the nucleation density was high enough for the number of grains to increase and their linkage to occur. It could have been expected that small-grained and compact deposits would continue to improve with further adjustment. However, at the higher ratio of cathodic *vs*. anodic overpotential $\tau_c:\tau_a$, saturation of the nucleation could be achieved and crystals grew larger. Even at $\tau_c:\tau_a$ = 2:1, the obtained deposit was small-grained and compact, but the current efficiency was lower.

Thus, further optimization of the electrolysis parameters was directed towards obtaining small-grained compact deposits with higher current efficiency, *i.e*., at a higher $\tau_c:\tau_a$ ratio, *e.g.* 4:1. In order to realize this, the anodic pulse period was varied.

Variation of the anodic pulse period, τ_a

An SEM image of an electrodeposit obtained by reverse electrodeposition with increased duration of the anodic pulse, τ_a = 4 ms, is shown in Fig. 4. Compared with the corresponding deposit obtained under identical conditions but with τ_a = 2 ms (see Fig. 1c), this deposit shows a denser nucleation and close--packed grains of reduced size. Prolongation of the anodic pulse enabled a more intensive dissolution of the larger crystals as well as the release of weaker bound

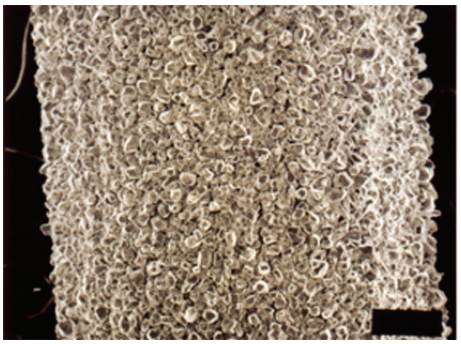

Fig. 4. Silver deposit produced in 0.50 M HNO_3 + 1.17 M $NaNO_3$; η_c = –80 mV; η_a = = 80 mV; $\tau_c:\tau_a$ = 2:1; τ_a = 4 ms; $\tau_{deposition}$ = = 10 min; magnification: ×100.

crystals from the electrode surface, especially dendrites. Successively repeating the cathodic and anodic pulses resulted in the formation of smaller-grained and more compact deposit. However, the compactness can also be improved with further changes of the electrodeposition conditions, for instance, the addition of PO_4^{3-} and application of stirring to the electrolyte.

Simultaneous action of PO_4^{3-} and stirring of the electrolyte

As mentioned above, formation of compact deposit depends on the j/j_0 ratio. The higher the j/j_0 ratio, the better is the compactness of the deposit. There are several approaches to increase the value of j/j_0, either through increasing the current density, or decreasing the exchange current density, j_0. Further attempts in this study to improve the morphological characteristics of the silver deposits were to include PO_4^{3-} and to stir the electrolyte.

The presence of PO_4^{3-} affects both an increase in the number of active centers and the stimulation of 2D crystal growth. This is a result of lower exchange current density. The values of the exchange current density in nitrate solution with and without PO_4^{3-}, measured by impedance spectroscopy, were 5.0 and 26 mA cm^{-2}, respectively.[6] The polarization curves of the electrodeposition of silver from a solution with and without PO_4^{3-} are shown in Fig. 5. At the potential interval of the formation of polycrystalline deposits, near –80 mV, the current densities were almost the same. Hence, the j/j_0 ratio was more than 5 times higher in the presence of PO_4^{3-} than in their absence. In this case, the nucleation rate increases considerably, while the radius of the nucleation exclusion zones decrease. The large difference in the j_0 values can be attributed to the formation of adsorbed intermediate complexes of Ag^+ and PO_4^{3-}, according to the following mechanism:[6,8]

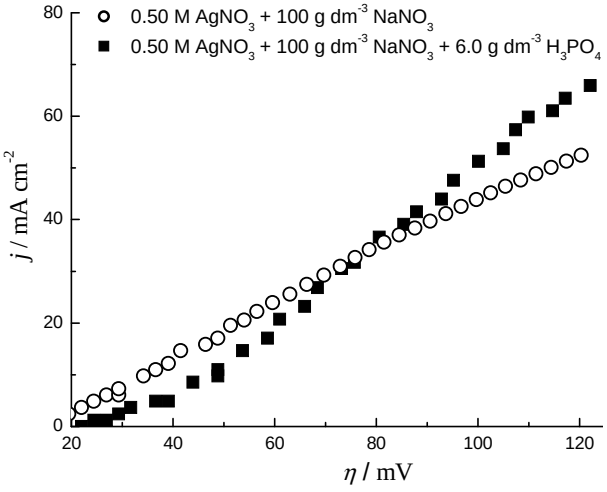

Fig. 5. Polarization curves for a silver electrode in electrolytes with and without PO_4^{3-}.

$$Ag^{+} + PO_4^{3-} \rightarrow (Ag\,PO_4^{2-})_{ads}$$

$$(Ag\,PO_4^{2-})_{ads} + e^{-} \rightarrow Ag + (PO_4^{3-})_{ads}$$

Electrocrystallization processes controlled by incorporation of adatoms suggest two-dimensional (2D) growth. As can be seen from Fig. 6a and 6b, the formed grains had a plate-like shape. As PO_4^{3-} favor the generation of a larger numbers of nuclei and almost eliminate nucleation exclusive zones, the produced deposit was more compact than in the previous cases. Furthermore, if electrolyte stirring is applied, the processes intensify and the deposits were even more compact with smaller grains (Fig. 6c and 6d). The plates were very closely packed and mutually intertwined, thus whisker-like shapes can be observed.

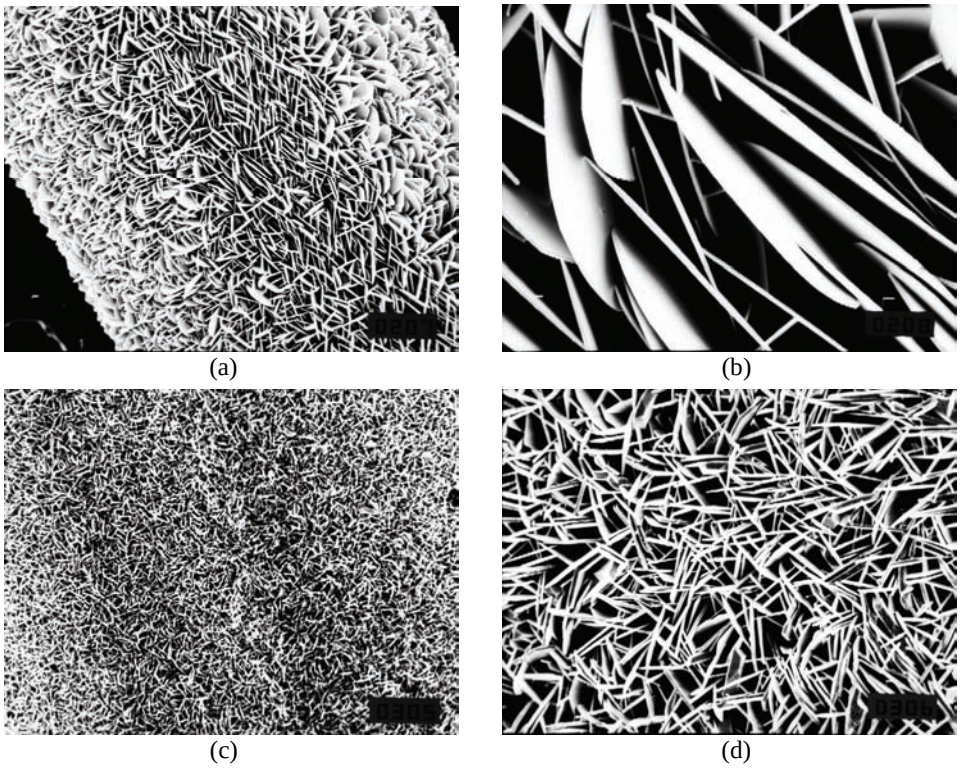

(a) (b) (c) (d)

Fig. 6. Silver electrodeposits produced by reverse electrodeposition in 0.50 M HNO_3 + 1.17 M $NaNO_3$ + 0.060 M PO_4^{3-} at η_c = –80 mV, η_a = 120 mV, τ_c:τ_a = 4:1, τ_a = 4 ms, $\tau_{deposition}$ = 10 min; a) no stirring, magnification: ×100, b) the same as in a), magnification: ×1000, c) stirring 400 rpm, magnification: ×100, d) the same as in c), magnification: ×1000.

Changing the hydrodynamic regime is another approach to increase the j/j_0 ratio. Stirring the electrolyte also lowers diffusion limitations during electrocrystallization. It lowers the concentration gradient that provides a continuous supply

of Ag^+ to the cathode surface. The thickness of the diffusion layer, δ, is also smaller, which means the limiting current density increases. This contributes to an increase in the j/j_0 ratio.

In the case of the simultaneous addition of PO_4^{3-} and stirring of the electrolyte, the j/j_0 ratio increases as a result of both an increase in j due to the stirring of the electrolyte and decrease of j_0 due to introduction of PO_4^{3-}. This enables the formation of compact and small-grained deposits even under conditions when previously this was impossible possible. Figure 7 shows that a fine compact deposit can be obtained at the lower anodic overpotential, 80 mV, and the higher ratio of the duration of the cathodic *vs*. anodic pulse, $\tau_c:\tau_a$ = 4:1. This contributes to an improved quality of the deposits and the current efficiency of the electrodeposition process.

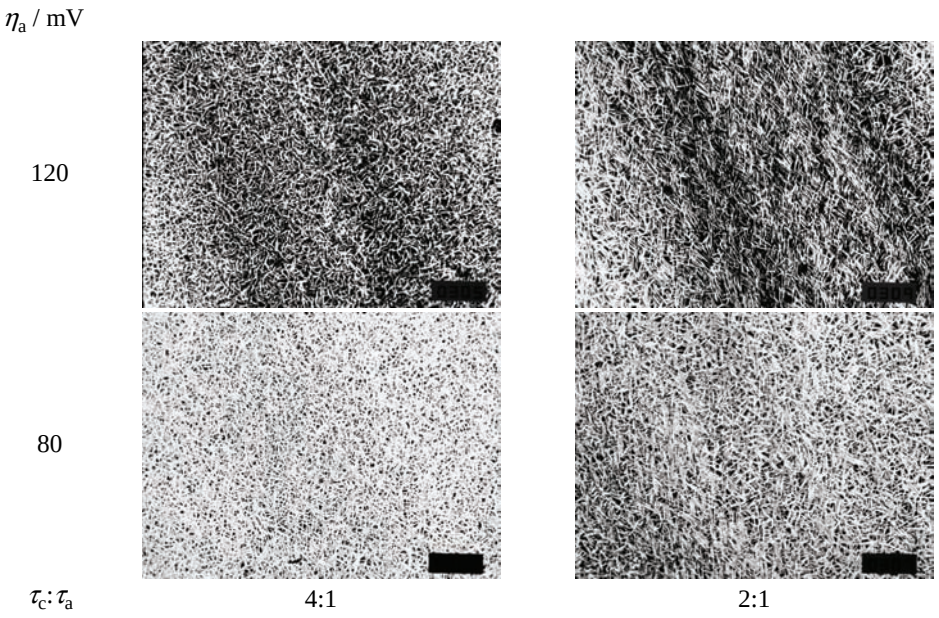

Fig. 7. Morphological changes of silver electrodeposits as a function of anodic overpotential, η_a, and cathodic *vs*. anodic time ratio, $\tau_c:\tau_a$, applying stirring of 400 rpm to the electrolyte; τ_a = 4 ms, $\tau_{deposition}$ = 10 min; magnification: ×100.

CONCLUSIONS

The investigations in this study were motivated by the idea to obtain small--grained and compact silver deposits by electrodeposition under electrorefining conditions. After varying several parameters such as anodic overpotential, anodic pulse period, cathodic *vs*. anodic time ratio in stirred and non-stirred electrolyte both with and without the addition of PO_4^{3-}, the following conclusions can be reached:

1) Increasing the anodic overpotential resulted in the formation of smaller grains and increased the compactness of the deposit. An optimal overpotential could be considered 120 mV, because further increasing the overpotential considerably decreased the current efficiency of the electrodeposition process.

2) Increasing the cathodic *vs*. anodic time ratio, $\tau_c:\tau_a$, led to the formation of a rough deposit with larger grains. At $\tau_c:\tau_a$ = 2:1, the deposit obtained was compact with smaller grains, but in this case the current efficiency was very low.

3) Prolongation of the anodic pulse had a similar influence on the morphology as the anodic potential, *i.e*., it enabled the formation of a more compact and small-grained deposit. In this case, an appropriate morphology can be obtained at higher cathodic *vs*. anodic time ratios.

4) The addition of PO_4^{3-} and stirring the electrolyte enabled the formation of deposits with the best morphological characteristics at a higher current efficiency.

Reverse current regimes in combination with PO_4^{3-} and stirring of the electrolyte during electrorefining are suitable ways of encouraging the formation of refined and compact silver deposits and they are technically applicable.

Acknowledgement. This paper was supported by and performed within the Project "Study of morphology of metal deposits produced by electrorefining under modified conditions" of the Ministry of Education and Science of the Republic of Macedonia.

И З В О Д

ЕФЕКАТ НЕСТАЦИОНАРНИХ СТРУЈНИХ РЕЖИМА НА МОРФОЛОГИЈУ ТАЛОГА СРЕБРА

ALEKSANDAR T. DIMITROV[1], PERICA PAUNOVIĆ[1], ORCE POPOVSKI[2], DRAGAN SLAVKOV[1], ЖЕЉКО КАМБЕРОВИЋ[3] и SVETOMIR HADŽI JORDANOV[1]

[1]*Faculty of Technology and Metallurgy, University "St. Cyril and Methodius", Skopje,* [2]*Military Academy "Mihajlo Apostolski", Skopje, FYROM и* [3]*Технолошко–металуршки факултет, Универзитет у Београду, Београд*

Рад се бави коришћењем реверсних струјних режима за добијање ситнозрних и компактних талога сребра у процесу електрохемијске рафинације. Варирано је неколико параметара: а) анодна пренапетост, б) однос времена трајања катодног и анодног пулса и ц) трајање анодног пулса. Након оптимизације ових параметара, у електролит су додати фосфатни јони и примењено је мешање електролита. Испитиван је утицај анодне пренапетости на величину зрна талога сребра и на његову компактност. Продужење трајања анодног пулса показало је сличан ефекат, али уз смањење искоришћења струје. Повећање односа времена трајања катодног и анодног пулса довело је до повећања зрна и смањења компактности талога. Оптимална морфологија талога је добијена након додатка PO_4^{3-} и уз мешање електролита.

(Примљено 19. септембра, ревидирано 30. октобра 2008)

REFERENCES

1. A. M. Mosher, *Trans. Am. Inst. Mining. Eng.* **106** (1933) 427
2. C. W. Clark, A. A. Heimrod, *Trans. Electrochem. Soc*. **61** (1932) 77
3. H. Gerischer, *Z. Electrochem*. **62** (1958) 256

4. I. Markov, A. Boynov, S. Toshev, *Electrochim. Acta* **18** (1973) 377
5. A. T. Dimitrov, S. Hadži Jordanov, K. I. Popov, M. G. Pavlović, V. Radmilović, *J. Appl. Electrochem.* **28** (1998) 791
6. K. I. Popov, E. R. Stojilković, V. Radmilović, M. G. Pavlović, *Powder Technol.* **93** (1997) 55
7. N. D. Nikolić, E. R. Stojilković, K. I. Popov, M. G. Pavlović, *J. Serb. Chem. Soc.* **63** (1998) 877
8. A. T. Dimitrov, *PhD Thesis*, University "Sts. Cyril and Methodius", Skopje, 1997 (in Macedonian).

Journal of the Serbian Chemical Society
JSCS@tmf.bg.ac.rs • www.shd.org.rs/JSCS
J. Serb. Chem. Soc. *74* (3) 291–299 (2009)
JSCS–3831
UDC 541.132+66.082.2:66.087+66.012
Original scientific paper

The effect of the concentration of the reacting ion on the control of the electrodeposition process

PREDRAG M. ŽIVKOVIĆ[1]*, NEBOJŠA D. NIKOLIĆ[2#], MILICA GVOZDENOVIĆ[1] and KONSTANTIN I. POPOV[1,2#]

[1]*Faculty of Technology and Metallurgy, University of Belgrade, Karnegijeva 4, 11120 Belgrade and* [2]*ICTM – Center for Electrochemistry, University of Belgrade, Njegoševa 12, Belgrade, Serbia*

(Received 11 July, revised 12 November 2008)

Abstract: The effect of the concentration of the reacting ion on the nature of the control of the electrodeposition process was investigated by digital simulation of the polarization curve using the Newman form of the polarization curve equation and the Levich dependence of the limiting diffusion current density under natural convection conditions. A simple method for the determination of the exchange current density from polarization measurements is also proposed. The agreement with experiments was correct.

Keywords: polarization curve equation; concentration dependence.

INTRODUCTION

It was shown recently[1,2] that instead of the general equation of the cathodic polarization curve:

$$\frac{j}{j_L} = \frac{j_0}{j_L}\left(1-\frac{j}{j_L}\right)^{\gamma}\left(f_c - f_a\right) \tag{1}$$

the approximate form:

$$\frac{j}{j_L} = \frac{\frac{j_0}{j_L}\left(f_c - f_a\right)}{1+\frac{j_0}{j_L}\left(f_c - f_a\right)} \tag{2}$$

obtained by taking $\gamma = 1$, can be used with a maximum error of 20 %. Equations (1) and (2) are modified for use in the electrodeposition of metals by taking the

* Corresponding author. E-mail: peca@tmf.bg.ac.rs
# Serbian Chemical Society member.
doi: 10.2298/JSC0903291Z

Popov *et al.*[3] j, j_0 and j_L are the current density, the exchange current density and limiting diffusion current density for the cathodic process, respectively,

$$f_c = 10^{\frac{\eta}{b_c}} \tag{3}$$

and

$$f_a = 10^{-\frac{\eta}{b_a}} \tag{4}$$

and η is the overpotential, b_c and b_a are the cathodic and anodic Tafel slope, respectively, and

$$\gamma = \frac{\mathrm{d}\log j_0}{\mathrm{d}\log c} \tag{5}$$

where c is the concentration of the reacting ion.

It is necessary to note that Eq. (2) is an approximation because the value of γ is lower than unity.[4] This approximation is widely used in qualitative discussions because it permits the simple mathematical treatment of electrochemical processes with relatively small errors. If $\gamma \neq 1$ is included in the derivation of the general equation of the cathodic polarization curve, simple analytical solutions are not available and numerical solutions are required.

It can be seen from Eq. (2) that the ratio j_0/j_L determines the nature of the control of the electrodeposition process. If

$$\frac{j_0}{j_L} \to 0 \tag{6}$$

the metal electrodeposition process is under activation control and if

$$\frac{j_0}{j_L} \to \infty \tag{7}$$

it is under diffusion control. On the other hand, it is known that j_0 and j_L depend on the concentration of the reacting ion. Thus, the aim of this study was to investigate the effect of the concentration of the reacting ion on the control of the electrodeposition process.

THE STATEMENT OF THE PROBLEM

It is known that the concentration dependence of the exchange current density[4] is expressed as:

$$j_{0,c} = \left(\frac{c}{c_0}\right)^{\gamma} j_{0,0} \tag{8}$$

where $j_{0,c}$ and $j_{0,0}$ are the exchange current densities corresponding to the concentrations c and c_0 of the reacting ion.

The limiting diffusion current density j_L depends on the concentration of the reacting ion according to:[5]

$$j_L \approx c^n \tag{9}$$

where

$$1 \leq n \leq 1.25 \tag{10}$$

depending on the hydrodynamic conditions in the electrochemical cell. Assuming c_0 as the concentration of the reacting ion in a reference solution, it follows from Eq. (9) that:

$$j_{L,c} = \left(\frac{c}{c_0}\right)^n j_{L,0} \tag{11}$$

where $j_{L,c}$ and $j_{L,0}$ are the limiting diffusion current densities for the concentrations of the reacting ion c and c_0, respectively, and because of Eqs. (8) and (9):

$$\frac{j_{0,c}}{j_{L,c}} = \frac{j_{0,0}}{j_{L,0}}\left(\frac{c_0}{c}\right)^{n-\gamma} \tag{12}$$

$n = 1$ is valid in the case of forced convection (stirred electrolyte). The mass and heat transfer induced by the density gradient in liquids in the gravitational field is natural or free convection. Levich[5] gave an approximate analytical solution for estimating the diffusion flux of the component that reacts and disappears on the surface of a vertical plate in a liquid. The electrochemical deposition of metals is a fair example of this kind of reaction.

A corresponding solution can be presented in the form $j \approx c_0^{1.25}$. Several authors[6–8] have reported a value of the concentration exponent of less than 1.25. Systematic investigations of metal electrodeposition on a vertical plate and thin metal wire[7,8] showed that the Levich solution is valid only when the temperatures of the thermo-isolated solution and of the surrounding air are equal, *i.e.*, under proper isothermal conditions. For even a small temperature difference, the value of the concentration exponent decreases considerably (for a temperature difference of 1.5 °C, the value of the exponent is 1.08). In addition, evaporation of the solution into dry air of the same temperature flowing over the electrolyte surface can also cause a decrease of the value of the concentration exponent.

A similar effect exist in the case of a superimposed magnetic field.[9]

In the case of copper electrodeposition[4] $\gamma = 0.75$ and

$$0.25 \leq n - \gamma \leq 0.5 \tag{13}$$

because of Eq. (10), but

$$n - \gamma \approx 0.25 \tag{14}$$

is a more realistic value even in slightly-stirred solutions, and

$$n - \gamma \approx 0.50 \tag{15}$$

for non-stirred solutions under isothermal conditions.

In both cases

$$n - \gamma < 1 \tag{16}$$

and if

$$c_0/c \to \infty \tag{17}$$

it follows from Eqs. (12), (16) and (17) that:

$$j_{0,c}/j_{L,c} \to \infty \tag{18}$$

meaning, in accordance with Eq. (7), that the degree of diffusion control increases with decreasing concentration of the reacting ion.

It was shown recently[10] that the exchange current density for a process for which the mechanism is known can be easily determined from the measured polarization curve, if the *IR* error is negligible.[11]

If

$$j = kj_L \tag{19}$$

where $0 < k < 1$, Eqs. (1) and (2) can be rewritten in the forms:

$$j_0 = \frac{kj_L}{(1-k)^{\gamma}\left(f_{c,k} - f_{a,k}\right)} \tag{20}$$

and

$$j_{0,app} = \frac{kj_L}{(1-k)(f_{c,k} - f_{a,k})} \tag{21}$$

respectively, where j_0 and $j_{0,app}$ are the true and approximate values of the exchange current density and $f_{c,k}$ and $f_{a,k}$ correspond to the current density from Eq. (19).

Using c_0 = 1.0 mol dm^{-3} $CuSO_4$ in 0.50 M H_2SO_4 as a reference solution and the corresponding values of $j_{L,0}$ = 100 mA/cm^2 and $j_{0,0}$ = 10 mA/cm^2, f_c = = $10^{\eta/120}$ and f_a = $10^{-\eta/40}$ and γ = 0.75 and 1, the polarization curves for electrodeposition from 1, 0.10 and 0.010 M $CuSO_4$ in 0.50 M H_2SO_4 are calculated using Eqs. (1), (2), (12), (14) and (15) and presented in Figs. 1 and 2. The polarization curves presented by the full lines in Figs. 1 and 2 were calculated using Eq. (1) and γ = 0.75 and the ones presented by the dashed lines, using Eq. (2) and hence, γ = 1. It can be seen from Figs. 1 and 2 that with increasing value of the $j_{0,c}/j_{L,c}$ ratio due to the decreasing concentration of the depositing ion, the degree of diffusion control increases. The polarization curves are practically the same for γ = 0.75 and 1 up to j/j_L = 0.3 for each j/j_L ratio. Hence, Eq. (2) can be successfully used instead of Eq. (1) in quantitative discussions at low current densities.

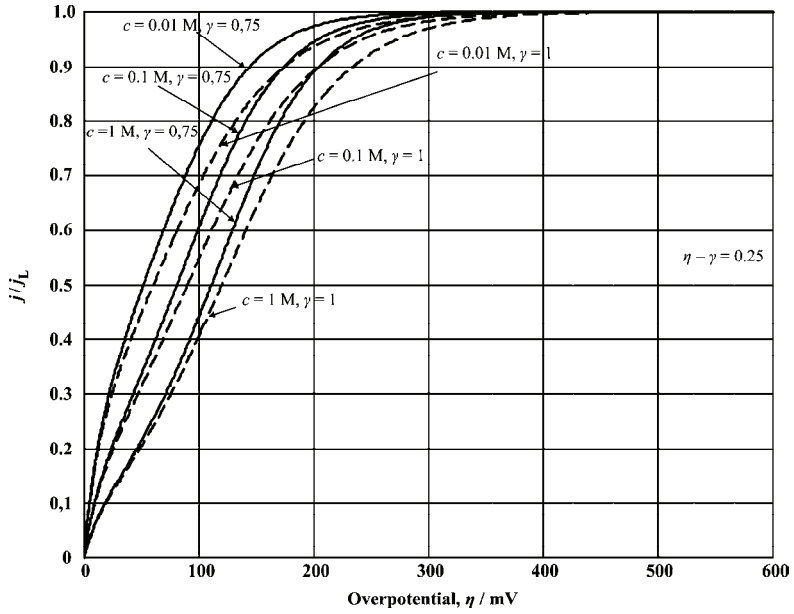

Fig. 1. Dependences j/j_L–η calculated from Eqs. (1) and (12) using c = 1.0, 0.10 and 0.010 mol dm^{-3}, c_0 = 1.0 mol dm^{-3}, $f_c = 10^{\eta/120}$, $f_a = 10^{-\eta/40}$, $j_{L,0}$ = 100 mA/cm^2, $j_{0,0}$ = 10 mA/cm^2 and $n - \gamma$= 0.25.

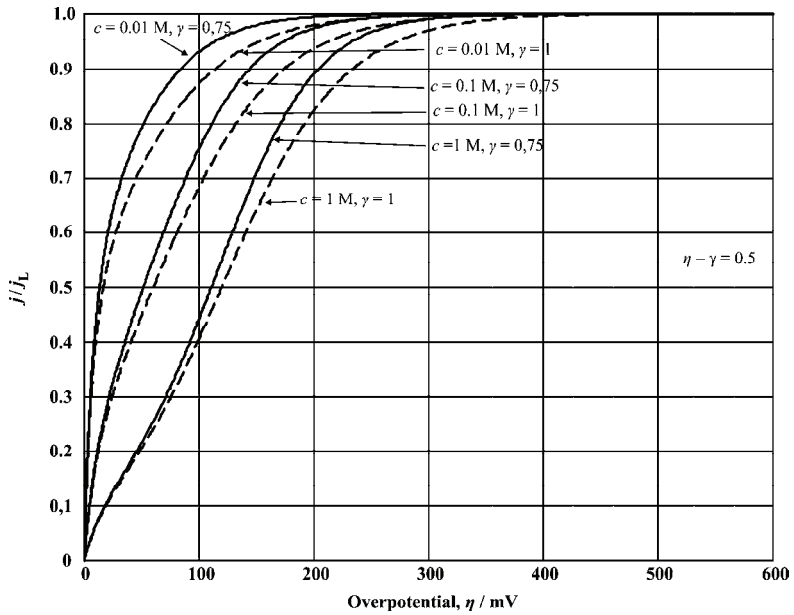

Fig. 2. Dependences j/j_L–η calculated from Eqs. (1) and (12) using c = 1.0, 0.10 and 0.010 mol dm^{-3}, c_0 = 1.0 mol dm^{-3}, $f_c = 10^{\eta/120}$, $f_a = 10^{-\eta/40}$, $j_{L,0}$ = 100 mA/cm^2, $j_{0,0}$ = 10 mA/cm^2 and $n - \gamma$= 0.5.

It follows from Eqs. (20) and (21) that

$$j_{0,app} = (1 - k)^{\gamma-1} j_0 \quad (22)$$

and the $j_{0,app}/j_0$ ratios calculated using Eq. (22) and $\gamma - 1 = 0.25$ as a function of k are presented in Table I.

TABLE I. Comparison of j_0 calculated using Eq. (8) (true values) and ones calculated using Eq. (21) (approximate values)

k	0.10	0.20	0.30	0.40	0.50	0.60	0.70	0.80	0.90
$j_{0,app}/j_0$	1.03	1.06	1.09	1.14	1.19	1.26	1.35	1.50	1.78

It can be seen from Table I that Eq. (21) can be successfully employed for the determination of the value of the exchange current density from the polarization curve up to $k = 0.2$ with an error lower than 5 % and up to $k = 0.3$ with an error lower than 10 %.

Obviously, the ratio of the exchange current density to the limiting diffusion one can also be calculated in the same manner with the same error.

EXPERIMENTAL

Copper was potentiostatically deposited from the following solutions: a) 0.020 M $CuSO_4$ + 0.50 M H_2SO_4, b) 0.050 M $CuSO_4$ + 0.50 M H_2SO_4 and c) 0.10 M $CuSO_4$ + 0.50 M H_2SO_4.

Electrodepositions were performed in an open cell at a temperature of 23.0±0.5 °C using a Wenking 7103 GIRH potentiostat. Doubly distilled water and analytical grade chemicals were used for the preparation of solutions for the electrodeposition of copper.

The working electrode was a stationary Pt wire covered with Cu film electrodeposited at an overpotential of 300 mV during 3.0 min from 0.10 M $CuSO_4$ in 0.50 M H_2SO_4.

The counter electrode was a copper foil placed close to the walls of the cell; the working electrode was placed in the middle of the cell, while the overpotential was adjusted *vs*. a copper electrode which was positioned at a distance of 0.2 cm from the surface of the working electrode.

In order to determine the exchange current densities of electrochemically deposited copper, the electrode was prepared by electrochemical deposition of copper on a Pt wire ($S = 0.45$ cm^2) from an aqueous solution of 0.10 M $CuSO_4$ in 0.50 M H_2SO_4 galvanostatically, at a constant current density of 4.0 mA/cm^2 during 1200 s. Then the cathodic and anodic polarization curves were recorded potentiodynamically at a scan rate of 1.0 mV s^{-1} in solutions containing 0.020, 0.050 and 0.10 M $CuSO_4$ in 0.50 M H_2SO_4 in the overpotential range –120 to 100 mV. In order to reach the steady state condition, the working electrode was held at a constant cathodic overpotential of –120 mV for 120 s before the measurements. Since the cathodic polarization curves were attained under mixed control, the exchange current densities were determined from the intercept of anodic and theoretical cathodic Tafel slopes.

The experiments for determining the exchange current densities were performed in a standard three compartment electrochemical cell at ambient temperature. A copper wire (99.999 %) in the same solution was used as the reference electrode, while a platinum wire served as the counter electrode. Both galvanostatic and potentiodynamic experiments were performed using a PAR 263A potentiostat/galvanostat.

RESULTS AND DISCUSSION

The polarization curves for the electrodeposition of copper from 0.020, 0.050 and 0.10 M $CuSO_4$ in 0.50 M H_2SO_4 at a temperature of 23±1 °C are shown in Fig. 3 and the ones normalized to the value of the limiting diffusion current density in Fig. 4.

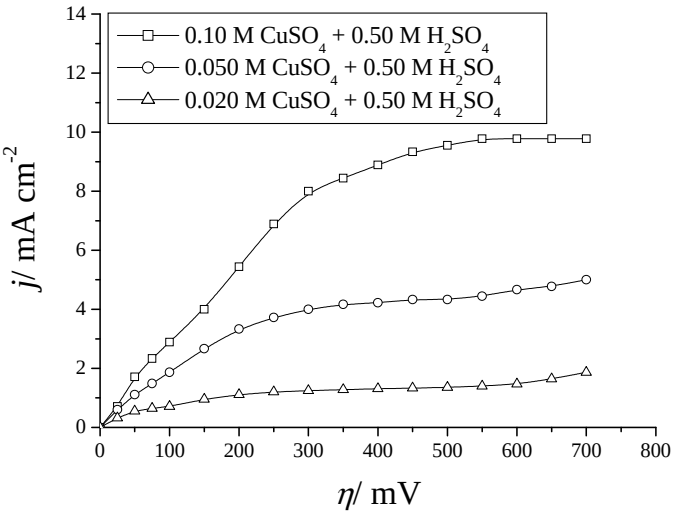

Fig. 3. Polarization curves for the electrodeposition of copper from 0.020, 0.050 and 0.10 M $CuSO_4$ in 0.50 M H_2SO_4 at a temperature of 23±1 °C.

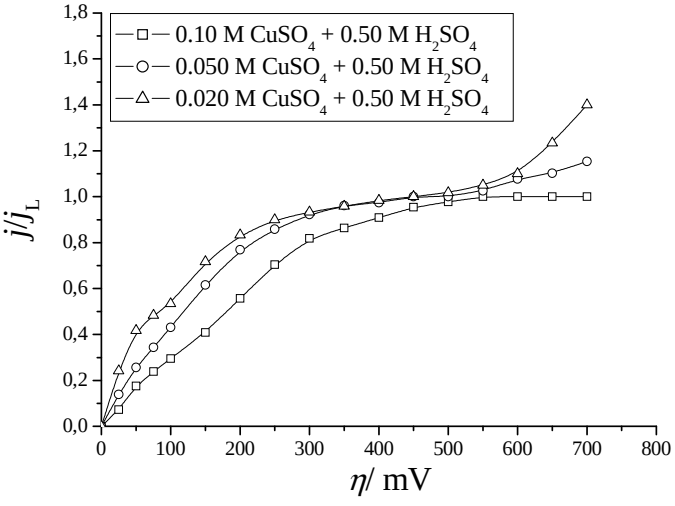

Fig. 4. Polarization curves for the electrodeposition of copper from 0.020, 0.050 and 0.10 M $CuSO_4$ in 0.50 M H_2SO_4 at a temperature of 23±1 °C normalized to the value of corresponding limiting diffusion current density.

The fact that the value of the ratio j_0/j_L increased with decreasing concentration of Cu(II) ions can be considered a good qualitative illustration of the increasing degree of diffusion control of the deposition process with decreasing concentration of the depositing ion (Figs. 1, 2 and 4).

Assuming that the *IR* error can be neglected in electrodeposition from the used electrolyte solutions, the values of j_0 listed in Table II were obtained using Eq. (21) and $k = 0.30$ and the data from Fig. 3, which are in fair agreement with the values obtained by the potentiodynamic recording of cathodic and anodic polarization curves.

TABLE II. Comparison of the j_0 values estimated by the proposed method (approximate values) and those determined by the potentiodynamic recording of the cathodic and anodic polarization curves (experimental values)

c ($CuSO_4$) / mol dm^{-3} (in 0.50 M H_2SO_4)	$j_{0,app}$ / mA cm^{-2}	$j_{0,exp}$ / mA cm^{-2}
0.020	0.36	0.24
0.050	0.54	0.70
0.10	0.85	1.3

Simultaneously, a simple method for the estimation of exchange current densities from polarization measurements is demonstrated.

In this way, it was shown that the degree of diffusion control increases with decreasing concentration of the reacting ion in metal electrodeposition processes, as was estimated earlier from the morphology of electrodeposited metals.[12]

Acknowledgments. This work was supported by the Ministry of Science of the Republic of Serbia under the research projects: “Deposition of ultrafine powders of metals and alloys and nanostructured surfaces by electrochemical techniques” (No. 142032G) and Contract No. 142044.

И З В О Д

УТИЦАЈ КОНЦЕНТРАЦИЈЕ РЕАГУЈУЋЕГ ЈОНА НА КОНТРОЛУ ПРОЦЕСА ЕЛЕКТРОХЕМИЈСКОГ ТАЛОЖЕЊА

ПРЕДРАГ М. ЖИВКОВИЋ[1], НЕБОЈША Д. НИКОЛИЋ[2], МИЛИЦА ГВОЗДЕНОВИЋ[1] и КОНСТАНТИН И. ПОПОВ[1,2]

[1]Технолошко–металуршки факултет, Универзитет у Београду, Карнегијева 4, 11120 Београд и
[2]ИХТМ – Центар за електрохемију, Универзитет у Београду, Његошева 12, 11000 Београд

У раду је испитиван утицај концентрације реагујућег јона на врсту контроле процеса електрохемијског таложења. Примењена је дигитална симулација поларизационих кривих на основу Newman-овог облика једначине поларизационе криве и Levich-еве зависности граничне дифузионе густине струје у условима природне конвекције. Предложен је једноставан метод одређивања густине струје измене на основу поларизационих мерења. Добијена је задовољавајућа сагласност са експериментално добијеним вредностима.

(Примљено 11. јула, ревидирано 12. новембра 2008)

REFERENCES

1. K.I. Popov, P. M. Živković, B. N. Grgur, *Electrochim. Acta* **52** (2007) 4696
2. P. M. Živković, B. N. Grgur, K. I. Popov, *J. Serb. Chem. Soc.* **73** (2008) 227
3. K. I. Popov, S. S. Djokić, B. N. Grgur, *Fundamental Aspects of Electrometallurgy*, Kluwer Academic/Plenum Publishers, New York, 2002, pp. VIII, 14, 15
4. J. S. Newman, *Electrochemical Systems*, Prentice-Hall Inc., Engelwood Cliffs, NJ, 1973, p. 177
5. V. G. Levich, *Physico-Chemical Hydrodynamics*, Prentice-Hall, Englewood Cliffs, NJ, 1962, p. 134
6. R. N. Adams, *Electrochemistry at Solid Electrodes*, Dekker, New York, 1969, p. 87
7. N. S. Blagojević, M. D. Maksimović, K. I. Popov, *Chem. Eng. J.* **16** (1978) 35, and references therein
8. M. D. Maksimović, N. S. Blagojević, K. I. Popov, *Bull. Soc. Chim. Beograd* **43** (1978) 637 (in Serbian)
9. N. D. Nikolić, *J. Serb. Chem. Soc.* **72** (2007) 787
10. N. D. Nikolić, Lj. J. Pavlović, M. G. Pavlović, K. I. Popov, *J. Serb. Chem. Soc.* **72** (2007) 1369
11. J. O'M. Bockris, A. K. N. Reddy, M. Gamboa-Aldeco, *Modern Electrochemistry 2A*, 2nd Ed., Kluwer Academic/Plenum Publishers, New York, 2000, p. 1107
12. K. I. Popov, N. V. Krstajić, *J. Appl. Electrochem.* **13** (1983) 775.

Journal of the Serbian Chemical Society
JSCS@tmf.bg.ac.rs • www.shd.org.rs/JSCS

J. Serb. Chem. Soc. 74 (3) 301–310 (2009)
JSCS–3832

UDC 543.34:546.212+543.544.1:676.2
Original scientific paper

Determination of inorganic anions in papermaking waters by ion chromatography

DARJA ŽARKOVIĆ[1#], ŽAKLINA TODOROVIĆ[2#], MILORAD KRGOVIĆ[3] and LJUBINKA RAJAKOVIĆ[3*#]

[1]*Belgrade Polytechnic, Brankova 17, 11000 Belgrade,* [2]*Vinča Institute of Nuclear Sciences, P.O. Box 522, 11001 Belgrade and* [3]*Faculty of Technology and Metallurgy, Karnegijeva 4, P.O. Box 494, 11000 Belgrade, Serbia*

(Received 21 April, revised 1 August 2008)

Abstract: A suppressed ion chromatography (IC) method for the determination of inorganic anions in process water from paperboard production was developed and validated. Common inorganic anions (Cl^-, NO_3^-, PO_4^{3-} and SO_4^{2-}) were detected in fresh and process water samples collected from a paperboard production system at 16 characteristic points. It was shown that the use of an IonPac®-AS14 column under isocratic conditions with Na_2CO_3/$NaHCO_3$ as the eluent and a suppression device proved to be a reliable analytical solution for the separation of the inorganic anions present in papermaking waters. This IC method is quite satisfactory concerning selectivity and sensitivity, and enables the determination of several inorganic anions over a wide concentration range. According to the obtained results, the total amount of analyzed inorganic anions was below 0.1 g/L, *i.e.*, below the critical value which may trigger operational problems in paper production.

Keywords: papermaking waters; ion chromatography; inorganic anions.

INTRODUCTION

A lot of efforts have been made to reduce the usage of fresh water and system closure in paper production.[1–5] The European Union Environmental Directive for Pulp and Paper Production commits producers to decrease fresh water consumption, which should be realized by water recirculation and water system closure.[6] In addition to the proven advantages, the closing up of the water system in paper production also brings different operational and product problems (chemical precipitation, low retention of fibers and fines, corrosion of equipment, microbiological growth, slime and odor inside mill and impurities in the final product).[7–11] These problems are mainly caused by increased concentrations of

* Corresponding author. E-mail: ljubinka@tmf.bg.ac.rs
# Serbian Chemical Society member.
doi: 10.2298/JSC0903301Z

water-soluble compounds in the process water, *i.e.*, dissolved and colloidal organic and inorganic compounds. Monitoring the quality of the process water is the most popular and effective measure for controlling detrimental phenomena in paper production.[12–15]

It has been estimated that the number of analytical water measurements, mostly physical ones, to be made for one paper machine per day could increase to 1.500–2.000.[16] Usually, basic methods for water analysis include the measurement of summative parameters. Being simple and rapid, they are traditionally predominant in the determination of papermaking process waters and effluents. Particularly, on-line chemical measurements are focused on monitoring pH and conductivity. However, the results obtained provide only information about the chemical behavior of the individual ions and compounds. Therefore, there is a necessity for separation techniques, such as ion chromatography (IC) or capillary electrophoresis (CE), to verify the concentrations of individual ions.[17] These rapid, powerful, high-throughput and specific identification techniques, such as IC with suppressed conductivity detection, are required for on-line separation and simultaneous determination of ion species.[18]

IC Represents a universal analytical technique for the separation and quantitative determination of specific ion species. Complex mixtures of anions or cations can be separated to the level of specific ions and then quantified in a relatively short time.

The main applications of IC methods are in the determination of trace anions in ultra pure water, in the pharmaceutical industry, electronics, power plants, pulp and paper production, *etc*.[19] In modern paper production, the determination of the amount of anions in the process water is an important control parameter. The IC method can detect and quantify substances that cause color, smell and slime in the production process, as well as salts and other corrosive substances. These disturbing substances include volatile organic acids (acetic, formic, lactic and butyric) and inorganic salts present as anions: chloride, fluoride, sulfate, nitrate, *etc*.

The aim of this work was to develop and validate IC method for the determination of inorganic anions in process water of paperboard production. Fresh and process water samples from production system were analyzed by suppressed IC method. It was examined that, concerning selectivity and sensitivity, if combination of selected columns, eluent and operating parameters was well established, IC method was able to determine several inorganic anions in a wide concentration range.

EXPERIMENTAL

Water from one paperboard production system with a daily output of 180 t of coated and uncoated paperboard was analyzed. The main feedstock materials were waste paper (70 %), bleached and unbleached ground wood and softwood pulp (primary fibers), sludge, fillers,

$CaCO_3$, different additives, *etc*. Water was samples at 16 characteristic points during the commercial production of 400 g/m^2 paperboard with an average water consumption of 32 m^3/t. A schematic description of the production process in the examined paperboard mill with control points for water analysis is given in Fig. 1.

The produced paperboard was made up of seven layers, each formed on a separate former. The bottom layer (made of unsorted waste paper) was formed on formers 1 and 3. The inner layer was made of low-grade waste paper (on formers 4, 5 and 6) and the upper layer was made of high-grade waste paper (formers 7 and 8).

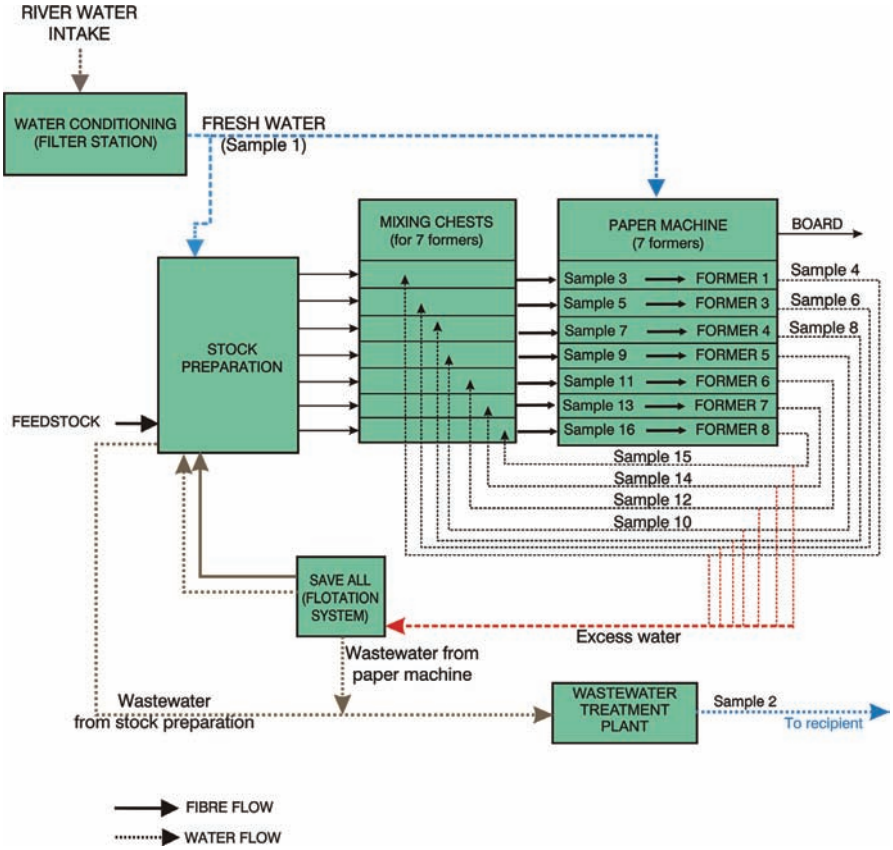

Fig. 1. Production process in a paperboard mill and the sampling points.

Instrumentation and operating conditions

Determination of inorganic anions by IC method was realized using a Dionex DX-300 ion chromatograph (Dionex, Sunnyvale, CA, USA). The instrument consists of an advanced gradient pump and a CDM-3 conductivity detector. The employed analytical separation column was a Dionex IonPac®-AS14 preceded by a Dionex IonPac®-AG14 guard column. Both columns were made of the same polymer resin for anion exchange. An Anion Self Regenerating Suppressor (ASRS ultra) was used. Dionex Peaknet ver. 5.1 software was employed for instrument control, data collection and processing. A Spectra-Physics model AS3500 autosampler was used for the direct programmed injection of samples.

TABLE I. Operating conditions for anion separation by suppressed IC method under isocratic conditions

Guard column	IonPac AG14 (4 mm×50 mm) anion exchange
Suppressor	ASRS-ULTRA (4 mm)
Mobile phase – Eluent	4.0 mM Na_2CO_3/1.0 mM $NaHCO_3$ (1:1)
Eluent flow rate	0.70 mL/min
Sample volume	20 µL
Injection technique	Direct
Detection	Suppressed conductivity
Full scale range	100 µS
Suppressor current	50 mA

Anion determination was realized under the optimal operating conditions presented in Table I. These parameters were determined by trial-and-error and were the same for all measurements of the water samples from the paper production system.

Separation and detection of anions were performed at room temperature and lasted for about 17 min for each sample.

Chemical reagents, standard solutions and eluent

All chemicals for the preparation of standard solutions and the eluent were of analytical-reagent grade and were dissolved in deionized (milli Q) water with a specific resistance of 18.2 MΩ cm. The stock standard solutions were stored at 4 °C. Standard working solutions of different concentrations were prepared by diluting the stock solutions with deionized water. Fresh working eluent was prepared daily, filtered through a 0.2 µm pore size membrane filter (Millipore, USA) and degassed before use. All standard solutions for calibration were stored in polyethylene containers.

Samples

Process water samples were collected *in situ* at selected control points in the production system. All samples were handled carefully and analyzed in the chemical laboratory as quickly as possible. Water samples with a higher turbidity (from headboxes and whitewater samples) were analyzed after removal of the suspended solids using a laboratory centrifuge (1500 min^{-1}, 30 min). All samples were filtered through a 0.2 µm membrane filter (Millipore, USA) just before injection.

RESULTS AND DISCUSSION

Common inorganic anions (Cl^-, NO_3^-, PO_4^{3-} and SO_4^{2-}) were identified and quantified applying the IC method under the operating conditions shown in Table I.

All the studied anions were determined in one chromatographic run. The identification and quantification of each anion were realized from the retention time and peak area. A typical chromatogram of a water sample is presented in Fig. 2.

The chromatographic parameters for the detected anions are presented in Table II. The recovery (*R*) and the relative standard deviation (*RSD*) of the peak area for spiked samples are given in Table III.

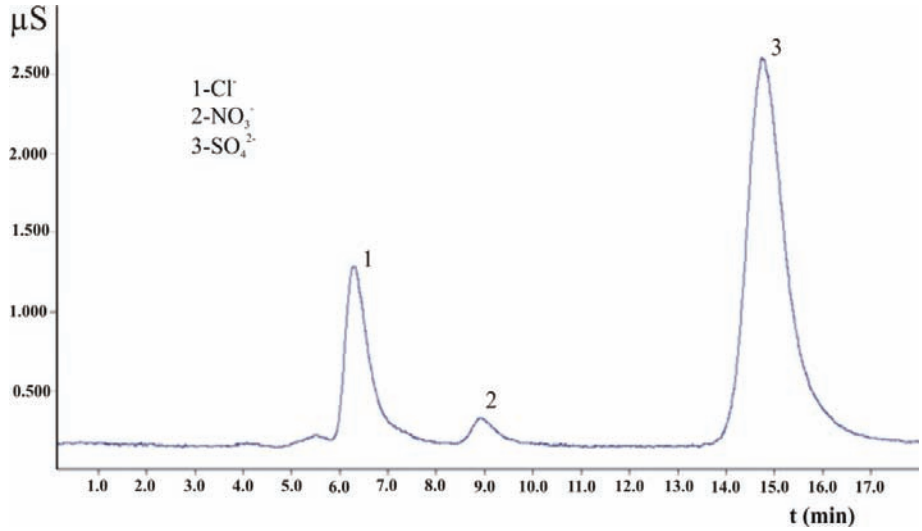

Fig. 2. Chromatogram of whitewater from former 8 (sample 15).

Table II confirms that the calibration lines obtained by the selected IC method (using the operating parameters presented in Table I) are linear with a correlation coefficient over 0.999 (except for phosphate) over the whole working concentration range. The calculated values for parameter *a* are much higher than is usual (for a calibration line which starts at the [0,0] coordinates). This can be explained by relatively large peak areas in the chromatograms.

TABLE II. Chromatography parameters for the detected anions: t_R – retention time; *a* and *b* – parameters for the calibration curve ($y = a + bx$, y – peak area, x – concentration); *r* – correlation coefficient

Anion	t_R / min	$-a\times10^{-4}$ Area unit	$b\times10^{-4}$ Area unit L mg^{-1}	*r*
Cl^-	6.28	2.1528	2.2003	0.9993
NO_3^-	8.88	1.8996	1.1261	0.9996
PO_4^{3-}	12.8	1.4429	1.4704	0.9987
SO_4^{2-}	14.6	9.2543	1.5833	0.9995

TABLE III. Recovery (*R*) and relative standard deviation (*RSD*) of the peak area for spiked water samples

Anion	*R* / %	*RSD* / %
Cl^-	102	2.4
NO_3^-	103	2.7
PO_4^{3-}	97	3.2
SO_4^{2-}	101	2.0

The previously developed and validated IC method was used as a control analytical tool for the analysis of water samples taken from the production pro-

cess. Sixteen different samples of process and waste water were prepared and injected into the chromatograph with Na_2CO_3/$NaHCO_3$ as the mobile phase. The concentrations of the commonly detected anions in the investigated water samples are presented in Table IV, while the descriptive statistics and reproducibility data (*RSD*) of the peak areas for the target inorganic anions in representative samples are given in Table V.

TABLE IV. Mean concentration values of the detected anions calculated from the peak areas (5 injections for each sample)

Sampling point/water type	Concentration, mg/L[a]			
	Cl^-	NO_3^-	PO_4^{3-}	SO_4^{2-}
Filter station (fresh water)	6.49	3.85	<0.05	35.5
Effluent to recipient	10.61	<0.01	<0.05	54.5
Headbox to former 1	11.33	<0.01	1.31	52.0
Whitewater from former 1	12.11	<0.01	<0.05	57.2
Headbox to former 3	7.61	<0.01	2.81	34.2
Whitewater from former 3	13.64	<0.01	4.53	64.4
Headbox to former 4	15.32	<0.01	3.91	67.3
Whitewater from former 4	14.63	0.14	1.90	65.4
Headbox to former 5	16.44	<0.01	3.25	76.9
Whitewater from former 5	14.02	<0.01	3.91	64.4
Headbox to former 6	15.21	<0.01	8.46	70.3
Whitewater from former 6	17.84	0.06	3.41	79.2
Headbox to former 7	8.85	2.10	<0.05	51.5
Whitewater from former 7	9.75	1.62	<0.05	51.7
Whitewater from former 8	8.10	2.69	<0.05	48.0
Headbox to former 8	8.08	2.68	<0.05	108.1

[a]Uncertainty of measurement presents 95 % of significance level: 0.05 mg/L for Cl^-, 0.01 mg/L for NO_3^- and PO_4^{3-} and 0.1 mg/L for SO_4^{2-}

TABLE V. Descriptive statistics and *repeatability* data (*RSD*) of the peak area for the target inorganic anions in samples 1, 2, 8 and 12 (n = 5)

Anion	Sample 1 (Filter station/fresh water)				Sample 2 (Effluent to recipient)				Sample 8 (Whitewater from former 4)				Sample 12 (Whitewater from former 6)			
	Concentration mg/L			*RSD* %	Concentration mg/L			*RSD* %	Concentration mg/L			*RSD* %	Concentration mg/L			*RSD* %
	Min	Max	Mean		Min	Max	Mean		Min	Max	Mean		Min	Max	Mean	
Cl^-	6.2	6.90	6.5	3.2	9.2	11.8	10.6	5.5	12.9	15.8	14.6	7.3	16.6	18.3	17.8	7.8
NO_3^-	3.7	4.0	3.8	3.0	nd[a]	nd	–	–	0.06	0.24	0.14	7.8	0.04	0.10	0.06	8.5
PO_4^{3-}	n.d.	n.d.	–	–	nd	nd	–	–	1.5	2.5	1.9	7.1	3.0	3.8	3.4	8.2
SO_4^{2-}	34.6	36.7	35.5	2.3	52.9	55.8	54.5	4.4	63.8	66.7	65.4	6.0	78.4	80.1	79.2	6.2

[a]Not detectable

Chlorides and sulfates were detected in all the water samples, which can be explained by the addition of these chemicals as retention aids into the production

process. Comparing the contents of Cl^- and SO_4^{2-} in the fresh water and the effluent (samples 1 and 2), no great difference could be observed. Furthermore, it shows that a larger amount of the added chemicals was settled down with the fibers and kept in the paper, which indicates a highly efficient retention of the fibers. Comparing the contents of Cl^- and SO_4^{2-} in water samples from the headboxes of different formers, the highest concentrations were recorded for formers 4–6 (and 8 for sulfates). These formers are used to make the inner layers of paperboards, except former 8 which is used for the upper layers. The middle layer is made up of the lowest quality recycled paper with the shortest fibers. On these formers, the retention is not so intense, which demands addition of retention aids. This is also the reason for the higher concentrations of residual (dissolved) Cl^- and SO_4^{2-} anions in the whitewaters from formers 4–6 and 8 (for sulfates).

Nitrates and phosphates were detected in 7 of 16 samples (resp. 9 of 16 samples), and their concentrations were below 3.85 (NO_3^-) and 8.46 (PO_4^{3-}) mg/L, respectively. It is important to perceive that neither NO_3^- nor PO_4^{3-} were detected in sample 2 (effluent to recipient). These anions, when present in higher concentrations, might result in higher values of total nitrogen and phosphorus in the paper production effluent, which is limited by the EU Environmental Directive for Pulp and Paper Production.

In addition to the anions presented in Table IV, Br^-, NO_2^- and F^- were also analyzed but they were not detected, because their concentrations were below 0.01 mg/L. Nitrites are unstable at higher temperatures (about 50 °C, which is a characteristic of process water), which might be the reason why they were not detected. Also, nitrites can hardly be detected in the presence of organic acids, which are predominantly present in papermaking waters.

Reproducibility tests were based on five injections for each water sample. The reproducibility data for the peak areas, obtained using the operation parameters described in Table I, were statistically evaluated from the relative standard deviation (*RSD*) and are presented in Table V.

All *RSD* values of the peak areas for the target anions (presented in Table V) were less than 9 %. Comparing the *RSD* values for examined samples, it can be seen that the best results of the precision of the measurement (lowest *RSD* value) were recorded for sample 1 – fresh water from the filter station. This can be explained by the low presence of interfering substances in the fresh water, which were previously removed in the clarification process. Comparing *RSD* values for the detected anions, it can be noticed that the highest precision in all the samples (lowest *RSD* value) was recorded for SO_4^{2-}. This fact might be explained by the highest concentrations (and the largest peak areas) of sulfates in all the analyzed water samples.

The obtained results show that the use of an IonPac-AS14 column under isocratic conditions with $Na_2CO_3/NaHCO_3$ solution as the eluent together with a

suppression device provides for good separation of inorganic anions from papermaking waters. All the detected anions were eluted in less than 17 min and their peaks were well separated (Fig. 2). It is a suitable method for the determination of anions in the concentration range from 0.1 to 100 mg/L by direct sample injection and it can be used for a routine analysis of papermaking waters. Direct injection does not require any previous pre-concentration of the samples and presents a simple but reliable method for ion analysis.

The results given in Table IV confirm that the total amount of analyzed inorganic anions (except for sample 16 – headbox to former 8) was below 0.1 g/L, *i.e.*, far below the critical value, which may induce operational problems caused by the anions present. However, increased concentration of sulfates in sample 16, which raised up the total amount of inorganic anions to 0.119 g/L, had not caused any operational problem. According to practical experiences, further closing of the water system with increased recirculation, as well as the usage of recycled fibers instead of cellulose may cause an increase in the concentration of detrimental anions, which should be controlled.[12]

As expected, the highest concentration of anions was recorded for sulphates, which are the main cause of process equipment corrosion. To determine inorganic anions such as Br^-, NO_2^- and F^-, which could not be detected in the present study, further investigation may include modifications in the eluent, eluent flow rate, stationary phase or column temperature.

Also, the analysis of papermaking process water should include organic acids (lactic, acetic, formic and butyric acid). These organic acids are the metabolic products of microorganism population growth in the closed water system of paper production. Increased concentration of volatile organic acids may cause a decrease in production efficiency, corrosion problems, as well as the appearance smell and slime in paper mills.

CONCLUSIONS

Inorganic anions in papermaking waters were successfully determined by a suppressed IC technique using an anion-exchange separation column, Na_2CO_3/ /$NaHCO_3$ solution as the eluent, and a suppression device. Major inorganic anions, usually present in papermaking waters (Cl^-, NO_3^-, SO_4^{2-} and PO_4^{3-}), were efficiently separated and quantified. However, some inorganic anions (Br^-, NO_2^- and F^-) could not be detected because of their lower concentrations (below 0.01 mg/L), which remains to be solved in further examinations. The total amount of detected inorganic anions was below 0.1 g/L, which is the critical value for triggering operational problems in paper production. The highest concentration of anions was recorded for sulfates, which are the main cause of corrosion of process equipment.

Further closure of the water system with increased recirculation, as well as an enhanced usage of recycled fibers as a raw material, will affect an increase in the concentration of detrimental anions. Monitoring of these anions by the IC method should be an integral part of modern paper production systems, in order to prevent operational and product problems.

И З В О Д

ОДРЕЂИВАЊЕ НЕОРГАНСКИХ АНЈОНА У ВОДАМА ИЗ ПАПИРНЕ ИНДУСТРИЈЕ МЕТОДОМ ЈОНСКЕ ХРОМАТОГРАФИЈЕ

ДАРЈА ЖАРКОВИЋ[1], ЖАКЛИНА ТОДОРОВИЋ[2], МИЛОРАД КРГОВИЋ[3] и ЉУБИНКА РАЈАКОВИЋ[3]

[1]Висока школа струковних студија "Београдска политехника", Бранкова 17, 11000 Београд, [2]Институт за нуклеарне науке "Винча", п.пр. 522, 11001 Београд и [3]Технолошко–металуршки факултет, Карнегијева 4, п.пр. 494, 11120 Београд

Одређивање неорганских анјона у водама кружног тока у производњи папира вршено је методом супресивне јонске хроматографије (IC). Најважнији неорганski анјони (Cl^-, NO_3^-, PO_4^{3-} и SO_4^{2-}) квантитативно су одређени у 16 узорака свеже и процесне воде једног система за производњу картона. Добијени резултати указују на то да употреба IonPac-AS14 сепарационе колоне у изократским условима са елуентом $Na_2CO_3/NaHCO_3$ и саморегенеришућим анјонским супресором (ASRS) представља поуздану IC методу за раздвајање неорганских анјона у процесним водама папирне индустрије. Резултати су показали да је изабрана IC метода сасвим задовољавајућа у погледу селективности, осетљивости и прецизности, и да је била идеална за одређивање анјона у опсегу концентрација mg/L. На основу резултата, укупна концентрација испитиваних неорганских анјона је испод 0,1 g/L, што представља критичну вредност за појаву оперативних проблема у системима за производњу папира.

(Примљено 21. априла, ревидирано 1. августа 2008)

REFERENCES

1. L. Webb, *Pulp Pap. Int.* **4** (2003) 33
2. C. Bulow, G. Pingen, U. Hamm, *Pulp Pap. Int.* **8** (2003) 14
3. K. Edelmann, S. Kaijaluoto, M. Karlsson, *Das Papier* **6A** (1997) 138
4. N. Zakrajšek, J. Zule, A. Može, J. Golob, *Acta Chim. Slov.* **52** (2005) 67
5. D. Žarković, M. Krgović, Lj. Rajaković, *Hem. Ind.* **8** (2004) 327
6. *IPPC BREF*, *The Pulp and Paper Industry*, European Commission, July 2002
7. L. Baghello, D. Eklund, *J. Pulp Pap. Sci.* **7** (1999) 246
8. L. Allen, M. Polverari, B. Levesque, W. Francis, *Tappi J.* **82** (1999) 189
9. A. Dunham, K. Tubergen, S. Govoni, J. Alfano, *J. Pulp Pap. Sci.* **3** (2001) 95
10. R. H. Pelton, L. H. Allen, H. M. Nugent, *Pulp Pap. Canada* **81** (1980) 54
11. F. Linhart, W. J. Auhorn, H. J. Degen, R. Lorz, *Tappi J.* **60** (1987) 79
12. K. Edelmann, S. Kaijaluoto, M. Nappa, *Control of detrimental phenomena in papermaking – new and innovative processes for radical changes in the European Pulp & Paper Industry* (project), VTT Energy, 2004
13. D. Žarković, *M. Sc. Thesis*, Faculty of Technology and Metallurgy, University of Belgrade, 2004 (in Serbian)
14. M. Rice, J. Roeraade, B. Holmbom, *Nord. Pulp Pap. Res. J.* **14** (1999) 292

15. B. Holmbom, *Analysis of paper mill process waters and effluents, pulping and paper-making*, Springer, Berlin, 1999, pp. 269–285
16. R. Kokkonen, H. Siren, S. Kauliomaki, S. Rovio, K. Luomanpera, *J. Chromatogr. A* **1032** (2004) 243
17. H. Siren, R. Kokkonen, T. Hiissa, T. Sarme, O. Rimpinen, R. Laitinen, *J. Chromatogr. A* **895** (2000) 189
18. J. Weiss, *Handbook of Ion Chromatography*, 3rd Ed., Wiley-VCH, Weinheim, 2004
19. D. Čičkarić, I. Deršek-Timotić, A. Onjia, Lj. Rajaković, *J. Serb. Chem. Soc.* **70** (2005) 995.

Journal of the Serbian Chemical Society
JSCS@tmf.bg.ac.rs • www.shd.org.rs/JSCS

J. Serb. Chem. Soc. 74 (3) 311–315 (2009)
JSCS–3833

UDC 681.586.5:546.982–71:543.33/
/.34:66.094.25
Short communication

SHORT COMMUNICATION

A novel optode sensor for the determination of palladium(II) in water and a hydrogenation catalyst

HOSSEIN TAVALLALI* and MARYAM GHANAAT PISHEH JAHROMI

Payame Noor University (PNU), Shiraz, 71365-944, Iran

(Received 1 July, revised 16 September 2008)

Abstract: A novel optical sensor was established to determine palladium(II) based on the immobilization of 1-(2-pyridylazo)-2-naphthol (PAN) on a triacetylcellulose membrane. Palladium ions react with the immobilized PAN and cause a decrease in the absorbance of the membrane at 469 nm. The response time of the optode was 8–10 min depending on the concentration of Pd(II) ions. This sensing phase had a dynamic linear range of 0.10–12.0 μg ml^{-1} palladium ions with a limit of detection of 65 ng ml^{-1}. The sensor can readily be regenerated using an ethylenediamine solution. The sensor could be fully regenerated, and the color change was fully reversible. The method was successfully applied for the determination of Pd(II) in synthetic aqueous solutions and in a hydrogenation catalyst sample.

Keywords: optode; 1-(2-pyridylazo)-2-naphthol (PAN); palladium(II); hydrogenation catalyst; triacetylcelluose.

INTRODUCTION

The significance of palladium as a transition metal lies in its wide spectrum of application, especially in the electrical and electronic industries, catalyst, dentistry and medical devices, jewelry and recently as nano-particles for the development of new active catalyst.[1–3] It was thus considered worthwhile to explore the possibilities of developing a simple, sensitive and selective method for the determination of traces of palladium in various samples. Many methods have already been developed for the determination of palladium in real samples. These are based on atomic absorption spectrometry (AAS) and extractive spectrophotometric methods.

The AAS instrumental techniques are: atomic absorption (AAS), both flame (FAAS) and electrothermal spectrometry (GFAAS).[4] Although these methods

* Corresponding author. E-mail: tavallali@pnu.ac.ir; tavallali@yahoo.com
doi: 10.2298/JSC0903311T

have good sensitivity, they require expensive instruments, well-controlled experimental conditions and a profound sample preparation.

The extractive spectrophotometric methods employ many organic complexing reagents[5,6] which can be used for the determination of palladium, but they suffer from several disadvantages, such as low sensitivity, incomplete extraction and interference from a large number of foreign ions.[7–9]

In this communication, the first optode for the determination of palladium ions is introduced. Although a few sensors exist for the determination of palladium,[10–11] there are some difficulties, such as pretreatment, higher detection limits and complex procedures. In the present study, PAN was employed as an ionophore because of its ability to form highly colored complexes with transition metals[12] and its solubility in the membrane phase. It was immobilized on a triacetylcelluose membrane for the determination of low levels of palladium ions. The membrane responds to palladium ions by changing in absorbance, it can be applied as a relatively selective reagent for Pd(II) at pH 2.0.

EXPERIMENTAL

Reagents

All the reagents such as PAN and ethylenediamine were supplied by Merck and all solutions were prepared with double distilled water. The Pd(II) solution was prepared by dissolving 1.664 g of palladium chloride (Merck) in a minimum amount of 2.0 mol L^{-1} hydrochloric acid solution in a one liter volumetric flask and finally made up to the mark with an identical hydrochloric acid solution. It was standardized by an indirect method using EDTA.[13]

Apparatus and measurement procedure

A Shimadzu 1601 PC UV–visible spectrophotometer with 1.0 cm quartz cells was used for the absorbance studies. A Jenway model 3510 pH-meter with a combined glass electrode was used for pH adjustment. A Sense AA GBC Scientific Equipment atomic absorption spectrometer was used to compare the result.

The membrane prepared according to a procedure given in the literature[18] was placed in a 2.5 ml trichloroacetic acid buffer (0.20 M) of pH 2.0 for several seconds to reach equilibrium. The membrane was placed vertically inside a quartz cell, hence, the optical path passed straight through the membrane. Then a solution with a specific concentration of analyte was added and the difference in the absorbance of the immobilized form of PAN was measured at 469 nm before and 600 s (equilibration time) after the addition of the analyte. In addition, no difference in the absorbance at 469 nm of the membrane was detected in a blank solution during 600 s.

RESULTS AND DISCUSSION

The absorption spectra of immobilized PAN obtained after equilibration in buffer solutions (pH 2.0) containing different concentrations of palladium are shown in Fig. 1. The spectral change is because of the addition of Pd(II) ions and the complex formation. Considering Fig. 1, the Pd(II) complex has two absorption peaks at pH 2.0, the first one of which is located on 659 nm and the second at 611 nm. Also, it can be seen that upon addition of increasing amounts of Pd(II)

ions, the absorbance of the complex increases at the expense of the absorbance of free ligand at 469 nm, showing a sharp isosbestic point at 515 nm, supporting the formation of a 1:1 metal ion–PAN complex. The wavelength of 469 nm was selected for further studies because of the higher sensitivity at this wavelength.

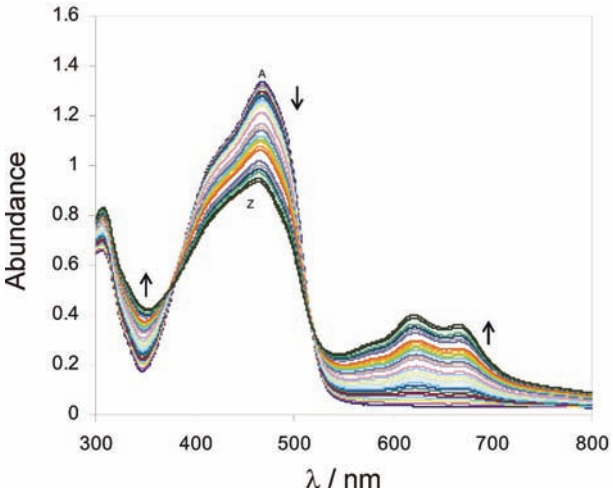

Fig. 1. Absorption spectra of the optode film in response to the addition of Pd(II) ions in the concentration range 0–14.0 μg mL^{-1} at pH 2.0 (A–Z show the increase in concentration of Pd(II) ions by the addition of 0.46 μg ml^{-1} Pd(II) ions in each interval).

The absorbance was measured at 469 nm for 1.0×10^{-5} M (2.0 μg ml^{-1}) palladium ions at different pH values. The blank membrane (membrane without PAN in the buffer solution) was taken as the reference. The absorbance measurement are expressed as absorbance difference, which was defined as the difference between the absorbance of the immobilized PAN alone and the absorbance of the Pd(II)–PAN complex at 469 nm. With increasing pH value from 1.0 to 5.0, the difference in the absorbance reached a maximum at pH 2.0 and then decreased sharply. This phenomenon might be due to the fact that at low pH values (pH < 2), complexation is weak. At pH values higher than 2, Pd(II) forms different hydroxide species ($Pd(OH)_n^{(n-2)-}$), which make complex formation with PAN impossible.[26]

The absorbance difference *versus* the Pd(II) concentration exhibits a linear range between 0.10 and 12.0 μg ml^{-1}. The regression equation is:

$$R = 0.0241c + 0.0251 \quad (1)$$

where R is the response expressed as the decrease of the absorbance of the film at 469 nm for a fixed time of 10 min and c is the concentration of Pd(II) in μg ml^{-1}, with a correlation coefficient of 0.9987. The detection limit, which was estimated as the concentration of analyte producing an analytical signal equal to three times the standard deviation of the blank signal, was found to be 65 ng ml^{-1}.

An important analytical feature of any optode film is its response time. In this work, the optode film was found to reach 95 % of the final signal after 8–10

min, depending on the concentration of Pd(II) ions. In general, the response time was lower in concentrated solutions than in dilute ones.

The lifetime of membrane was determined by adding a buffer solution (pH 2.0) in a quartz cell including a film. The signal was recorded at wavelength of 469 nm over a period of about 24 h. No significant loss of the indicator occurred during this time. When the membrane was exposed to light, no drift in the signal was observed and the membrane was stable over the period of the experiment with no leaching of the indicator.

Concerning membrane regeneration, the best result was obtained by applying ethylenediamine, which gave short membrane regeneration times (3–5 s). After regeneration before the next palladium concentration measurement, the optode should be placed in buffer (pH 2.0) for 15 min.

To determine the selectivity of the proposed method, interference of a number of ions was studied. The main interference was Cu(II), which can be eliminated by 0.10 M ascorbic acid. It is apparent from the study that discrimination between different metals can be achieved by the control of several parameters, including the absorption wavelength, the pH and the sample contact time in addition to the use of masking agents.

The developed optical sensing method for Pd(II) was successfully applied for the determination in synthetic aqueous solutions and hydrogenation catalyst. Various water samples with different contents of Pd(II) and a hydrogenation catalyst were prepared and analyzed employing the recommended procedure. The results were in perfect agreement with those obtained by direct atomic-absorption spectrometry. The results are presented in Table I.

TABLE I. Determination of Pd(II) in synthetic aqueous solutions and a hydrogenation catalyst by the proposed optode method and by AAS

Sample	Palladium claimed, wt. %	Pd (II) added, μg ml^{-1}	Pd (II) found, μg ml^{-1}		Recovery %
			AAS Method	Proposed method	
Solution 1	–	1.50	1.48	1.46	97.3
Solution 2	–	3.40	3.37	3.33	97.9
Solution 3	–	5.50	5.52	5.46	99.3
Solution 4	–	8.80	8.80	8.75	99.4
Solution 5	–	11.40	11.42	11.45	100.4
Catalyst	0.03–0.04[a]	–	0.037[b]	0.035[b]	–

[a]The catalyst 7741-T, which is used in the Amir Kabir Petrochemical Co., Iran, was treated twice with 10 ml portions of aqua regia; [b]the unit is wt. %

CONCLUSIONS

The described optode is easily prepared and provides a simple and inexpensive means for the determination of Pd(II) ions. The membrane responds to palladium ion by decreasing absorbance of PAN. The sensor can be regenerated readily with a solution of ethylenediamine and has a long lifetime. The response

of the optode was reproducible and the optode presented a good selectivity for Pd(II) over other metal ions, except for Cu(II) which can be masked using ascorbic acid. Since the sensor does not require solvent extraction, it can compete with standard optical fibers. The sensor can be applied for the analysis of real samples.

Acknowledgments. The authors gratefully acknowledge the support of this work by the Shiraz Payame Noor University Research Council.

И З В О Д

НОВИ ОПТИЧКИ СЕНЗОР ЗА ОДРЕЂИВАЊЕ ПАЛАДИЈУМ(II) ЈОНА У ВОДИ И У КАТАЛИЗАТОРУ ЗА ХИДРОГЕНОВАЊЕ

HOSSEIN TAVALLALI и MARYAM GHANAAT PISHEH

Payame Noor University (PNU), Shiraz, 71365-944, Iran

Формиран је нови оптички сензор за одређивање паладијум(II) јона заснован на имобилизацији 1-(2-пиридилазо)-2-нафтола (ПАН) на мембрани од триацетилцелулозе. Јони паладијума реагују са имобилисаним ПАН-ом и проузрокују смањење абсорбанције мембране на 469 nm. Време одзива сензора је 8–10 min, зависно од концентрације Pd(II) јона. Ова сензорска фаза поседује динамички линеарни одзив у опсегу концентрација Pd(II) јона од 0,10––12,0 μg ml^{-1}, са границом детекције од 65 ng ml^{-1}. Сензор се лако регенерише раствором етилендиамина. Он се потпуно регенерише, а промена боје је потпуно повратна. Метод је успешно примењен за одређивање Pd(II) у синтетичким воденим растворима и у катализатору за хидрогеновање.

(Примљено 1. јула, ревидирано 16. септембра 2008)

REFERENCES

1. T. N. Lokhannde, M. A. Anuse, M. B. Chavan, *Talanta* **46** (1998) 163
2. R. Sahu, S. M. Sondhi, B. Gupta, *Talanta* **42** (1995) 401
3. A. Tunceli, A. R. Turker, *Anal. Sci.* **16** (2000) 81
4. R. R. Barefoot, J. C. Van Loon, *Talanta* **49** (1999) 1
5. D. G. Gambarov, A. M. Ayubova, S. R. Azimova, *Azerb. Khim. Zh.* **2** (1981) 122 (in Russian)
6. A. Kumar, M. F. Hussain, M. Satake, B. K. Puri, *Bull. Chem. Soc. Japan* **55** (1982) 3455
7. S. G. Kawathar, R. V. Nimbalkar, *J. Ind. Chem. Soc.* **74** (1997) 69
8. A. N. Shetty, V. R. Gadag, *Bull. Chem. Soc. Japan* **66** (1993) 2536
9. P. J. Lopez, J. A. M. Leyva, *Quim. Anal*. **3** (1984) 226
10. M. Aghamohammadi, N. Alizadeh, *Anal. Chim. Acta* **480** (2003) 299
11. N. Pourreza, S. Rastegarzadeh, *Can. J. Anal. Sci. Spectros.* **49** (2004) 314
12. F. Lazaro, M. D. Luque de Castro, M. Val Carcel, *Anal. Chim. Acta* **214** (1988) 217
13. G. H. Jeffery, J. Bassett, J. Mendham, R. C. Denney, *Vogel's Textbook of Quantitative Chemical Analysis, 5th Ed.*, Longman Scientific and Technical, New York, 1989, p. 327
14. A. Safavi, M. Bagheri, *Sens. Actuators B* **90** (2003) 143
15. J. Lurie, *Handbook of Analytical Chemistry*, Mir Publisher, Moscow, 1978.

Journal of the Serbian Chemical Society
JSCS@tmf.bg.ac.rs • www.shd.org.rs/JSCS

J. Serb. Chem. Soc. 74 (3) 317–329 (2009) UDC 547.261'122.6–31+547.534.2:532.12/.14
JSCS–3834 *Original scientific paper*

Density, viscosity and refractive index of the dimethyl sulfoxide + *o*-xylene system

OANA CIOCIRLAN* and OLGA IULIAN

Department of Applied Physical Chemistry and Electrochemistry, Faculty of Industrial Chemistry, "Politehnica" University of Bucharest,313 Splaiul Independentei, 060042, Romania

(Received 10 April, revised 17 September 2008)

Abstract: This work reports the experimental results of the densities, viscosities and refractive indices between 298.15 and 323.15 K of the dimethyl sulfoxide + + *o*-xylene system over the entire composition range of the mixtures. The excess molar volumes (V^E), viscosity deviations ($\Delta\nu$), excess Gibbs energy of activation of viscous flow (G^{*E}) and deviations in the refraction (ΔR) were calculated from the experimental data; all the computed quantities were fitted to the Redlich–Kister equation. The system exhibits moderate negative values for the investigated excess properties. The resulting excess functions were interpreted in structural and interactional terms. From the experimental data, the thermodynamic functions of the activation of viscous flow were estimated. The viscosity data were correlated with several semi-empirical equations. The two-parameter McAllister equation can give very good results.

Keywords: dimethyl sulfoxide; *o*-xylene; density; viscosity; excess properties.

INTRODUCTION

Thermodynamic and physical properties data have a well recognized importance in design calculations involving chemical separations, fluid flow and heat transfer. Studies on the volumetric and transport properties of binary liquid mixtures provide information on the nature of the interactions between the constituents.

The present work is a continuation of our systematic experimental studies on the physic–chemical properties of binary mixtures of dimethyl sulfoxide with xylenes. The effects of molecular size and geometrical fitting of the molecules on the volumetric and viscometric properties of binary mixture containing dimethyl sulfoxide and *p*-xylene were reported earlier.[1]

This work reports experimental data of density, viscosity and refractive index for the dimethyl sulfoxide + *o*-xylene system at temperatures 298.15, 303.15,

* Corresponding author. E-mail: ciocirlan_o@yahoo.com
doi: 10.2298/JSC0903317C

313.15 and 323.15 K. The excess molar volumes, viscosity deviations, excess Gibbs energy of activation of viscous flow (G^{*E}) and deviations in refraction were calculated from the experimental data and fitted to the Redlich–Kister type polynomial equation.

The variation of the excess or deviation properties with the composition were discussed from the interactional and structural point of view. The thermodynamic functions of activation of viscous flow were estimated from the dynamic viscosity values. The viscosity data were correlated with the Grunberg–Nissan, Hind and McAllister semi-empirical equations.

Dimethyl sulfoxide (DMSO), a typical aprotic highly polar self-associated solvent (dipole moment $\mu = 1.32\times10^{-29}$ C m),[2] is an important solvent in chemistry, biotechnology, and medicine. The aromatic hydrocarbon molecules possess large quadrupole moments, causing an orientational order in these liquids.[3] The objecttive underlying the present work was to obtain information regarding molecular interactions in mixtures of a polar liquid with non-polar liquids, which is essential for an understanding of many chemical and industrial processes in these media. Moreover, the binary mixtures containing aromatic hydrocarbons are of interest as these systems find applications in studies of polymer miscibility, polymer phase diagrams, and preferential interactions in mixed solvents.[4]

The volumetric properties of binary mixtures of DMSO with *o*-xylene were studied by Ali *et al.*[5] and Wang *et al.*[6] However, no literature data on viscosities and refractive indices are available for this system.

EXPERIMENTAL

Materials

DMSO (Merck, mole fraction purity > 0.998) and *o*-xylene (Merck, mole fraction purity > 0.995) were used without further purification. The experimental density, refractive index and viscosity of the pure components are in agreement with the literature values, as can be seen in Table I.

TABLE I. Experimental and literature values for density, refractive index and viscosity of the pure components

T / K	$\rho\times10^{-3}$ / kg m^{-3}		n_D		η / mPa s	
	Lit.	Exp.	Lit.	Exp.	Lit.	Exp.
			Dimethyl sulfoxide			
298.15	1.0954[7], 1.095240[8]	1.09530	1.4770[4]	1.4778	1.991[7]	1.993
303.15	1.09045[9], 1.09049[10]	1.09027	1.4752[10]	1.4748	1.830[10]	1.811
313.15	1.08046[11]	1.08024	1.4700[10]	1.4702	1.534[10]	1.505
			o-Xylene			
298.15	0.87557[6], 0.87558[12]	0.87560	1.50295[13]	1.5020	0.758[14]	0.759
303.15	0.8714[5], 0.87136[15]	0.87131		1.4998		0.715
313.15	0.8627[5]	0.86273		1.4948		0.634

Procedure

The binary mixtures were prepared by mixing the appropriate volumes of the liquids in airtight stoppered glass bottles, which were weighed using a HR-120 (A & D Japan) electronic balance with a precision of ±0.0001 g. The experimental uncertainty in the mole fractions was estimated to be less than ±0.0002.

The density measurements of the pure solvents and the mixtures were performed by means of an Anton Paar DMA 4500 densimeter with a precision of ±0.00005 g cm^{-3}, between 298.15 and 323.15 K. The DMA cell was calibrated with dry air and ultra pure water at atmospheric pressure. The sample size was 0.70 cm^3 and the sample thermostat was controlled to ±0.01 K. Triplicate measurements of the density were performed for all the mixtures and pure components. The accuracy in the determination of the density is believed to be less than ±0.2 $kg \cdot m^{-3}$ and $\pm 10^{-8}$ $m^3 \cdot mol^{-1}$ for the calculation of V^E.

The kinematic viscosities of the pure components and their mixtures were determined at the same temperatures as for the density determinations, using an Ubbelohde capillary viscometer having a capacity of about 15 ml, a length of about 90 mm and 0.5 mm internal diameter. The viscometer was calibrated using double distilled water. At least four time flow measurements were performed for each composition and temperature, and the results were averaged. The viscometer was kept vertically in a transparent-walled bath with a thermal stability of ±0.05 K for about 30 min to attain thermal equilibrium. The uncertainty of the flow time measurement was ±0.1 s. The corresponding uncertainty in the kinematic viscosity is $\pm 0.001 \times 10^{-6}$ m^2 s^{-1}.

Refractive indices values for the D-line were measured with a thermostated Abbe refracttometer with a precision of ±0.0001. All measurements were performed in a thermostat maintained at ±0.05 K.

RESULTS AND DISCUSSION

Experimental data and excess or deviation values

The densities, ρ, kinematic viscosities, ν, and refractive indices, n_D, were measured in the temperature range from 298.15 to 323.15 K and the measured values are presented in Table II.

The values of the excess molar volume, V^E, viscosity deviation, $\Delta\nu$, deviation in molar refraction, ΔR, and the excess Gibbs energy of activation of viscous flow, G^{*E}, were calculated from the experimental data according to the following equations:

$$V^E = V - \sum_{i=1}^{2} V_i x_i \quad (1)$$

$$\Delta\nu = \nu - \sum_{i=1}^{2} \nu_i x_i \quad (2)$$

$$\Delta R_m = R_m - \sum_{i=1}^{2} R_i \varphi_i \quad (3)$$

$$G^{*E} = RT\left[\ln(V\eta) - \sum_{i=1}^{2} x_i \ln(V_i \eta_i)\right] \quad (4)$$

where x_i and φ_i represent the mole fraction and volume fraction of the pure component i, respectively; V, ν, η and R_m are the molar volume, kinematic and dynamic viscosity, and molar refraction of the mixtures, respectively, and V_i, ν_i, η_i, and R_i the corresponding properties of the pure components. The molar refraction was calculated from the Lorentz–Lorentz equation.[16] R is the gas constant and T the absolute temperature. The experimental excess properties are also reported in Table II.

TABLE II. Densities, kinematic viscosities, refractive index, excess molar volumes, viscosity deviations, excess Gibbs energy of activation for viscous flow and deviations in molar refraction for the dimethyl sulfoxide (1) + *o*-xylene (2) system from 298.15 to 323.15 K

x_1	$\rho\times10^{-3}$ kg m^{-3}	$\nu\times10^{6}$ m^2 s^{-1}	n_D	$V^E\times10^{6}$ m^3 mol^{-1}	$\Delta\nu\times10^{6}$ m^2 s^{-1}	G^{*E} kJ mol^{-1}	$\Delta R_m\times10^{6}$ m^3 mol^{-1}
			298.15 K				
0.0000	0.87560	0.8666	1.5020	0.000	0.000	0.000	0.000
0.1320	0.89390	0.9477	1.5005	–0.033	–0.045	–0.009	–0.759
0.2540	0.91281	1.0364	1.4988	–0.065	–0.072	–0.003	–1.330
0.3602	0.93100	1.1225	1.4973	–0.082	–0.087	0.005	–1.689
0.4729	0.95236	1.2229	1.4945	–0.088	–0.094	0.013	–1.964
0.5640	0.97145	1.3110	1.4923	–0.087	–0.093	0.018	–2.038
0.6602	0.99366	1.4106	1.4871	–0.078	–0.085	0.021	–1.947
0.7602	1.01934	1.5214	1.4831	–0.059	–0.070	0.020	–1.676
0.8597	1.04805	1.6390	1.4783	–0.035	–0.047	0.014	–1.200
1.0000	1.09530	1.8195	1.4778	0.000	0.000	0.000	0.000
			303.15 K				
0.0000	0.87131	0.8200	1.4998	0.000	0.000	0.000	0.000
0.1320	0.88962	0.8942	1.4979	–0.043	–0.037	–0.004	–0.782
0.2540	0.90844	0.9723	1.4963	–0.072	–0.061	–0.001	–1.342
0.3602	0.92655	1.0474	1.4944	–0.087	–0.076	0.003	–1.717
0.4729	0.94783	1.1347	1.4919	–0.092	–0.083	0.007	–1.972
0.5640	0.96686	1.2113	1.4897	–0.092	–0.083	0.009	–2.041
0.6602	0.98897	1.2982	1.4835	–0.080	–0.077	0.011	–1.983
0.7602	1.01457	1.3955	1.4804	–0.061	–0.064	0.010	–1.706
0.8597	1.04318	1.4997	1.4761	–0.036	–0.043	0.008	–1.184
1.0000	1.09027	1.6608	1.4748	0.000	0.000	0.000	0.000
			313.15 K				
0.0000	0.86273	0.7344	1.4948	0.000	0.000	0.000	0.000
0.1320	0.88097	0.7911	1.4932	–0.052	–0.030	–0.013	–0.773
0.2540	0.89966	0.8524	1.4912	–0.081	–0.049	–0.013	–1.361
0.3602	0.91763	0.9119	1.4891	–0.094	–0.060	–0.010	–1.750
0.4729	0.93876	0.9814	1.4870	–0.099	–0.065	–0.003	–1.989
0.5640	0.95764	1.0424	1.4852	–0.095	–0.064	0.002	–2.042
0.6602	0.97960	1.1113	1.4793	–0.083	–0.058	0.006	–1.979
0.7602	1.00502	1.1880	1.4762	–0.063	–0.047	0.009	–1.704
0.8597	1.03345	1.2692	1.4721	–0.037	–0.032	0.007	–1.185
1.0000	1.08024	1.3931	1.4702	0.000	0.000	0.000	0.000

TABLE II. Continued

x_1	$\rho\times10^{-3}$ kg m^{-3}	$\nu\times10^{6}$ m^2 s^{-1}	n_D	$V^E\times10^{6}$ m^3 mol^{-1}	$\Delta\nu\times10^{6}$ m^2 s^{-1}	G^{*E} kJ mol^{-1}	$\Delta R_m\times10^{6}$ m^3 mol^{-1}
			323.15 K				
0.0000	0.85410	0.6591	1.4892	0.000	0.000	0.000	0.000
0.1320	0.87226	0.7062	1.4878	–0.060	–0.023	–0.011	–0.769
0.2540	0.89081	0.7572	1.4864	–0.087	–0.037	–0.009	–1.330
0.3602	0.90866	0.8073	1.4841	–0.101	–0.044	0.000	–1.737
0.4729	0.92964	0.8656	1.4820	–0.105	–0.045	0.011	–1.983
0.5640	0.94840	0.9163	1.4800	–0.101	–0.043	0.019	–2.051
0.6602	0.97020	0.9729	1.4744	–0.087	–0.038	0.025	–1.985
0.7602	0.99546	1.0345	1.4710	–0.067	–0.030	0.026	–1.711
0.8597	1.02371	1.0983	1.4672	–0.040	–0.019	0.020	–1.212
1.0000	1.07019	1.1917	1.4659	0.000	0.000	0.000	0.000

The experimental values of V^E, $\Delta\nu$, ΔR_m and G^{*E} were fitted to the Redlich–Kister[17] type polynomials:

$$Y = x_i x_j \sum_{k=0}^{p} A_k (x_i - x_j)^k \tag{5}$$

where Y is V^E, $\Delta\nu$, ΔR_m or G^{*E} and p is the degree of polynomial expansion. The adjustable parameters A_k obtained by fitting the equations to the experimental values with a least-squares algorithm are given in Table III, along with the standard deviation, σ, defined as follows:

$$\sigma = \left[\frac{\sum_{i=1}^{n} (Y_i^{\text{exp}} - Y_i^{\text{calc}})^2}{n - m} \right]^{0.5} \tag{6}$$

where n is the number of experimental data and m is the number of parameters.

The variation of the excess or deviation properties along with the smoothed curves using Eq. (5) are presented in Figs. 1a–1d. As can be seen from the Figures, the main features of the system are that the excess molar volumes, deviations in viscosity, and deviations in molar refraction are all negative, while the excess Gibbs energy of activation of viscous flow has an S-shape allure, with positive and negative values.

The values of the excess molar volumes are moderately negative and become slightly more negative as the temperature of the mixtures increases from 298.15 to 323.15 K, with minima between –0.09 and -0.1×10^{-6} m^3 mol^{-1}.

This trend would seem to indicate: (a) a packing effect due to the geometrical fitting of the molecules of different molecular sizes into each others structure (71.30×10^{-6} for DMSO and 121.24×10^{-6} m^3 mol^{-1} for *o*-xylene at 298.15 K)

and (b) electron donor–acceptor type interactions in which the aromatic hydrocarbon behaves as electron donor.[18] A factor that would cause an increase of the V^E values (a positive effect) is the breakdown of DMSO self-association and the destruction of molecular order in the aromatic hydrocarbon on mixing, as is reflected by the positive heats of mixing reported in literature for this system.[19] All these above factors play a role in deciding the magnitude of the excess molar volumes; hence the obtained V^E values are moderately negative. As the temperature is lowered, the packing effect of the compounds is lowered; therefore V^E became less negative, as was observed by Pal and Kumar[20] for mixtures exhibiting a similar behavior.

TABLE III. The adjustable parameters and standard deviations of the excess functions of the dimethyl sulfoxide (1) + *o*-xylene (2) system

Function	A_0	A_1	A_2	A_3	σ
		298.15 K			
$V^E \times 10^6$ / m^3 mol^{-1}	–0.3600	0.0140	0.1201	–0.0141	0.0012
$\Delta\nu \times 10^6$ / m^2 s^{-1}	–0.3590	0.0378	–0.0187	–	0.0002
$\Delta R \times 10^6$ / m^3 mol^{-1}	–7.9785	1.9901	–0.5406	–	0.0097
G^{*E} / kJ mol^{-1}	0.1802	0.3288	–0.1472	0.0272	0.0004
		303.15 K			
$V^E \times 10^6$ / m^3 mol^{-1}	–0.3736	0.0232	0.0656	0.0678	0.0006
$\Delta\nu \times 10^6$ / m^2 s^{-1}	–0.3235	–0.0049	–0.0103	–	0.0001
$\Delta R \times 10^6$ / m^3 mol^{-1}	–8.0778	1.8382	–0.2766	0.8832	0.0040
G^{*E} / kJ mol^{-1}	0.0740	0.1394	–0.0518	0.0085	0.0001
		313.15 K			
$V^E \times 10^6$ / m^3 mol^{-1}	–0.3942	0.0538	0.0267	0.0941	0.0003
$\Delta\nu \times 10^6$ / m^2 s^{-1}	–0.2517	0.0151	–0.0067	–	0.0001
$\Delta R \times 10^6$ / m^3 mol^{-1}	–8.0712	2.1884	–0.5766	–	0.0082
G^{*E} / kJ mol^{-1}	0.0527	0.2216	–0.0687	0.0103	0.0002
		323.15 K			
$V^E \times 10^6$ / m^3 mol^{-1}	–0.4161	0.0632	–0.0070	0.1273	0.0006
$\Delta\nu \times 10^6$ / m^2 s^{-1}	–0.1829	0.0280	0.0028	–	0.0001
$\Delta R \times 10^6$ / m^3 mol^{-1}	–8.0967	2.0085	–0.5193	–	0.0073
G^{*E} / kJ mol^{-1}	0.0680	0.2250	–0.0039	–0.0098	0.0001

The deviations in the viscosity are moderately negative over the whole composition range at the investigated temperatures. The viscosity deviations are a function of the intermolecular interaction as well as of the size and shape of the molecules. Fort and Moore[21] state that a positive viscosity deviation is a characteristic of systems where intermolecular interactions predominate, whereas mixtures without strong interactions present a negative viscosity deviation. The obtained negative $\Delta\nu$ values for DMSO + *o*-xylene mixtures indicate weak interactions in this system. Moreover, V^E and $\Delta\nu$ do not obey the general rule, according which they should have the opposite sign (specific for systems where inter-

molecular interactions predominate), therefore, for this system, the geometrical fitting of the molecules prevails.

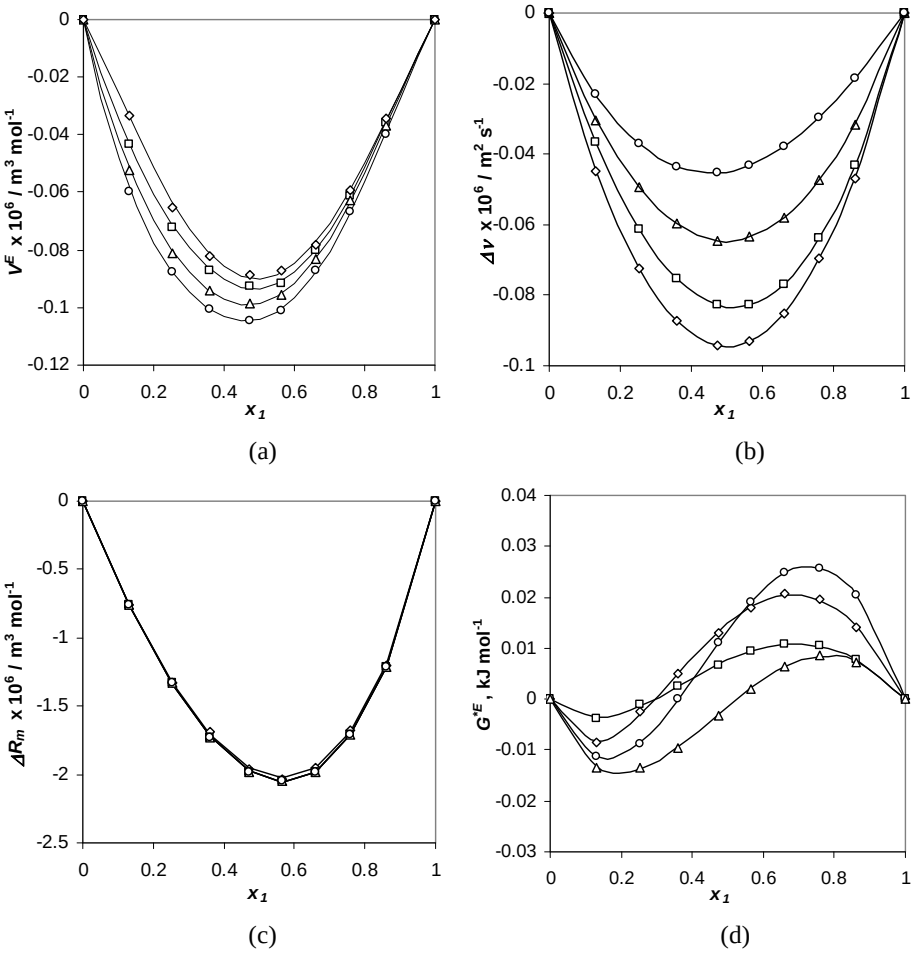

Fig. 1. Excess molar volumes (a), viscosity deviations (b), deviations in molar refraction (c) and excess Gibbs energy of activation of viscous flow (d) for the dimethyl sulfoxide (1) + + *o*-xylene (2) system at 298.15 (◊); 303.15 K (□); 313.15 K (Δ); 323.15 K (○); correlation with the Redlich–Kister equation (—).

An increase of temperature diminishes the interactions in the pure components and also the interactions between unlike molecules, because of the increase in the thermal energy. This leads to less negative values of $\Delta\nu$ with increasing temperature, as was observed in the present study.

The V^E values at 303.15 K compare well with the reported results of Wang *et al.*[6] using the same experimental method, as is reflected in Fig. 2. There are no literature data with which to compare the values of $\Delta\nu$.

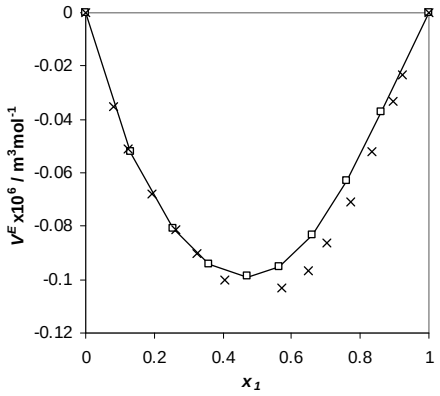

Fig. 2. Comparison of the excess molar volumes for the dimethyl sulfoxide (1) + *o*-xylene (2) system at 313.15 K: present data – □; Ref. 6 – ×; correlation with the Redlich–Kister equation: —.

The deviations in molar refraction are negative for the whole composition range for all mixtures. The values are independent of temperature, according to the theory, the molar refraction depending only on the wavelength of light used for the measurement.

From the viscosity and density data, the excess free energy of activation for viscous flow was calculated. The G^{*E} dependence with the mole fraction of DMSO and temperature is shown in Fig. 1d. For all the studied temperatures, the G^{*E} values vary from slightly negative in the *o*-xylene rich region to slightly positive with increasing DMSO mole fraction. Only a slight influence of temperature on the excess free energy of activation was observed. As suggested by other authors,[22–23] a large negative excess in G^{*E} indicates the presence of weak interactions, whereas a large positive excess in G^{*E} suggests a specific association between the molecules in the solvent mixture. Due to the small obtained G^{*E} values (about ±0.02 kJ mol^{-1}) for this system, it is difficult to explain the variation of G^{*E} with composition. For this purpose, non-thermodynamic information concerning the structure of the mixtures would be necessary.

A similar behavior, namely negative excess molar volumes, negative deviations in viscosity, negative deviations in molar refractivity and the same variation with temperature of the excess functions, was found in the case of the DMSO + *p*-xylene system, which was presented in a previous paper.[1]

Thermodynamic functions of activation

The thermodynamic functions of activation for viscous flow were evaluated from the dynamic viscosity values of the binary mixtures considering the Eyring transition state theory. The absolute rate approach of Eyring provides the following expression for the viscosity of a liquid mixture:[24–26]

$$\eta = \frac{h N_A}{V} \exp\left(\frac{\Delta G^*}{RT}\right) \quad (7)$$

where h is the Planck constant, N_A is Avogadro constant and ΔG^* is the molar Gibbs energy change of activation for the viscous flow process. Combining with:

$$\Delta G^* = \Delta H^* - T\Delta S^* \quad (8)$$

yields the equation:

$$\ln\left(\frac{\eta V}{h N_A}\right) = \frac{\Delta H^*}{RT} - \frac{\Delta S^*}{R} \quad (9)$$

From the experimental density and viscosity data, plots of $\ln(\eta V/hN_A)$ against $1/T$ give a straight line for each mixture and the enthalpy and entropy changes of activation of viscous flow can be estimated from its slope and intercept, respectively. The ΔH^* values are constant in the studied temperature range. The obtained thermodynamic functions of activation at 298.15 K are pre-

TABLE IV. The thermodynamic functions of the activation of viscous flow, ΔH^*, ΔS^* and ΔG^*, for the dimethyl sulfoxide (1) + *o*-xylene (2) system at 298.15 K

x_1	ΔH^* / kJ mol^{-1}	$-\Delta S^*$ / J mol^{-1} K^{-1}	ΔG^* / kJ mol^{-1}
0.0000	8.78	54.10	–7.35
0.1320	9.47	52.22	–6.10
0.2540	10.11	50.54	–4.96
0.3602	10.61	49.27	–4.08
0.4729	11.11	48.01	–3.20
0.5640	11.51	47.01	–2.51
0.6602	11.93	45.95	–1.77
0.7602	12.38	44.80	–0.98
0.8597	12.85	43.56	–0.14
1.0000	13.59	41.55	1.20

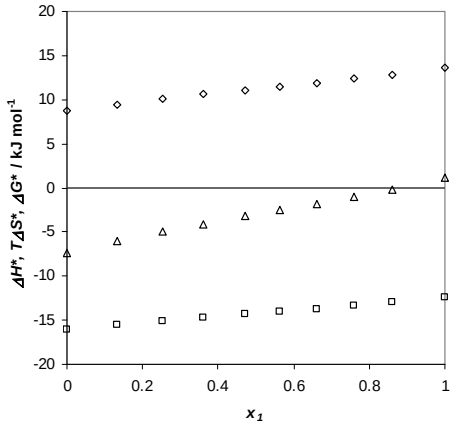

Fig. 3. Thermodynamic functions of activation *vs.* composition for the dimethyl sulfoxide (1) + *o*-xylene (2) system at 298.15 K; ΔH^* (◊); $T\Delta S^*$ (□); ΔG^* (Δ).

sented in Table IV. The contributions of enthalpy and entropy changes to the Gibbs energy change of activation of viscous flow for dimethyl sulfoxide + *o*-xylene mixtures are shown in Fig. 3 at 298.15 K; they increase with increasing concentration of DMSO in the mixture. The same behavior was observed at all investigated temperatures. The values of ΔH^* are positive and of ΔS^* negative, indicating that the attainment of the transition state for viscous flow is accompanied by bond breaking. The entropy change of activation from the initial state to the transition at a given composition is significant during an activated viscous flow process; therefore this process is entropy-controlled for DMSO + *o*-xylene mixtures. It seems that for the viscous flow process, the structural factor dominates over the interactional one, as in the case of the mixing properties.

The viscosity data correlation

Several semi-empirical relations have been proposed to estimate the viscosity of liquid mixtures, in terms of pure component data. In the present work, the experimental viscosity data of the binary DMSO + *o*-xylene system at 298.15, 303.15, 313.15 and 323.15 K were fitted to the Grunberg–Nissan,[27] Hind[28] and McAllister[29] equations. According to Grunberg and Nissan, the adjustable binary parameter mentioned in Eq. (10) is regarded as a measure of the strength of the interactions between the mixing species. The single parameter correlation of Grunberg–Nissan and Hind equations are:

$$\ln \eta = \sum_{i}^{2} x_i \ln \eta_i + \sum_{i}^{2} \sum_{j>i}^{2} x_i x_j A_{ij} \tag{10}$$

$$\eta = \sum_{i}^{2} x_i^2 \eta_i + \sum_{i}^{2} \sum_{j>i}^{2} x_i x_j A_{ij} \tag{11}$$

where A_{ij} is the interaction parameter.

The McAllister two-parameter equation, based on the Eyring theory of absolute reaction rates, takes into account interactions of both like and unlike molecules by a two-dimensional three-body interaction. This model is recommended for systems where the volumetric size ratio of the components is less than 1.5:

$$\ln \nu = \sum_{i=1}^{n} x_i^3 \ln \left(\nu_i M_i\right) - \ln \sum_{i=1}^{n} x_i M_i + 3 \sum_{i=1}^{n} \sum_{\substack{j=1 \\ j \neq i}}^{n} x_i^2 x_j \ln A_{ij} M_{ij} \tag{12}$$

$$M_{ij} = \frac{2M_i + M_j}{3} \tag{13}$$

where A_{ij} are the interaction parameters and M_i is the molar mass of the components. For all these models, the standard deviation, σ, was calculated using a type (6) equation.

The correlation parameters along with the average percentage deviation:

$$Dev = \frac{100}{n}\sum_{i=1}^{n}\frac{\left|\eta_i^{\exp} - \eta_i^{\text{calc}}\right|}{\eta_i^{\exp}} \quad (14)$$

and the standard deviation for the binary DMSO + *o*-xylene system at each temperature are listed in Table V.

TABLE V. Correlation deviations and adjustable parameters of the viscosity Equations for the dimethyl sulfoxide (1) + *o*-xylene (2) system

T / K	Grunberg–Nissan			Hind			McAllister			
	A_{ij}	σ mPa s	*Dev* %	A_{ij}	σ mPa s	*Dev* %	A_{ij}	A_{ji}	$\sigma\times10^6$ m^2 s^{-1}	*Dev* %
298.15	–0.1120	0.0020	0.14	1.0114	0.0093	0.60	1.4373	1.0896	0.0009	0.06
303.15	–0.1251	0.0005	0.04	0.9391	0.0099	0.70	1.3139	1.0227	0.0003	0.02
313.15	–0.1378	0.0013	0.11	0.8146	0.0065	0.53	1.1280	0.8860	0.0004	0.03
323.15	–0.1126	0.0024	0.24	0.7260	0.0030	0.28	0.9957	0.7823	0.0003	0.03

The analysis showed that all the equations present small deviations, less than 1 %. The theoretically based McAllister equation gives very good results, with deviations from 0.02 to 0.06 %, even though the components have different molar volumes (molar volume ratio is 1.7). The values of the Grunberg–Nissan interaction parameter are negative for this system, which suggest weak interactions between unlike molecules, which is in accordance with the excess properties analysis.

CONCLUSIONS

Experimental data of the densities, kinematic viscosities and refractive indices for the binary system DMSO + *o*-xylene at 298.15, 303.15, 313.15 and 323.15 K are reported. The calculated excess molar volumes, viscosity deviations, excess Gibbs energy of activation of viscous flow and deviations in refraction were fitted to the Redlich–Kister equation. The excess molar volumes, deviations in viscosity and deviations in molar refraction are all negative, while the excess Gibbs energy of activation of viscous flow has an S-shape allure, with positive and negative values. The temperature has a significant effect on $\Delta\nu$ and a relatively slight effect on V^{E}, ΔR_{m} and $G^{*\text{E}}$.

The moderate negative excess molar volumes and negative $\Delta\nu$ values suggest that the geometrical fitting of the molecules is more important than the interactional factor for this system. The thermodynamic functions of activation for the viscous flow process indicate that this process is entropy-controlled. The Grunberg–Nissan, Hind and McAllister equations are suitable for estimating the mixing viscosities in terms of the pure component data.

NOMENCLATURE

A_k – Redlich–Kister parameters

A_{ij} – Interaction parameters
Dev – Average percentage deviation
G^{*E} – Excess Gibbs energy of activation of viscous flow
ΔG^* – Gibbs energy change of activation of viscous flow
h – Planck constant
ΔH^* – Enthalpy change of activation of viscous flow
m – Number of model parameters
M_i – Molar mass of the i-th pure component
n – Number of experimental points
N_A – Avogadro constant
n_D – Refractive index
ΔR_m – Deviation in molar refraction
R_m – Molar refraction of mixture
R_i – Molar refraction of the *i*-th pure component
R – The gas constant
ΔS^* – Entropy change of activation of viscous flow
T – Absolute temperature
V^E – Excess molar volume
V – Molar volume of mixture
V_i – Molar volume of the *i*-th pure component
x_i – Liquid-phase mole fractions

Greek letters

μ – Dipole moment
η, ν – Dynamic and kinematic viscosity of the mixture, respectively
η_i, ν_i – Dynamic and kinematic viscosity of the *i*-th pure component
$\Delta\nu$ – Viscosity deviation
ρ – Density
σ – Standard deviation
φ_i – Volume fraction.

И З В О Д

ГУСТИНА, ВИСКОЗНОСТ И ИНДЕКС РЕФРАКЦИЈЕ СИСТЕМА ДИМЕТИЛ СУЛФОКСИД + *o*-КСИЛЕН

OANA CIOCIRLAN и OLGA IULIAN

Department of Applied Physical Chemistry and Electrochemistry, Faculty of Industrial Chemistry, "Politehnica" University of Bucharest,313 Splaiul Independentei, 060042, Romania

У раду су приказани експериментални подаци за густине, вискозности и индексе рефракције на температурама од 298,15 до 323,15 K система диметил сулфоксид + *o*-ксилен за комплетан опсег састава смеше. Вишак моларне завремине, одступање вискозности, вишак Gibbs-ове енергије вискозног течења и одсупање индекса рефракције израчунати су на основу експерименталних података; израчунате вредности фитоване су Redlich–Kister једначином. Систем показује умерено негативно одступање вишкова испитиваних величина. Резултујуће функције вишкова тумачене су са становишта структурних промена и интеракције компоненти. На основу експериметалних података одређене су термодинамичке функције за активацију вискозног течења. Подаци за вискозност корелисани су са неколико полуемиријских једначина. Двопараметарска McAllister једначина може да да веома добра слагања.

(Примљено 10. априла, ревидирано 17. септембра 2008)

REFERENCES

1. O. Ciocirlan, O. Iulian, *J. Serb. Chem. Soc*. **73** (2008) 73
2. J. A. Dean, *Lange's Handbook of Chemistry*, McGraw-Hill, New York, 1956
3. D. Patterson, *J. Solution Chem*. **23** (1994) 105
4. M. I. Aralaguppi, T. M. Aminabhavi, S. B. Harogoppad, R. H. Balundgi, *J. Chem. Eng. Data* **37** (1992) 298
5. A. Ali, A. K. Nain, D. Chand, R. Ahmad, *Bull. Chem. Soc. Jpn.* **79** (2006) 702
6. H. Wang, W. Liu, J. Huang, *J. Chem. Thermodyn*. **36** (2004) 743
7. J. A. Riddick, W. B. Bunger, T. K. Sakano, *Techniques of Chemistry. Vol. II, Organic Solvents*, 4th Ed., Wiley, 1986
8. R. D. Peralta, R. Infante, G. Cortez, J. Wisniak, *J. Solution Chem.* **34** (2004) 515
9. K. Rubini, R. Francesconi, A. Bigi, F. Comelli, *Thermochim. Acta* **452** (2007) 124
10. N. G. Tsierkezos, A. E. Kelarakis, M. A. Palaiologou, *J. Chem. Eng. Data* **45** (2000) 395
11. D. J. Pruett, L. K. Felker, *J. Chem. Eng. Data* **30** (1985) 452
12. L. Serrano, J. A. Silva, F. Farelo, *J. Chem. Eng. Data* **35** (1990) 288
13. T. E. Daubert, R. P. Danner, *Technical data book-petroleum refining*, 5th Ed., American Petroleum Institute, Washington, D.C., 1992-extant, in: DIPPR AIChE, 2005
14. M. Georgios, R. Christos, R. George, *J. Chem. Eng. Data* **44** (1999) 1187
15. C. Yang, P. Ma, Q. Yhou, *J. Chem. Eng. Data* **49** (2004) 881
16. H. A Lorentz, *Theory of electrons*, Teubner, Leipzig, Germany, 1909
17. O. Redlich, A. T. Kister, *Ind. Eng. Chem*. **40** (1948) 345
18. D. V. Fenby, G. B. Billing, D. B. Smythe, *J. Chem. Thermodyn.* **5** (1973) 49
19. E. I. Shcherbina, A. E. Tenenbaum, L. L. Gurarii, *Russ. J. Phys. Chem*. **49** (1975) 450
20. A. Pal, H. Kumar, *Fluid Phase Equilib.***181** (2001) 17
21. R. Fort, W. R. Moore, *Trans. Faraday Soc*. **62** (1966) 1112
22. B. Sathyanarayana, B. Ranjithkumar, T. S. Jyostna, N. Sathyanarayana, *J. Chem. Thermodyn.* **39** (2007) 16
23. A. S. Al-Jimaz, J. A. Al-Kandary, A.-H. Al-Latif, *Fluid Phase Equilib*. **218** (2004) 247
24. H. Eyring, M. S. John, *Significant Liquid Structure*, Wiley, New York, 1969
25. R. J. Martins, M. J. E. de M. Cardoso, O. E. Barcia, *Ind. Eng. Chem. Res*. **39** (2000) 849
26. A. Ali, A. K. Nain, S. Hyder, *J. Indian Chem. Soc.* **75** (1998) 501
27. L. Grunberg, A. H. Nissan, *Nature* **164** (1949) 799
28. R. K. Hind, E. McLaughlin, A. R. Ubbelohde, *Trans. Faraday Soc*. **56** (1960) 328
29. R. A. McAllister, *AIChE J*. **6** (1960) 427.

Journal of the Serbian Chemical Society
JSCS@tmf.bg.ac.rs • www.shd.org.rs/JSCS

J. Serb. Chem. Soc. 74 (3) 331–347 (2009)
JSCS–3835

UDC 666.942:620.193:546.226:519.87
Original scientific paper

$(NH_4)_2SO_4$ corrosion of cement in concrete analyzed by an improved mathematical model

SAŠA MILETIĆ[1]*, MIRJANA DJURIĆ[2], ANDJELKA MIHAJLOV[3], DJORDJE BAŠIĆ[3] and DJORDJE JANAĆKOVIĆ[4#]

[1]*Galenika Fitofarmacija, Batajnički drum b.b., 11080 Zemun,* [2]*Faculty of Technology, University of Novi Sad, 21000 Novi Sad, Bul. Cara Lazara 1,* [3]*Faculty of Technical Sciences, University of Novi Sad, 21000 Novi Sad, Trg Dositeja Obradovića 6 and* [4]*Faculty of Technology and Metallurgy, University of Belgrade, 11000 Belgrade, Karnegijeva 4, Serbia*

(Received 18 July, revised 21 October 2008)

Abstract: This paper gives a critical analysis of the equation that predicts and estimates the progress of degradation for various building materials, recently proposed by Matsufuji *et al.*[1] After the analysis, the paper suggests an improved mathematical model, particularly for the modeling of sulfate corrosion. Experiments were performed with two samples of Portland cement and two samples of Portland cement with 30 % coal ash. The samples were immersed into a 10 % $(NH_4)_2SO_4$ solution and the concentration of SO_4^{2-} in the solution and the material was measured. As a parameter that quantifies cement degradation, the quantity of bonded SO_4^{2-} was suggested. According to the obtained data, mathematical models for the description of sulfate corrosion were defined for all the examined samples. The models were applied for the analysis of the behavior of ash and non-ash containing samples. They allowed a better explanation of degradation which occurred during the investigated time period and even further they showed that ash systems were significantly more resistant to sulfate corrosion.

Keywords: sulfate; corrosion; Portland cement; coal fly ash; mathematical model.

INTRODUCTION

Degradation of concrete is a serious problem mostly caused by various parallel and/or consecutive chemical reactions and related physical changes. The term sulfate corrosion means the effect of aggressive SO_4^{2-} from the environment on the concrete. The response of a concrete on this aggression depends on its composition and structure. A certain number of different compounds might appear as products (such as gypsum or its anhydrite, ettringite, calcium silicate sul-

* Corresponding author. E-mail: miletic@fitofarmacija.rs
# Serbian Chemical Society member.
doi: 10.2298/JSC0903331M

fate carbonate hydrate – thaumasite, *etc*.) which are undesirable for various reasons.[2–5] They can provoke further chemical reactions and/or undergo dissolution, thus promoting degradation. The newly formed compounds can also change the volume of the system. This causes the appearance of smaller or larger cracks, due to the generated deformation stresses.

On the other hand, a description of the degradation processes by an adequate mathematical model provides a useful tool for investigating the phenomenon.[6] Mathematical models enable a kind of generalization when they are applied to analogous systems. Once defined, a mathematical model can be used for numerical simulations of the response of a material to variable environmental conditions. The results of such a simulation can also be used for an optimization. For example, the quantities of a particular raw material which should be used (in the case of products obtained by blending) might be suggested in order to obtain products with desired features.

The formulation of rigorous mathematical models requires accurate knowledge of the mechanisms of deterioration, which is not always the case. Various assumptions, simplifications and idealizations very often have to be accepted, which leads to approximate models. Typical examples are models defined by statistical processing of measured data. The necessary source of information is an experiment which simulates the degradation.[7,8] Quantification of the degradation processes are obtained by employing numerous experimental techniques and methods. In the case of sulfate corrosion, the classical method of chemical analysis is suggested for determining the concentration of SO_4^{2-} in the solution. The methods for characterization of the final products are also suitable. For example, a method for measuring flexural strength, when comparatively applied to corroded and uncorroded samples, can give essential information.

This paper gives a contribution to mathematical modeling of sulfate corrosion of cements and also analyses the behavior of four chosen samples by applying the suggested model.

THEORY

Model of Matsufuji, Koyama and Harada[1]

Matsufuji *et al.*[1] recently proposed an equation that predicts and estimates the progress of degradation for various building materials. They assumed that the degradation commences at the surfaces in contact with the environment, whereby the environmental factors (p_f) permeate and otherwise affect the material. Therefore, the surface of the system is covered with the deteriorating parts – the products of degradation, as presented in Fig. 1.

The surface between the deteriorated and the defect-free internal parts is exposed to the influence of both environmental factors at the outer surface (p_0) and the characteristics of the deteriorated parts between p_0 and p_f:

$$p_f = p_0 + f(A,D(t)) \quad (1)$$

where $f(A,D(t))$ is a function of the two variables; A is a property of the deteriorated part and $D(t)$ is the degree of degradation.

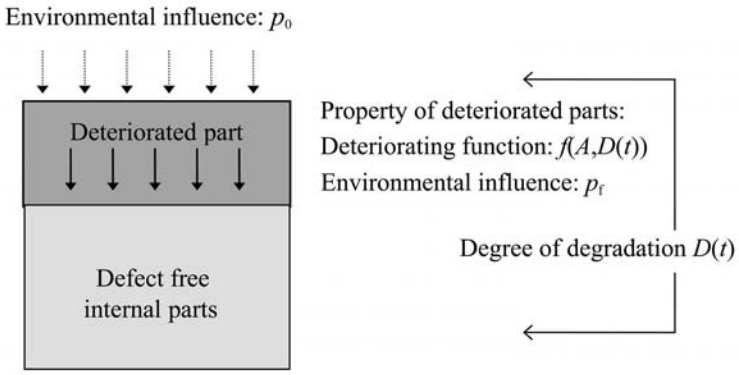

Fig. 1. Progress of degradation and relevant factors.

It can be assumed that the rate of degradation, $dD(t)/dt$, is proportional to p_f:

$$\frac{dD(t)}{dt} = kp_f = k[p_0 + f(A,D(t))] = b + aD(t) \quad (2)$$

This is a general kinetic model with constants a and b. They represent the influence of the deteriorated parts (a) and the influence of the environment itself (b). The model is easy to solve analytically, thus the following solutions can be obtained:

$$\frac{dD(t)}{dt} = b + aD(t) \Rightarrow \begin{cases} a = 0 & D(t) = bt \\ a \neq 0 & D(t) = \dfrac{b}{a}(\exp(at) - 1) \end{cases} \quad (3)$$

In accordance with the Solutions (3), the deterioration of all building materials can be classified into three patterns (as presented in Fig. 2):

The alignment type ($a = 0$) has a deterioration rate that does not depend on the current status of degradation and therefore is the simplest model for estimation. As an example, deterioration of floor concrete subjected to impact loads can be taken.

The convergence type ($a < 0$) has a gradually falling deterioration rate, due to the preserving influence of the layers of deteriorated material. In this type, the rate of degradation increases at the beginning and tends to zero at the end. The convergence type of degradation is typical of carbonation and deformation of concrete.

The multiplication type ($a > 0$) is an accelerated type of degradation for the deteriorated parts accelerates the further degradation. Hence, as the degradation

progresses, the higher the rate becomes. Deterioration of concrete by freezing can be taken as an example.

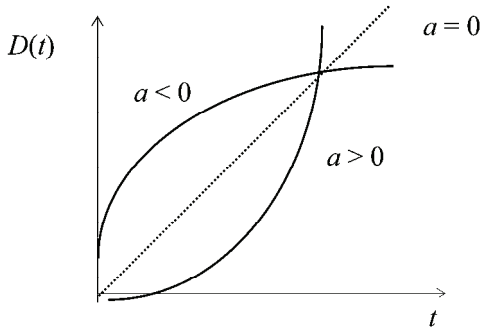

Fig. 2. Three types of deterioration.[8]

Modification of the Matsufuji model

The Matsufuji and co-authors model seems to be rather idealized. There are at least two highly questionable assumptions which were accepted by the authors: *i*) the environmental factors have a constant intensity and *ii*) the characteristics of the deteriorated parts are time independent. Neither of the assumptions is correct with regards to the degradation caused by atmospheric influence. Therefore, the Matsufuji model has to be modified in a following way:

$$\frac{\mathrm{d}D(t)}{\mathrm{d}t} = b(t) + a(t)D(t) \tag{4}$$

Obviously, the parameters (a and b) of the original equation have to be replaced by the time functions ($a(t)$ and $b(t)$), which have to be defined for each particular case.

Mathematical modeling of sulfate corrosion

Modified model (4) will be applied to the modeling of sulfate corrosion on several cement samples and the best possible $a(t)$ and $b(t)$ functions (derived from the experimental data) will be found. Such a modified model will be used for a comparative analysis of the degradation processes of the investigated samples.

The procedure for determining the modified model is given below:

1) the experimental data concerning the change in concentration of the SO_4^{2-} in the surrounding solution should be used for defining the mathematical model of the solution behavior (y_b). This can be realized by applying the regression analysis method, which means choosing an adequate type of correlation and defining the parameters of the correlation.

The type of correlation (where the independent variable is time) could be a polynomial of adequate order, such as:

$$y_b = b_1 + b_2 t + b_3 t^2 + \ldots \tag{5}$$

or, very often, some of exponential decay functions, such as:

$$y_b = b_1 + b_2 \exp\left(\frac{-t}{b_3}\right) + b_4 \exp\left(\frac{-t}{b_5}\right) + \ldots \quad (6)$$

After choosing the type of correlation, their parameters (b_i, i = 1,n) should be determined by processing the experimental data.

2) Now, the time dependent parameter ($b(t)$) of the modified differential equation can be defined. It is proportional to the function, y_b:

$$b(t) = k y_b \quad (7)$$

where k is a constant. In this way, the influence of the immediate environment on the samples immersed in the aggressive solution is mathematically described.

3) The third step in the mathematical modeling of sulfate corrosion is the determination of k and a (a_i, i = 1,n) parameters in the model:

$$\frac{\mathrm{d}D(t)}{\mathrm{d}t} \approx \frac{\Delta D}{\Delta t} = k y_b + (a_1 + a_2 t + a_3 t^2 + \ldots) D(t) \quad (8)$$

using experimental data. As the experimental data, the degrees of degradation are taken. In a sulfate corrosion problem, the degradation degree is expressed as the concentration of SO_4^{2-} reacting with the material. The derivatives ($\mathrm{d}D/\mathrm{d}t$) must be determined numerically using the mentioned database and the time increments in accordance with the experiments.

Unfortunately, Eq. (4) is difficult to solve analytically even in the cases when the $a(t)$ and $b(t)$ functions are extremely simple, hence a numerical procedure particularly oriented to solving the sulfate corrosion problem will be suggested.

Database obtained by measurements and calculations

It is obvious that the data necessary for deriving a sulfate corrosion model are: *i*) the concentrations of SO_4^{2-} in the environment and *ii*) the concentrations of the SO_4^{2-} spent by the chemical reactions occurring inside the material. Actually, the quantities of the reacted SO_4^{2-} are equal to the concentration differences for the solution in particular time increments. The changes of the other product characteristics due to sulfate corrosion can also be tracked. Here, weight loss and the decrease in flexural strength were chosen. Therefore, the experiments were planned to give the necessary information.

EXPERIMENTAL

The investigated samples were as follows:
– Portland cement 1 (PC1),
– Portland cement 1 with 30 % coal ash (PAC1) added,
– Portland cement 2 (PC2) and
– Portland cement 2 with 30 % coal ash (PAC2) added.

The cements were made from two clinkers; the potential phase compositions of which (calculated by ASTM C 150) are presented in Table I.[7] It can be seen that the content of the C_3A compound was two times lower in clinker 2 than in the clinker 1. It is also well known that the hydrates of this compound react easily with SO_4^{2-} giving expansive compounds. The difference in the content of C_3S was also significant.

TABLE I. Phase composition (mass %) of Portland cement clinker

Compound	Portland cement clinker	
	1	2
C_3S	57.54	66.98
C_2S	13.50	12.72
C_3A	13.31	6.60
C_4AF	8.67	9.10

The chemical compositions of the pure cements, blended cements and the coal ash (determined applying the European standard method EN 196-2) are shown in Table II.[7] As can be seen, the coal ash had high contents of SiO_2, Al_2O_3 and Fe_2O_3 oxides and low contents of CaO, MgO, sulfate and alkali oxides. The loss of ignition was rather high. XRD Analysis showed that the ash was mostly amorphous but quartz, feldspar and hematite were present as crystalline phases. With regards to the chemical composition of the cements with mineral admixture, an increased content of insoluble residue as well as a higher loss of ignition could be noticed. The content of free CaO diminished after addition of the ash. Cements PC2 and PAC2 had low contents of sulfate and MgO.

TABLE II. Chemical composition (mass %) of the cement and coal ash

Compound	Cement				Ash
	PC1	PC2	PAC1	PAC2	
SiO_2	19.7	21.0	14.0	15.6	50.8
Al_2O_3	6.95	5.33	6.23	4.88	21.6
Fe_2O_3	2.71	2.92	2.67	2.85	11.6
CaO	62.0	63.8	44.7	47.5	6.52
Insoluble residue	0.10	0.11	20.2	18.7	76.6
LOI	0.84	0.69	3.03	2.89	5.68
CaO free	0.12	0.35	–	–	–
CaO in $CaCO_3$	0.51	0.45	0.55	0.55	–
CaO in $CaSO_4$	1.40	1.18	1.41	1.08	–
SO_3 in $CaSO_4$	2.00	1.69	2.02	1.54	–
SO_3	–	–	–	–	0.05
S	–	–	–	–	0.02
MgO	2.22	1.41	2.43	1.21	2.65
Alkalis as Na_2O	0.41	0.33	0.38	0.35	0.30
K_2O	0.40	0.33	0.22	0.30	0.70

The sieve residue (European standard EN 196-6), density, specific surface area (European standard EN 196-6), setting time (European standard EN 196-3) and other physico–chemical properties were determined and are presented in Table III.[7] The addition of ash caused an increase of the following quantities: sieve residue (due to the fineness of the ash itself), spe-

cific surface area and the water demand for a standard consistency. On the other hand, other characteristics of the cements did not change. It should also be emphasized that all the quantities given in Tables II and III are in compliance with the Yugoslav standard JUS B.C1.011.

TABLE III. Physico–chemical properties of the cements

Physico–chemical property	Cement			
	PC1	PC2	PAC1	PAC2
Sieve residue at 0.09 mm sieve, mass %	1.80	2.60	5.20	6.00
Density, g/cm^3	3.14	3.17	2.88	2.85
Specific surface area (after Blain), cm^2/g	3320	3100	3720	3710
Standard consistence, mass %	25.8	23.8	28	27.5
Initial time, min	165	165	240	255
Final time, min	225	225	330	360
Le Chatelier test, mm	1.0	1.5	1.0	1.0

Also, flexural and compressive strengths of the cements (European standard EN 196-1) were obtained as given in Table IV.[8] The addition of ash did not significantly change the strengths during the first four weeks.

TABLE IV. Strengths (MPa) of the cements

Strength	*t* / days	Cement			
		PC1	PC2	PAC1	PAC2
Flexural	2	4.4	3.7	2.5	2.1
	3	5.3	4.4	3.6	2.9
	7	7.2	7.4	6.2	4.7
	28	8.0	8.9	8.3	8.4
Compressive	2	15.7	13.2	8.8	7.4
	3	19.8	16.0	14.9	10.4
	7	30.2	32.8	24.2	19.4
	28	40.3	50.9	39.5	44.9

The sulfate corrosion of the cements was investigated according to the Koch–Steinegger method.[6,8] Mortar prisms of the samples were prepared from the standard sand of the former German cement standard DIN 1164 (1958), with a water/cement ratio 0.6. Before the prisms were exposed to the aggressive solutions, they were cured for 1 day in the mould and for 20 days in water. Instead of the 4.4 % Na_2SO_4 solution, suggested in the original Koch–Steinegger method, a 10 % $(NH_4)_2SO_4$ solution was used. This provided intensive aggression and enabled successful simulation of the real conditions typical for a polluted environment. The samples were immersed into the aggressive solution for 9 month. Simultaneously, the same number of samples was stored in distilled water for possible comparisons.

Measurements of the mass and flexural strength of the corroded samples, as well as the samples exposed to water, were performed after 7, 14, 28, 56, 90, 180 and 270 days. Also, the concentration of SO_4^{2-} in the solution was determined.

Quantification of sulfate corrosion

The following parameters that quantify cement degradation are suggested: *i*) bonded SO_4^{2-}, *ii*) mass change and *iii*) a degradation factor based on changes in the flexural strength, as given by the Eqs. (9)–(11):

$$(SO_4^{2-})_{\text{bonded}} = (SO_{4\ \text{initial}}^{2-} - SO_{4\ \text{actual}}^{2-})_{\text{in solution}} \quad (9)$$

$$\Delta m = 100\frac{m_{\text{initial}} - m_{\text{actual}}}{m_{\text{initial}}} \quad (10)$$

$$DFlex[1] = 1 - \frac{\text{Flexural strength of corroded sample}}{\text{Flexural strength of uncorroded sample}} \quad (11)$$

The parameters defined by Eqs. (9)–(11) were calculated by applying the measured values. They are presented in Figs. 3–5.

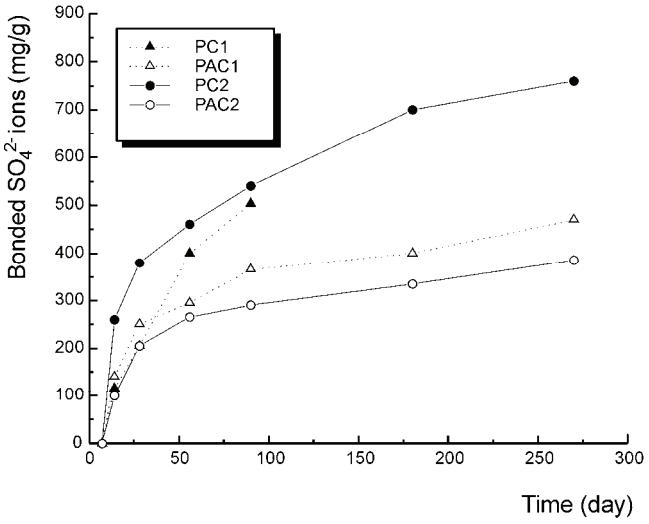

Fig. 3. Experimental curves for bounded SO_4^{2-}.

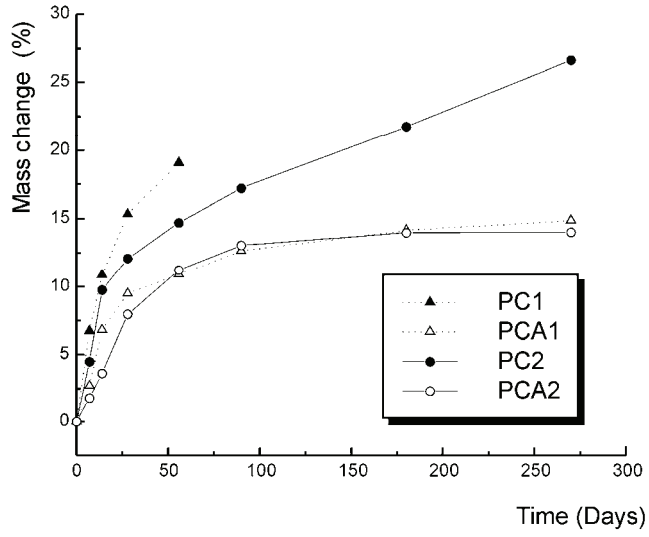

Fig. 4. Experimental mass change curves.

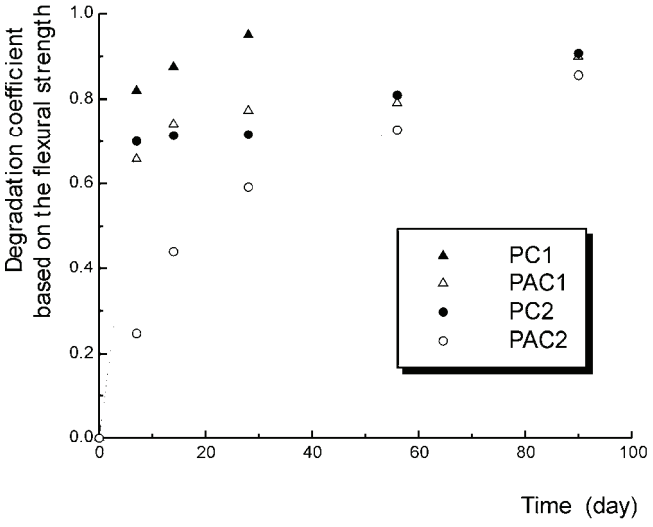

Fig. 5. Experimental coefficients of degradation curves.

RESULTS

Mathematical models of sulfate corrosion of the examined systems

According to the algorithm suggested in this paper, sulfate corrosion of the examined samples was mathematically described. While applying the derived model, interesting facts were noticed. They concern the corrosion caused by the variable influence of the atmosphere and the already degraded material.

The mathematical model was defined in following steps:

1) By applying the regression analysis method on the experimental data, *i.e.*, the concentrations of SO_4^{2-} in the solution, the behavior of the solutions in contact with four samples (PC1, PC2, PAC1 and PAC2) was mathematically described.

The decrease of SO_4^{2-} concentration in the solution surrounding PC1 samples is described quite adequately by the polynomial:

$$(y_b)_{PC1} = 1126.6 - 11.51t + 0.0583t^2 \quad (12)$$

which is graphically presented in Fig. 6.

As for other three groups of samples (PC2, PAC1 and PAC2), two decay times exponential functions proved suitable. In the case of the sample PCA1, it has the following form:

$$(y_b)_{PAC1} = 450 + 420\exp\left(\frac{-t}{10}\right) + 350\exp\left(\frac{-t}{275.94}\right) \quad (13)$$

The function given by Eq. (13) is graphically presented in Fig. 6 as dotted line.

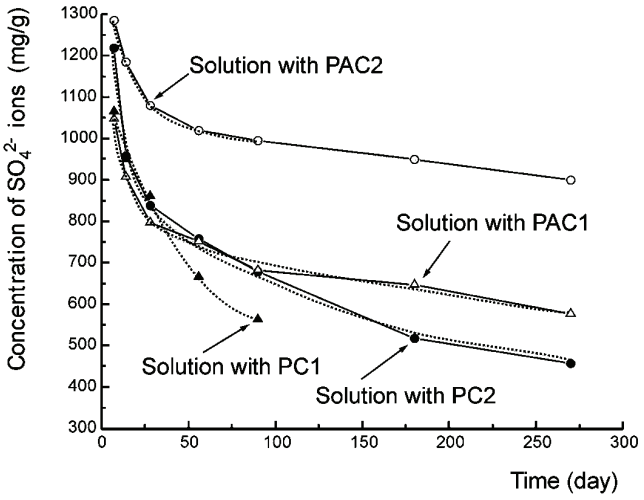

Fig. 6. Decrease of SO_4^{2-} concentration in the solutions.

The mathematical models describing the behavior of the solutions in contact with the samples PC2 and PAC2 are given by the functions:

$$(y_b)_{PC2} = 370 + 1340\exp\left(\frac{-t}{4.7}\right) + 575\exp\left(\frac{-t}{140.2}\right) \quad (14)$$

and

$$(y_b)_{PAC2} = -4460 + 420\exp\left(\frac{-t}{14}\right) + 5500\exp\left(\frac{-t}{10607.75}\right) \quad (15)$$

The functions given by Eqs. (14) and (15) are graphically presented in Fig. 6 as dotted curves.

2) After defining the y_b functions, it is possible to express the $b(t)$ functions as given by Eq. (7).

3) Finally, the $b(t)$ functions should be introduced into the modified mathematical model (8). In this way, four correlations (16–19) were obtained:

$$\frac{\Delta D}{\Delta t} = c(1126.6 - 11.51t + 0.0583t^2) + (a_1 + a_2 t + a_3 t^2 + ...)D(t) \quad (16)$$

$$\frac{\Delta D}{\Delta t} = c\left(450 + 420\exp\left(\frac{-t}{10}\right) + 350\exp\left(\frac{-t}{275.94}\right)\right) + (a_1 + a_2 t + a_3 t^2 + ...)D(t) \quad (17)$$

$$\frac{\Delta D}{\Delta t} = c\left(370 + 1340\exp\left(\frac{-t}{4.7}\right) + 575\exp\left(\frac{-t}{140.2}\right)\right) + (a_1 + a_2 t + a_3 t^2 + ...)D(t) \quad (18)$$

$$\frac{\Delta D}{\Delta t} = c\left(-4460 + 420\exp\left(\frac{-t}{14}\right) + 5500\exp\left(\frac{-t}{10607.75}\right)\right) + (a_1 + a_2 t + a_3 t^2 + ...)D(t) \quad (19)$$

Their c and a (a_i, i = 1,n) parameters can be obtained by applying the regression analysis method over the experimental data. As the experimental data, the $D(t) \equiv (SO_4^{2-})_{bonded}$ values were taken. Their derivatives ($\Delta D/\Delta t$) might be determined by dividing the SO_4^{2-} concentration differences by the time increments, in accordance with the experiments. For example, for the first time increment (0–7 days), the numerically expressed derivative might be:

$$\frac{\Delta D}{\Delta t} = \frac{([SO_4^{2-}]_2 - [SO_4^{2-}]_1)_{bonded}}{7} = \frac{\Delta[SO_4^{2-}]_{bonded}}{7} \quad (20)$$

Off course, there are better methods for the determination of derivatives. Mostly, they are parts of software packages developed for a graphical presentation and mathematical processing of measured data (such as Origin and others).

Hence, the sulfate corrosion models are defined when $b(t)$ and $a(t)$ are determined. For the examined series of samples, the mentioned parameters are as follows.

1) For the PC1 samples:

$$b(t)_{PC1} = 0.01566(1126.6 - 11.51t + 0.0583t^2) \quad (21)$$

$$a(t)_{PC1} = -2.299\times10^{-2} - 1.320\times10^{-3}t + 4.373\times10^{-5}t^2 - 3.078\times10^{-7}t^3 \quad (22)$$

2) For the PAC1 samples:

$$b(t)_{PAC1} = 0.01977\left(450 + 420\cdot\exp\left(\frac{-t}{10}\right) + 350\cdot\exp\left(\frac{-t}{275.9}\right)\right) \quad (23)$$

$$a(t)_{PAC1} = -4.352\times10^{-2} + 7.486\times10^{-5}t + 7.6573\times10^{-9}t^2 \quad (24)$$

3) For the PC2 samples:

$$b(t)_{PC2} = 38.219\left(370 + 1340\exp\left(\frac{-t}{4.7}\right) + 575\exp\left(\frac{-t}{140.2}\right)\right) \quad (25)$$

$$a(t)_{PC2} = -7.363\times10^{-2} - 1.619\times10^{-4}t + 2.823\times10^{-6}t^2 - 7.010\times10^{-9}t^3 \quad (26)$$

4) For the PAC2 samples:

$$b(t)_{PAC2} = 0.0114\left(-4460 + 410\exp\left(\frac{-t}{14}\right) + 5500\exp\left(\frac{-t}{10607.75}\right)\right) \quad (27)$$

$$a(t)_{PAC2} = -2.918\times10^{-2} - 2.537\times10^{-4}t + 2.131\times10^{-6}t^2 - 4.212\times10^{-9}t^3 \quad (28)$$

The graphical presentations of the $b(t)$ functions and of the $a(t)D(t)$ products are given in Figs. 7 and 8, respectively. They will be used for further analysis of the influences of different factor on the sulfate corrosion of the examined samples.

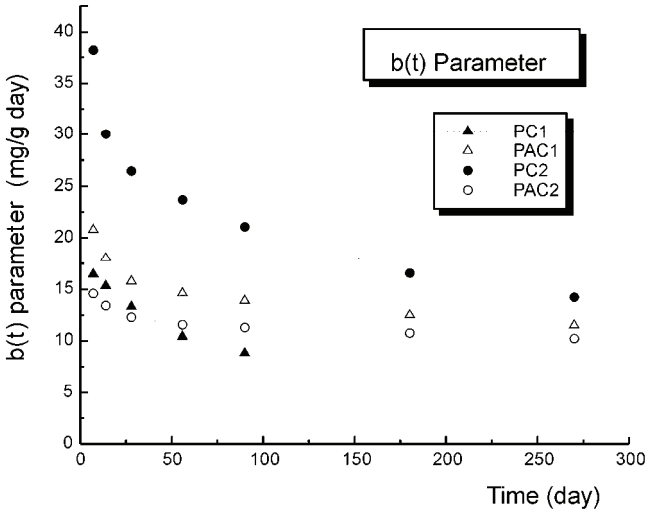

Fig. 7. Fit of the $b(t)$ parameter.

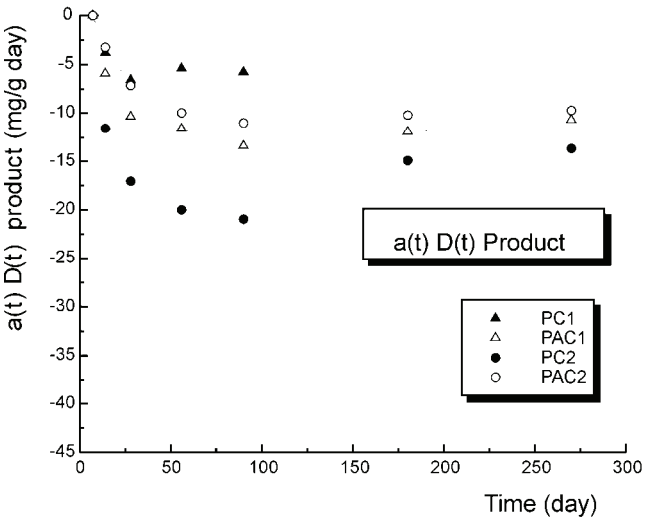

Fig. 8. Product between the fitted $a(t)$ parameter and the degree of degradation.

Comparison of the Matsufuji model and the presented modification

As expected, the modified mathematical model gave better results than the original; *i.e.*, the modified model described the sulfate corrosion of the examined samples more precisely than the Matsufuji Equation. This can be seen from Figs. 9–12, in which the experimental values of the concentration of bounded SO_4^{2-}, as well as the values estimated by both mathematical models are presented comparatively. As a quantifier of fitness quality, the standard deviation was accepted. The standard deviation values prove that the modified mathematical model is better than the Matsufuji Equation.

DISCUSSION

Experimentally obtained values

Non-ash samples. Both Portland cements reacted with SO_4^{2-} (see Fig. 3). This reaction was induced not only by the content of the C_3A compound but also by the content of C_3S and other compounds. The PC1 samples reacted slower than the PC2 samples. After certain period of time (*i.e.*, after 90 days), both non-ash samples reached the same quantity of bounded SO_4^{2-}, when the PC1 samples cracked and broke down.

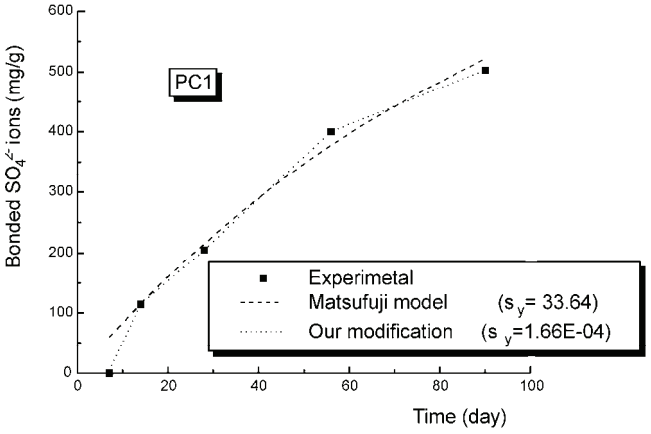

Fig. 9. Comparison of the experimental and estimated values for PC1.

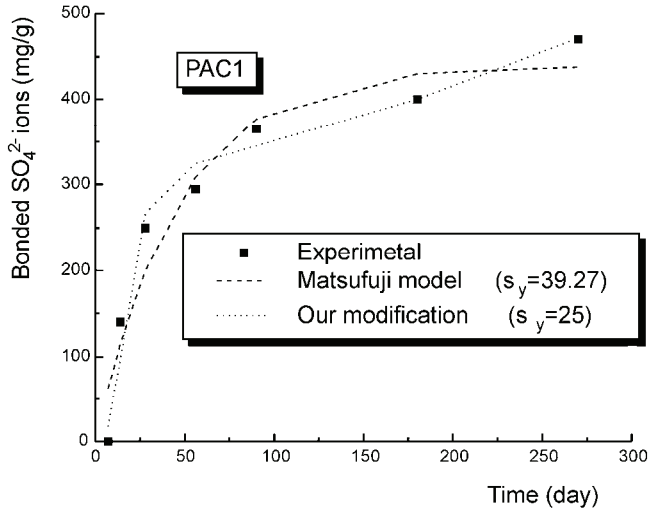

Fig. 10. Comparison of the experimental and estimated values for PAC1.

Sulfate corrosion caused a fast mass reduction (see Fig. 4), very probably due to appearance of sulfate bearing compounds (such as gypsum, ettringite, thaumasite).[1,2]

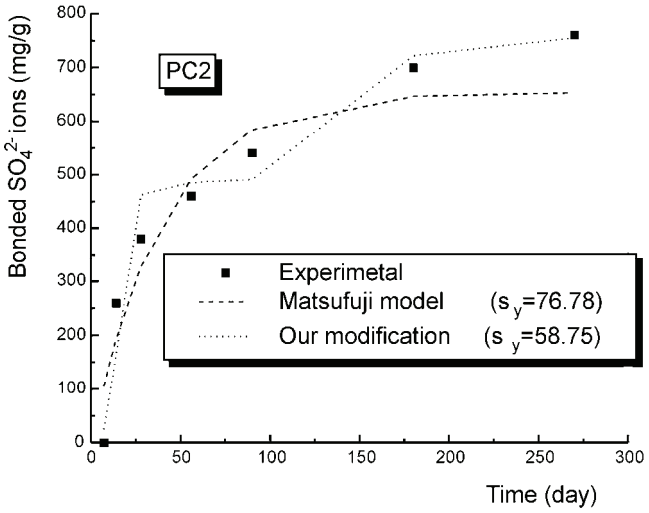

Fig. 11. Comparison of the experimental and estimated values for PC2.

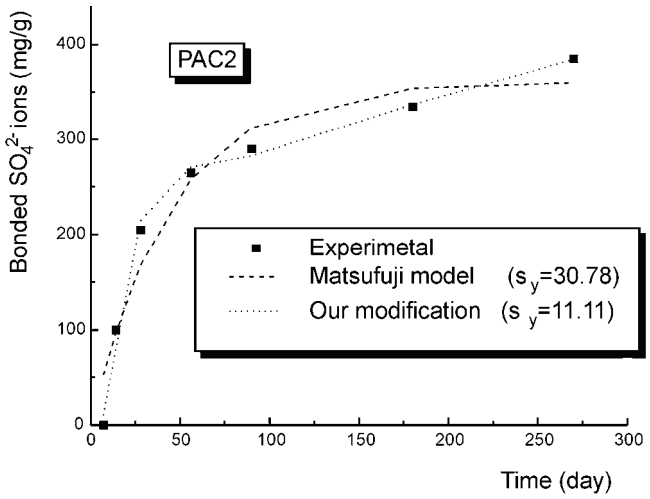

Fig. 12. Comparison of the experimental and estimated values for PAC2.

They disintegrated the system and decreased the mechanical characteristics extremely (see Fig. 5), which was remarkably evident in the case of the PC1 samples.

Ash samples. The presence of ash significantly improved resistance of both Portland cements to attack by sulfate (see Fig. 3). Although both (PAC1 and PAC2) samples incorporated a certain quantity of SO_4^{2-}, the amount was almost half the quantity incorporated into the non-ash samples. The phenomenon was particularly noticeable in the later stages.

Due to sulfate corrosion, the mass of both ash samples decreased slower than the mass of the non-ash samples. This mass reduction tended to be approximately 15 % (see Fig. 4). The flexural strength changed in accordance with the progress

of the physical destruction of the material. As it was slower in the presence of ash, these samples possessed greater strength; particularly the PAC2 samples (see Fig. 5).

Results obtained by the mathematical model

The model suggested in this paper allows a more detailed examination and a better explanation of the system changes during time. According to the experimentally determined values, the concentrations of SO_4^{2-} in the solutions decreased very rapidly in contact with the PC1 and PC2 samples. This change was much slower in the case of the ash samples, particularly PAC2 (see Fig. 6). The conclusion is in compliance with the fact that the non ash samples incorporated a greater quantity of SO_4^{2-} than the ash containing samples.

As far as the rate of deterioration is concerned, it is obvious that sulfate corrosion belongs to the convergence type of degradation. This process had a gradually decreasing rate, as presented in Fig. 13. An analysis of rate curves can give significant information about the progress of degradation with time. From the Fig. 13, it is obvious that the lowest rate of bonding of SO_4^{2-} is a characteristic of the ash samples (particularly PAC2), for all the investigated time periods. On the contrary, the highest rates characterized the non-ash samples, particularly PC2, at the beginning of corrosion. After one month, the situation changed and other non-ash sample (PC1) became more liable to bonding of SO_4^{2-}. Such a great rate caused the complete destruction and disintegration of the PC1 samples after three months. Finally, the analysis of the rate curves indicated that the presence of ash slowed down the absorption of the aggressive SO_4^{2-} by the investigated materials.

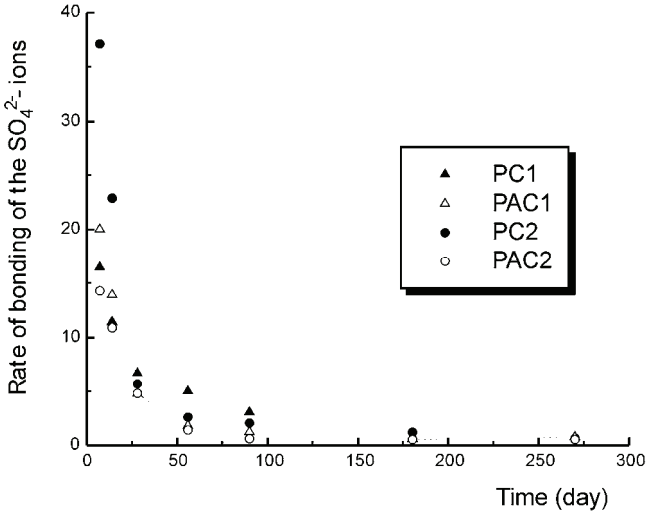

Fig. 13. Rate of bonding of SO_4^{2-} for all samples.

A more detailed study of the behavior of all the systems can be performed by applying of suggested mathematical model. According to Model (4), the degra-

dation rate is the sum of two terms; the first one, $b(t)$, expresses the influence of the immediate environment while the second one, $a(t)D(t)$, quantifies the behavior of the already deteriorated parts. The first one has a positive sign while the second one has a negative sign. It is desirable that the first one has a value as low as possible while the second one must have a value as high as possible. The physical meaning of both terms would be as follows: $b(t)$ represents the aggressiveness of the environment while the product $a(t)D(t)$ expresses the protective behavior of the sulfate bearing compounds already formed at the surface of the corroded object.

From Fig. 7 it is obvious that the aggression of the $(NH_4)_2SO_4$ solution is the most intensive in the case of the PC2 samples. Fortunately, the protective character of its deteriorating parts is very strong (see Fig. 8). Still, the rate of bonding of SO_4^{2-} was large for the PC2 samples. The aggression of the $(NH_4)_2SO_4$ solution in the case of all the other samples was rather similar and not too intensive (see Fig. 7). With the ash samples, it is neutralized by the protective behavior of the degradation products. As a result, these two phenomena (aggression and protection) induced a small rate of bonding of SO_4^{2-} in the case of the ash containing samples as a result. With regards to the behavior of the PC1 system, an extremely undesirable fact can be noticed, *i.e.*, the protective effect of the sulfate bearing layers was very weak. It decreased particularly after one month and caused the total destruction of PC1 samples after three months was very probable.

CONCLUSIONS

This paper introduces an improved model for the mathematical description of sulfate corrosion of particular systems prepared from Portland cement and Portland cement with 30 % of coal ash. The model enables a rather exact analysis of the behavior of all the systems. According to the model, the degradation rate is considered to be the sum of two terms; the first one represents the aggressiveness of the immediate environment while the second one expresses the protective behavior of sulfate bearing compounds already formed at the surface of corroded objects. It is concluded that the sulfate corrosion belongs to the attenuated type of deterioration. The model allowed not only better explanations of the degradation during the investigated time period, but also showed that the ash systems were significantly resistant to sulfate corrosion.

ИЗВОД

$(NH_4)_2SO_4$ КОРОЗИЈА ЦЕМЕНТА У БЕТОНУ АНАЛИЗИРАНА ПОБОЉШАНИМ МАТЕМАТИЧКИМ МОДЕЛОМ

САША МИЛЕТИЋ[1], МИРЈАНА ЂУРИЋ[2], АЊЕЛКА МИХАЈЛОВ[3], ЂОРЂЕ БАШИЋ[3] и ЂОРЂЕ ЈАНАЋКОВИЋ[4]

[1]Галеника Фитофармација, Батајнички друм бб, 11080 Земун, [2]Технолошки факултет, Универзитет у Новом Саду,Булевар Цара Лазара 1, 21000 Нови Сад, [3]Факултет техничких наука, Универзитет у Новом Саду, Трг Доситеја Обрадовића 6, Нови Сад и [4]Технолошко–металуршки факултет, Универзитет у Београду, Карнегијева 4, 11000 Београд

У раду је приказана критичка анализа једначине која предвиђа напредовање деградације разних грађевинских материјала, а коју су у скорије време предложили Matsufuji и други. После анализе, у раду је предложен побољшан математички модел, посебно оријентисан ка моделовању сулфатне корозије. Изведени су експерименти на два узорка Портланд цемента и на два узорка Портланд цемента са 30 % летећег пепела. Узорци су потопљени у 10 % раствор $(NH_4)_2SO_4$ и мерена је концентрација SO_4^{2-} у оба система – раствору и материјалу. Као параметар који квантификује деградацију цемента узет је садржај везаних SO_4^{2-}. Коришћењем добијених података дефинисан је математички модел за описивање сулфатне корозије четири испитивана узорка. Модели су примењени за анализу понашања узорака са летећем пепелом и без њега. Они омогућавају не само бољу интерпретацију деградације током испитиваног периода, већ и показују значајну отпорност система са летећим пепелом према сулфатној корозији.

(Примљено 18. јула, ревидирано 21. октобра 2008)

REFERENCES

1. Y. Matsufuji, T. Koyama, S. Harada, in *Proceedings of Durability of Building Materials and Components 7*, C. Sjostrom, Ed., E & FN Spon, London 1996, p. 45
2. U. Schneider, S.-W. Chen, in *Proceedings of Durability of Building Materials and Components 7*, C. Sjostrom, Ed., E & FN Spon, London, 1996, p. 383
3. M. A. Halliwell, N. J. Crammond, in *Proceedings of Durability of Building Materials and Components 7*, C. Sjostrom, Ed., E & FN Spon, London, 1996, p. 235
4. M. Djurić, J. Ranogajec, R. Omorjan, S. Miletić, *J. Serb. Chem. Soc*. **62** (1997) 1003
5. M. Djurić, J. Ranogajec, R. Omorjan, S. Miletić, *Cement Concrete Res.* **26** (1996) 1295
6. M. Djurić, I. Grzetić, *Ceram. Silikaty* **41** (1997) 152
7. A. Koch, H. Steinneger, *ZKG-International* **13** (1960) 317
8. S. Miletić, M. Ilić, J. Ranogajec, R. Marinković-Neducin, M. Djurić, *Cement Concrete Res*. **28** (1998) 713.

Journal of the Serbian Chemical Society
JSCS@tmf.bg.ac.rs • www.shd.org.rs/JSCS

J. Serb. Chem. Soc. 74 (3) 349–357 (2009)
JSCS–3836

UDC 546.57–72:677.674/.675:
:677.027:615.281.004.12
Original scientific paper

A study of the antibacterial efficiency and coloration of dyed polyamide and polyester fabrics modified with colloidal Ag nanoparticles

VESNA ILIĆ[1], ZORAN ŠAPONJIĆ[2], VESNA VODNIK[2], DARKA MIHAILOVIĆ[1], PETAR JOVANČIĆ[1], JOVAN NEDELJKOVIĆ[2#] and MAJA RADETIĆ[1]*

[1]*Textile Engineering Department, Faculty of Technology and Metallurgy, Karnegijeva 4, 11000 Belgrade and* [2]*Vinča Institute of Nuclear Sciences, P.O. Box 522, 11001 Belgrade, Serbia*

(Received 3 September, revised 11 November 2008)

Abstract: In this study, the influence of dyeing on the antibacterial efficiency of polyamide and polyester fabrics loaded with colloidal Ag nanoparticles and the influence of the presence of Ag nanoparticles on the color change of dyed fabrics were investigated. Dyes C.I. acid green 25 and C.I. disperse blue 3 were used for dyeing of polyamide fabrics, while dye C.I. disperse violet 8 was used for dyeing of polyester fabrics. The influence of Ag nanoparticles on the color change of polyamide fabrics depends on the dye type, but generally it was lower compared to polyester fabrics. Polyester fabrics exhibited excellent antibacterial efficiency against Gram-positive bacterium *Staphylococcus aureus* and Gram-negative bacterium *Escherichia coli*, independent of the order of dyeing and Ag loading. Polyamide fabrics provided a desirable level of antibacterial activity only if the Ag loading was performed after dyeing.

Keywords: Ag nanoparticles; polyester; polyamide; antibacterial efficiency; color change.

INTRODUCTION

The traditional approach to textile materials from only an aesthetic and comfort point of view must be considered as the past. Currently, in addition to conventional end-use properties, textile products must exhibit some advanced properties, such as UV protection, self-cleaning, antimicrobial and/or anti-electrostatic properties.[1–3] These effects can be achieved using new technologies that can provide targeted functionalization and long-term durability, as well as environmental and economical feasibility. Developments in the synthesis of dif-

* Corresponding author. E-mail: maja@tmf.bg.ac.rs
# Serbian Chemical Society member.
doi: 10.2298/JSC0903349I

ferent metal and metal oxide nanoparticles (NPs) and the wide range of their successful applications opened up new perspectives for the engineering of desired properties of textile materials. The greatest interests are oriented towards the imparting of antimicrobial effects.[4–15] Ag NPs seem to be particularly convenient for the improvement of antimicrobial properties of textile materials since bacteria do not become resistant to Ag as in the case of antibiotics.[4] The high stability and large surface to bulk ratio of Ag NPs provide an excellent antibacterial efficiency.

Although much work has been done on the antimicrobial activity of Ag NPs on different textile materials,[4–15] there are only few data on the synergism between loading of Ag NPs and dyeing or printing.[6,16] This aspect is of great importance from the technological point of view since textile products should preserve all the usual aesthetic and comfort standards. Therefore, the influence of dyeing on the antibacterial efficiency of polyamide (PA) and polyester (PES) fabrics loaded with Ag NPs, as well as the influence of Ag NPs on the color change of dyed fabrics were the focus of this study. Dyes C.I. acid green 25 and C.I. disperse blue 3 were used for dyeing of PA fabrics, while dye C.I. disperse violet 8 was used for dyeing of PES fabrics. The antibacterial efficiency was tested against Gram-positive bacterium *Staphylococcus aureus* and Gram-negative bacterium *Escherichia coli*.

EXPERIMENTAL

Desized and bleached PA (150 g/m^2) and PES (165 g/m^2) fabrics were cleaned in a bath containing 0.50 % nonionic washing agent Felosan RG-N (Bezema) at a liquor-to-fabric ratio of 50:1.[17] After 15 min of washing at 50 °C, the fabrics were rinsed once with warm water (50 °C) for 3 min and three times (3 min) with cold water. The samples were dried at room temperature.

The PA fabrics were dyed with acid dye C.I. acid green 25 (Ortolgreen B, BASF) and disperse dye C.I. disperse blue 3 (Colliton Blue FFR, BASF), whereas the disperse dye C.I. disperse violet 8 (Palanil Violet 3B, BASF) was used for dyeing of PES fabrics.

$AgNO_3$ (Kemika) and $NaBH_4$ (Fluka) of *p.a.* grade were used without any further purification for the synthesis of the colloidal Ag NPs.[18,19] Briefly, 8.5 mg of $AgNO_3$ was dissolved in 250 mL of water and purged with argon for 30 min. Under vigorous stirring, the reducing agent $NaBH_4$ (125 mg) was added to the solution and left for 1 h under an argon atmosphere. The concentration of the Ag colloid was 50 ppm.

One gram of fabric was immersed in 65 mL of Ag colloid for 5 min and dried at room temperature. After 5 min of curing at 100 °C, the procedure was repeated. Subsequently, the samples were rinsed twice (5 min) with deionized water and dried at room temperature.

A schematic presentation of the dyeing procedures for PA and PES fabrics is presented in Fig. 1. The PA fabrics were dyed in a bath containing 2.0 % (o.w.f.) acid dye and 4.0 % (o.w.f.) Na_2SO_4 at a liquor-to-fabric ratio of 60:1 and at pH 4.0. The dyeing of the PA fabrics with disperse dye was performed in a bath containing 2.0 % (o.w.f.) dye at a liquor-to-fabric ratio of 60:1 and at pH 5.0. The pH values were adjusted with CH_3COOH (30 %). The PES fabrics were dyed in a bath containing 1.0 % (o.w.f.) disperse dye, 1 g/L CHT dispergator (Bezema) and 0.50 mL/L CH_3COOH (30 %) at a liquor-to-fabric ratio of 25:1 and at pH 5.0. The fabrics were then washed in a bath containing 0.50 % Felosan RG-N (Bezema) at a liquor-to-

-fabric ratio of 40:1. After 30 min of washing at 40 °C, the fabrics were rinsed once with warm water (40 °C) for 3 min and four times (3 min) with cold water. Afterwards, the fabrics were dried at room temperature.

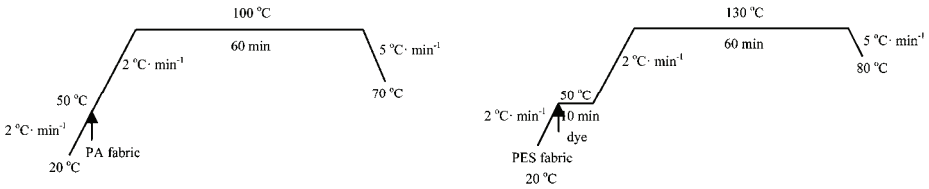

(a) (b)

Fig. 1. Dyeing procedures for PA (a) and PES (b) fabrics.

The shape and size of silver NPs were determined using a Philips EM-440 transmission electron microscope (TEM) operating at 100 kV. Samples for the TEM measurements were prepared by placing a drop of Ag colloid onto a holey carbon-coated standard copper grid (400 mesh) and evaporating the solvent.

The UV/Vis absorption spectra of the silver colloid were recorded using a Thermo Evolution 600 spectrophotometer.

The fiber morphology was observed using a JEOL JSM 6460 LV scanning electron microscope (SEM). Prior to analysis, the samples were coated with a thin layer of gold.

The elemental analysis of the PES and PA fabrics loaded with silver NPs was realized using a Perkin Elmer 403 atomic absorption spectrometer (AAS).

The color coordinates of the dyed fabrics (CIE L^*, a^*, b^*) were determined with Datacolor SF300 spectrophotometer under illuminant D_{65} using the 10° standard observer. On the basis of the measured CIE color coordinates, the color difference (ΔE^*) was determined as:

$$\Delta E^* = \sqrt{(\Delta a^*)^2 + (\Delta b^*)^2 + (\Delta L^*)^2} \tag{1}$$

where: ΔL^* is the color lightness difference between the treated (dyed fabric loaded with Ag NPs) and the control (dyed untreated fabric without Ag) samples; Δa^* is the red/green difference between the treated and control samples and Δb^* is the yellow/blue difference between the treated and control samples.

The influence of dyeing on the antibacterial efficiency of fabrics was quantitatively assessed using a Gram-positive bacterium *Staphylococcus aureus* ATCC 25923 and a Gram--negative bacterium *Escherichia coli* ATCC 25922. Sterile potassium hydrogen phosphate buffer solution of pH 7.2 (70 mL) was inoculated with 0.7 mL of a bacterial inoculum. One gram of sterile fabric cut into small pieces was put into the flask and shaken for 1 h. 1.0 mL aliquots from the flask were diluted with phosphate buffer and 0.10 mL of the solution was placed onto a tryptone soy agar (Torlak, Serbia). After 24 h of incubation at 37 °C, zero time and one hour counts of viable bacteria were made. The percentage bacteria reduction (R / %) was calculated using Eq. (2):

$$R = 100\frac{C_0 - C}{C_0} \tag{2}$$

where: C_0 (CFU – colony forming units) is the number of bacteria colonies on the control fabric (fabric without Ag, dyed in the described manner), and C (CFU) is the number of bacteria colonies on the dyed fabric loaded with Ag NPs.

RESULTS AND DISCUSSION

The absorption spectrum of the colloidal Ag NPs showed the presence of a strong surface plasmon resonance band with a maximum at 380 nm (Fig. 2). The position of the symmetric plasmon resonance band and its half-width (46 nm) indicated a narrow size distribution of Ag NPs without undesired aggregation. Based on the TEM analysis of the colloidal Ag NPs, the average diameter of the nearly spherical Ag NPs was found to be 10 nm (inset in Fig. 2).

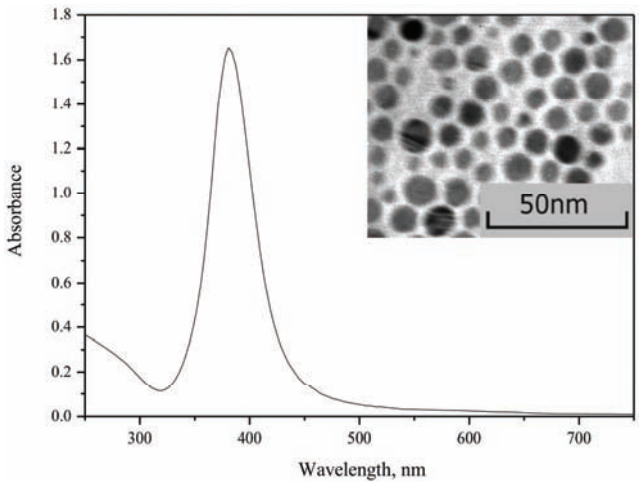

Fig. 2. Absorption spectrum of Ag NPs in aqueous solution; inset: TEM image of the Ag NPs.

The surface morphology of the PA and PES fibers loaded with Ag NPs was examined by SEM. The SEM images of the Ag loaded PA and PES fibers are shown in Fig. 3. It can be noticed that almost spherical aggregates of Ag NPs with diameters less than 100 nm are unevenly distributed over the surface of both fibers.

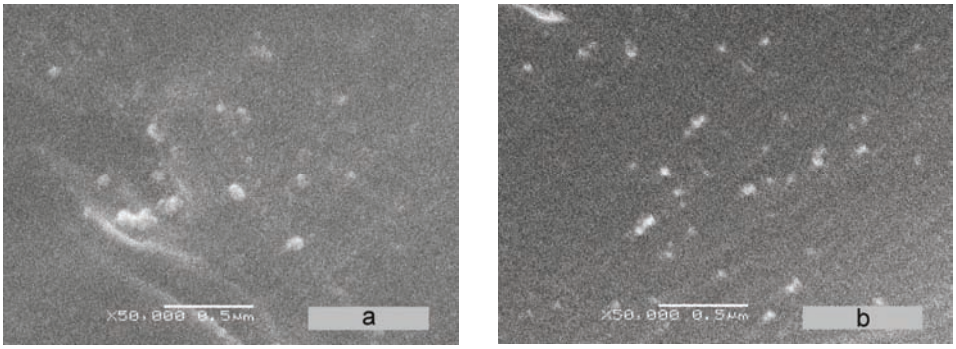

Fig. 3. SEM images of Ag-loaded PA (a) and PES (b) fibers.

To quantify the Ag on the fabrics after loading the colloidal NPs, elemental analysis using atomic absorption spectrometry was performed. It was found that

one gram of PA and PES fabrics contained 1.79 and 21.12 μg of Ag, respectively. Evidently, the amount of Ag on PES fabrics was more than ten times higher. The higher content of Ag NPs on the PES fibers indicates their stronger binding, most likely due to the existence of benzene rings in polymer structure. It is well known from surface-enhanced Raman spectroscopy (SERS) studies of benzoic acid and its derivates on Ag NPs that there are strong interactions between the Ag surface and benzene rings.[20,21]

These results are in good correlation with the color changes of the fabrics, which were evaluated by measuring the UV/Vis reflectance spectra (Fig. 4). Loading of Ag NPs caused color changes of the PA and PES fabrics. Due to loading of Ag NPs, an overall decrease in the reflectance was observed for both samples, demonstrating a color change of the PA and PES fabrics from white to yellowish. The observed color changes are in accordance with literature data.[8] The more pronounced color change of the PES fabric could be anticipated because of the higher amount of Ag NPs detected by AAS. The color difference between fabrics loaded with Ag NPs and control fabrics (untreated fabrics) was expressed *via* the ΔE^*, ΔL^*, Δa^* and Δb^* values (also presented in Fig. 4).

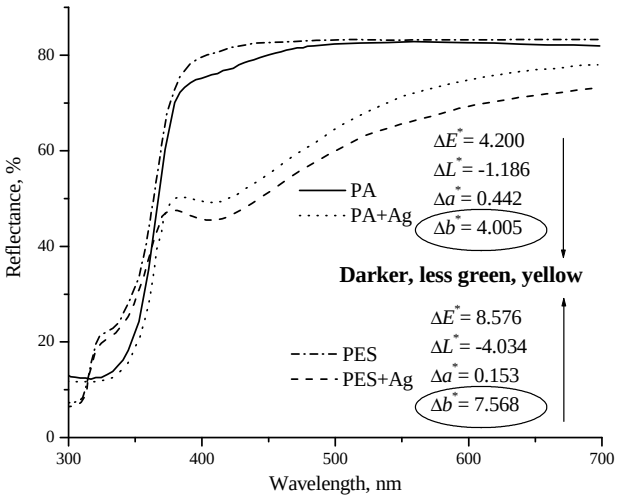

Fig. 4. Reflectance curves of the control (untreated fabrics) and silver-loaded PA and PES fabrics.

Bearing in mind that the fiber surface is responsible for many important properties of textile materials (wettability, dyeability, printability, *etc.*), it can be expected that modification of PA and PES fibers with Ag NPs might affect their dyeability. In order to establish the influence of the Ag NPs presence on the color of dyed PA and PES fabrics, colorimetric determination based on the CIELAB color system was performed. The colorimetric data for the fabrics loaded with Ag NPs before and after dyeing are given in Table I.

The obtained results indicate that the color of PA fabrics dyed with AG25 was almost unaffected by Ag loading, regardless of the order of Ag loading and dyeing. The obtained color changes could not be visually detected since the values of the color difference (ΔE^*) were less than one. However, the influence of the Ag NPs was more pronounced after dyeing of PA fabrics with DB3. The loading of Ag NPs onto the PA fabrics before and particularly after dyeing brought about considerable color changes. The fabrics became darker (ΔL^*), less red (Δa^*) and less blue (Δb^*). A similar trend was observed in the case of PES fabrics dyed with DV8, although the color difference (ΔE^*) was several times greater, demonstrating a significant color change. The increased greenness and decreased blueness are attributed to the presence of the Ag NPs on the fabrics.

TABLE I. Colorimetric data for PA and PES fabrics loaded with Ag NPs before and after dyeing

Dye	Sample	L^*	a^*	b^*	ΔE^*	Description
AG25	Control PA[a]	30.16	–25.40	–4.72		
			Silver loading before dyeing			
	PA+Ag	29.92	–25.46	–4.75	0.251	Darker
			Silver loading after dyeing			
	PA+Ag	29.80	–24.82	–4.23	0.833	Darker, less green, less blue
DB3	Control PA[a]	34.80	6.15	–44.78		
			Silver loading before dyeing			
	PA+Ag	33.23	6.83	–43.87	1.934	Darker, less red, less blue
			Silver loading after dyeing			
	PA+Ag	34.47	4.28	–41.69	3.629	Darker, less red, less blue
DV8	Control PES[a]	43.38	14.55	–39.52		
			Silver loading before dyeing			
	PES+Ag	43.37	11.94	–35.31	4.962	Less red, less blue
			Silver loading after dyeing			
	PES+Ag	42.19	9.75	–30.95	9.901	Darker, less red, less blue

[a]Dyed fabric without Ag NPs

Despite the low content of Ag on the PES and, particularly, the PA fabrics, these amounts were sufficient to impart a desirable level of antibacterial activity. The influence of the order of dyeing and loading of Ag NPs on the antibacterial activity of the PA and PES fabrics was evaluated for the Gram-positive bacterium *Staphylococcus aureus* and the Gram-negative bacterium *Escherichia coli*. The values of bacterial reduction by the PA and PES fabrics which had been Ag--loaded before and after dyeing are given in Tables II and III.

The PES fabrics showed outstanding antibacterial efficiency for both bacteria regardless of the order of the operations. Similarly, the PA fabrics exhibited excellent antibacterial efficiency when the loading of the Ag NPs was performed after dyeing, regardless of the dye studied. However, the opposite order of operations led to a significant decrease in bacterial reduction of *E. coli* on the PA fab-

rics. These PA fabrics can be considered as inactive. Evidently, to obtain the maximum antibacterial efficiency, the order of the operations must be carefully planned. Hence, it is recommended that the loading of Ag NPs onto PA fabrics should be performed after dyeing, while Ag loading of PES fabrics after dyeing should be avoided due to the strong color change of the fabrics.

TABLE II. Antibacterial efficiency of PA and PES fabrics loaded with Ag NPs before dyeing

Dye	Sample	Initial number of bacterial colonies ($\times10^{-5}$)	Number of bacterial colonies on the fabric after 24 h	R / %
		S. aureus		
AG25	Control PA[a]	2.4	2.4×10^{5}	
	PA+Ag		5.2×10^{3}	97.8
DB3	Control PA[a]	2.4	1.3×10^{5}	
	PA+Ag		<10	99.9
DV8	Control PES[a]	3.0	2.5×10^{4}	
	PES+Ag		<10	99.9
		E. coli		
AG25	Control PA[a]	5.2	2.7×10^{5}	
	PA+Ag		1.8×10^{5}	33.3
DB3	Control PA[a]	5.2	1.7×10^{5}	
	PA+Ag		1.2×10^{5}	29.4
DV8	Control PES[a]	3.0	8.5×10^{4}	
	PES+Ag		<10	99.9

[a]Dyed fabric without Ag NPs

TABLE III. Antibacterial efficiency of PA and PES fabrics loaded with Ag NPs after dyeing

Dye	Sample	Initial number of bacterial colonies ($\times10^{-5}$)	Number of bacterial colonies on the fabric after 24 h	R / %
		S. aureus		
AG25	Control PA[a]	2.4	2.4×10^{5}	
	PA+Ag		<10	99.9
DB3	Control PA[a]	2.4	1.3×10^{5}	
	PA+Ag		<10	99.9
DV8	Control PES[a]	3.0	2.5×10^{4}	
	PES+Ag		<10	99.9
		E. coli		
AG25	Control PA[a]	3.9	2.2×10^{5}	
	PA+Ag		<10	99.9
DB3	Control PA[a]	3.9	1.3×10^{5}	
	PA+Ag		130	99.9
DV8	Control PES[a]	3.0	8.5×10^{4}	
	PES+Ag		<10	99.9

[a]Dyed fabric without Ag NPs

CONCLUSIONS

The order of loading of Ag NPs and dyeing has a strong influence on the color change of PA and PES fabrics. It was shown that the color of the PA fabrics dyed with C.I. acid green 25 was slightly affected by Ag loading, regardless of the order of the operations. On the contrary, the loading of Ag NPs onto fabrics before and particularly after dyeing with C.I. disperse blue 3 induced considerable color changes. Moreover, the color changes became even more prominent on the PES fabrics which were Ag loaded after dyeing with C.I. disperse violet 8. The obtained color changes are suggested to be due to the presence of Ag NPs on the fabrics.

The antibacterial efficiency of the PES fabrics for *S. aureus* and *E. coli* is independent of the order of dyeing and loading of Ag NPs. In order to achieve desired level of antibacterial efficiency of PA fabrics, the loading of the Ag NPs after dyeing is recommended.

Acknowledgement. The financial support for this work was provided by the Ministry of Science and Environment of Republic of Serbia (Eureka project NANOVISION E! 4043 and project 142066). We gratefully acknowledge M. Bokorov (University of Novi Sad, Serbia) for providing the SEM measurements.

И З В О Д

ПРОУЧАВАЊЕ АНТИБАКТЕРИЈСКЕ ЕФИКАСНОСТИ И ПРОМЕНЕ ОБОЈЕЊА ПОЛИАМИДНИХ И ПОЛИЕСТАРСКИХ ТКАНИНА МОДИФИКОВАНИХ КОЛОИДНИМ НАНОЧЕСТИЦАМА СРЕБРА

ВЕСНА ИЛИЋ[1], ЗОРАН ШАПОЊИЋ[2], ВЕСНА ВОДНИК[2], ДАРКА МИХАИЛОВИЋ[1], ПЕТАР ЈОВАНЧИЋ[1], ЈОВАН НЕДЕЉКОВИЋ[2] и МАЈА РАДЕТИЋ[1]

[1]*Катедра за текстилно инжењерство, Технолошко–металуршки факултет, Карнегијева 4, 11120 Београд и* [2]*Институт за нуклеарне науке "Винча", п.пр. 522, 11001 Београд*

Циљ овог рада је да се утврди утицај бојења на антибактеријску ефикасност полиамидних и полиестарских тканина модификованих колоидним наночестицама сребра као и утицај присуства сребра на промену обојења бојених тканина. Боје C.I. acid green 25 и C.I. disperse blue 3 су коришћене за бојење полиамидних тканина, а боја C.I. disperse violet 8 за полиестарске тканине. Промена обојења полиамидних тканина зависи од типа боје, али је генерално мања у поређењу са полиестарским тканинама. Антибактеријска ефикасност тканина модификованих сребром је тестирана на Грам-позитивне бактерије *Staphylococcus aureus* и Грам-негативне бактерије *Escherichia coli*. Полиестарске тканине показују одличну антибактеријску ефикасност независно од редоследа бојења и наношења сребра. Да би полиамидна тканина обезбедила жељени ниво антибактеријске активности, неопходно је нанети сребро после бојења. Морфологија влакана модификованих нанчестицама сребра утврђена је СЕМ анализом, док је за елементарну анализу коришћена атомска апсорпциона спектрометрија.

(Примљено3. септембра, ревидирано 11. новембра 2008)

REFERENCES

1. T. Wakida, S. Tokino, *Indian J. Fibre Text. Res.* **21** (1996) 69

2. M. Ueda, S. Tokino, *Rev. Prog. Coloration* **26** (1996) 9
3. Y. W. H. Wong, C. W. M. Yuen, M. Y. S. Leung, S. K. A. Ku, L. I. Lam, *AUTEX Res. J.* **6** (2006) 1
4. D. Pohle, C. Damm, J. Neuhof, A. Rösch, H. Münsted, *Polym. Polym. Compos.* **15** (2007) 357
5. N. Vigneshwaran, A. A. Kathe, P. V. Varadarajan, R. P. Nachane, R. H. Balasubramanya, *J. Nanosci. Nanotechnol.* **7** (2007) 1893
6. H. J. Lee, S. Y. Yeo, S. H. Jeong, *J. Mater. Sci.* **38** (2003) 2199
7. S. Y. Yeo, H. J. Lee, S. H. Jeong, *J. Mater. Sci.* **38** (2003) 2143
8. T. Yuranova, A. G. Rincon, A. Bozzi, S. Parra, C. Pulgarin, P. Albers, J. Kiwi, *J. Photochem. Photobiol. A* **161** (2003) 27
9. U. C. Hipler, P. Elsner, J. W. Fluhr, *J. Biomed. Mater. Res. B* **77B** (2005) 156
10. S. H. Jeong, Y. H. Hwang, S. C. Yi, *J. Mater. Sci.* **40** (2005) 5413
11. H. J. Lee, S. H. Jeong, *Text. Res. J.* **75** (2005) 551
12. S. H. Jeong, S. Y. Yeo, S. C. Yi, *J. Mater. Sci.* **40** (2005) 5407
13. L. Hadad, N. Perkas, Y. Gofer, J. Calderon-Moreno, A. Ghule, A. Gedanken, *J. Appl. Polym. Sci.* **104** (2007) 1732
14. H. Y. Ki, J. H. Kim, S. C. Kwon, S. H. Jeong, *J. Mater. Sci.* **42** (2007) 8020
15. N. Duran, P. D. Marcato, G. I. H. De Souza, O. L. Alves, E. Esposito, *J. Biomed. Nanotechnol.* **3** (2007) 203
16. M. Gorensek, P. Recelj, *Text. Res. J.* **77** (2007) 138
17. M. Radetić, V. Ilić, V. Vodnik, S. Dimitrijević, P. Jovančić, Z. Šaponjić, J. Nedeljković, *Polym. Adv. Technol.* **19** (2008) 1816
18. V. V. Vuković, J. M. Nedeljković, *Langmuir* **9** (1993) 980
19. Z. V. Šaponjić, R. Csencsits, T. Rajh, N. Dimitrijević, *Chem. Mater.* **15** (2003) 4521
20. D. Wu, Y. Fang, *J. Colloid Interface Sci.* **265** (2003) 234
21. Y. Badr, M. A. Mahmoud, *J. Mol. Struct.* **749** (2005) 187.